CHAPTER 11
Numerical Methods in Antenna Modeling

J.-F. Lee, R. Lee, V. Rawat, K. Sertel, and F. L. Teixeira

In this chapter, we present three main numerical methods that are capable of solving complex electromagnetic wave radiation and scattering problems in three-dimensional (3D). They are: time-domain methods including finite-difference and finite-element time-domain methods, finite-element frequency-domain methods, and a conformal domain decomposition method using interior penalty formulation. This chapter starts by discussing the state-of-art time-domain methods, followed by a detailed description of the frequency-domain finite-element methods (FEM). Finally, we include a conformal domain decomposition method which does not require additional auxiliary variables. Throughout the chapter, various complex and electrically large numerical examples are also included.

11.1 Time-Domain Modeling

In this section, we shall discuss some time-domain computational electromagnetics (CEM) methods for antenna analysis.[1] Due to space limitations, we will focus on the finite-difference time-domain (FDTD) and finite-element time-domain (FETD) methods [8], [10], [1]. These are two of the most popular methods presently available and widely used in many commercially available software packages.

11.1.1 FDTD and FETD: Basic Considerations

Time-domain simulations of antenna problems are sometimes an attractive alternative to frequency-domain simulations because they can produce wideband data with a single code execution. As a result, they are particularly suited, for example, to ultra-wideband antenna problems, as will be illustrated later on in this section. Antenna scenarios involving nonlinear and/or time-varying media/components are more easily tackled in the time-domain as well.

In general, a time-domain discretization strategy for Maxwell's equations may involve either *explicit* or *implicit* "marching-on-time" updates (also called

[1] Portions of this material have previously appeared in [1]–[7].

"time-stepping"). Explict updates refer to time-domain discretizations whereby the fields to be determined at a given time step depend only on (known) field values at previous time steps. On the other hand, implicit updates refers to time-domain discretizations whereby present field values depend not only on previous field values but also on each other. As a result, implicit updates require the solution of a linear system (typically sparse) at every time step, whereas explicit update may not (the latter are denoted "matrix-free"). This is a clear advantage for explicit updates. The most celebrated explicit time-domain method is the conventional Yee's FDTD scheme [8]. However, explicit updates are subject to the so-called Courant limit, which sets a bound on the maximum size of the time increment from numerical stability considerations [11]. In contrast, some implicit updates are not subject to the Courant limit and the time increment size in this case can be chosen from accuracy considerations only, which can lead to a time increment much larger than the one set by the Courant limit.

In its basic form as introduced by Yee and pioneered by Taflove, the FDTD method is conceptually very simple and relies on the approximation of time and space derivatives of Maxwell curl equations by central differences on staggered grids, leading to a scheme which is second-order accurate in both space and time [8]. The grid in FDTD is typically a structured rectangular grid. Because FDTD is matrix-free, its memory requirements scale only linearly with the number of unknowns. This, added to the fact that FDTD is massively parallelizable, makes FDTD quite suited for petascale computing and beyond. Higher-order versions of FDTD also exist, which trade simulation accuracy by sparsity.

Being naturally constructed for unstructured irregular grids, FETD is quite suited for numerical solution of antenna problems in complex geometries where the use of a rectangular FDTD grid would give rise to staircasing error. FETD is also suited for implementations with *p*- and *h*-refinement capabilities. However, FETD methods in irregular grids lead to implicit schemes requiring the solution of a sparse linear system at every time step. For Maxwell's equations, it is possible to obtain explicit ("matrix-free") FEM using, for instance, mass (matrix) lumping, but not without shortcomings (in particular, they are prone to numerical instabilities). There are two basic approaches for constructing FETD algorithms for Maxwell equations. The first approach is based on the discretization of the second-order vector Helmholtz wave equation (for either the electric or magnetic field) by expanding the unknown field in terms of local basis functions—most commonly (curl-conforming) Whitney edge elements—followed by application of the method of weighted residuals via an inner product with test functions [10]. In order to produce symmetric matrices (assuming reciprocal media), the set of test functions is chosen identical to the set of basis functions (Galerkin testing). The second FETD approach is based on the discretization of the first-order Maxwell curl equations by expanding the electric and magnetic fields in terms of "mixed" elements, most commonly Whitney edge elements for the electric field and (div-conforming) Whitney face elements for the magnetic flux density [12]. This choice avoids the appearance of spurious modes (by satisfying a discrete version of the de Rham diagram). This is followed by either (a) application of the method of weighted residuals with appropriate (also mixed) test functions or (b) by the use of incidence matrices and construction of discrete Hodge operators [12].

11.1.2 UWB Antenna Problems in Complex Media

Some of the antenna problems where FDTD and FETD are mostly suited for involve UWB operation, as noted above, and/or scenarios where the antenna is loaded by or in close proximity of inhomogeneous and possibly dispersive media. This, of course, necessitates algorithms able to incorporate frequency dispersive effects in the time-domain. In linear, time-invariant, isotropic media, the time-domain constitutive equation relating the electric field and the electric flux density $\bar{D}$ is typically cast as a convolution between $\bar{E}$ and the permittivity as follows

$$\bar{D}(\bar{r}, t) = \int_{-\infty}^{t} \epsilon(\bar{r}, t-\tau)\bar{E}(\bar{r}, \tau)d\tau \tag{11-1}$$

$$\epsilon(\bar{r}, t) = \epsilon_0\delta(t) + \epsilon_0\chi_e(\bar{r}, t) \tag{11-2}$$

where $\epsilon(\bar{r}, t) = \mathcal{F}^{-1}[\epsilon(\bar{r}, \omega)]$ is the time-domain permittivity function, $\mathcal{F}$ stands for Fourier transformation, ϵ_0 is the vacuum permittivity, $\delta(t)$ is the Dirac delta function, and $\chi_e(\bar{r}, t)$ is the (time-domain) electric susceptibility function. In FDTD or FETD, the time variable is discretized as $t_l = l\Delta t$ with $l = 0, 1, 2 \ldots$. We denote $\bar{E}(l\Delta t) = \bar{E}^l$, and similarly for the other fields. A direct implementation of the convolution above would require storage of the entire past time series of $\bar{E}^l$, which is obviously impractical. However, due to the exponential nature of the susceptibility kernel, a *recursive* convolution can be implemented instead where storage of only a few previous time-step values is needed (the actual number depends on the order of accuracy sought—two or three steps are typical in FDTD). The terminology RC is usually reserved for the low-order implementation that assumes a piecewise constant electric field between each time step. Other implementations for the convolution also exist, with the *piecewise linear recursive convolution* (PLRC) [2] being a popular choice and illustrated below. Since conventional FDTD is second-order accurate in time, it is usually not advantageous to implement a high order accurate recursive convolution unless the time integration in the core FDTD update (of Maxwell curl equations) itself is of high order.

In linear time-invariant media, the constitutive equation in dispersive media can also be cast as ordinary differential equation (ODE) in time involving $\bar{D}$ and $\bar{E}$ or, alternatively, involving $\bar{E}$ and some induced macroscopic polarization field. In linear time-invariant media, this ODE is linear with constant coefficients (in time) with the generic form

$$\sum_{p=0}^{N_1} a_p(\bar{r})\frac{\partial^p \bar{D}(\bar{r}, t)}{\partial t^p} = \sum_{p=0}^{N_2} b_p(\bar{r})\frac{\partial^p \bar{E}(\bar{r}, t)}{\partial t^p} \tag{11-3}$$

or an analogous ODE involving $\bar{E}$ and polarization fields. In some cases, additional dynamic fields are present in the physical model so that an ODE *system* ensues.

The order N_1, N_2 and the coefficients $a_p(\bar{r})$, $b_p(\bar{r})$ above depend on the particular dispersion model considered for $\epsilon(\bar{r}, \omega)$. In FDTD, the above ODE can be discretized by, for example, recasting it as an equivalent *system* of ODEs involving only first- and/or second-order differential equations, followed by a FD approximation in time of each differential equation [2]. This is commonly referred to as the *auxiliary differential equation* (ADE) approach.

The presence of inhomogeneous media of course poses no difficulties for FDTD or FETD as they are volumetric discretization schemes where medium properties are naturally described point-wise. Both methods are also able to model anisotropic media without much difficulty [1], [13], [14]. A recent survey of FDTD and FETD as applied to problems involving media having more complex properties (nonlinear, anisotropic, etc.) can be found in [1]

11.1.3 PML Absorbing Boundary Condition

For problems in unbounded regions, which comprise the vast majority of antenna problems, an absorbing boundary condition (ABC) needs to be imposed at the outer edges of the computational domain to suppress spurious reflection from the grid truncation. The most versatile ABC for complex media is the perfectly matched layer (PML) [15], [16], which can be implemented in either FDTD [8], [2] or FETD [3]. Apart from its numerical efficiency, a major advantage of PML over other ABCs is that its reflectionless absorption properties hold independently of the frequency of the incident wave (in the continuum limit). Most other ABCs are not suited for dispersive media because they require knowledge of the wave velocity near the grid boundary, a quantity that is not well-defined for dispersive media in the time-domain. Another advantage of PML is that it preserves the nearest-neighbor-interaction property of FDTD and FETD, hence retaining their suitability for parallelization. The original PML concept applies only to Cartesian coordinates (planar grid terminations). To extend its range of applicability, the PML concept was implemented in nonorthogonal FDTD grids and curvilinear FEM meshes with good results [17], [18]. However, these implementations were based on an *approximate* matching because they assumed the metric coefficients to be independent of the spatial coordinates, which is not true in curvilinear coordinates. Later, true PMLs—in the sense of providing reflectionless absorption in the continuum limit—were derived for conformal (doubly-curved) mesh terminations [19], [3], based on a complex stretching (analytic continuation) of the normal coordinate to the mesh termination [16].

A conformal PML is of interest because it can be placed on the convex hull enclosing the antenna/scatterer(s) to reduce the amount of buffer space in the computational domain. The savings in memory can be considerable. The conformal PML can be expressed in terms of dispersive and anisotropic constitutive tensors $\bar{\bar{\epsilon}}(\vec{r})$ and $\bar{\bar{\mu}}(\vec{r})$ that depend on the *local* principal radii of curvature of the FEM mesh termination surface [19].

11.1.4 A PML-FDTD Algorithm for Dispersive, Inhomogeneous Media

In this section, we describe a PML-FDTD method suited for antenna problems in the presence of (possibly) dispersive and inhomogeneous media with conductive losses. This may be due, for example, to the presence of some dielectric or metamaterial dispersive loading and/or the proximity of the antenna to dispersive media such as some soils (as in ground-penetrating radar applications). The dispersion in the medium is characterized by multispecies Lorentz or Debye models and incorporated into the FDTD scheme via the use of the PLRC technique [2], [20]. We use the complex coordinate stretching PML formulation [16] to obtain the following modified Maxwell's equations ($e^{-j\omega t}$ convention)

$$\nabla_s \times \bar{E} = j\omega \bar{B} \tag{11-4}$$

$$\nabla_s \times \bar{H} = -j\omega \bar{D} + \sigma \bar{E} \tag{11-5}$$

where σ is the medium conductivity and

$$\nabla_s = \hat{x}\frac{1}{s_x}\frac{\partial}{\partial_x} + \hat{y}\frac{1}{s_y}\frac{\partial}{\partial_y} + \hat{z}\frac{1}{s_z}\frac{\partial}{\partial_z} \tag{11-6}$$

with $s_i = a_i + j\Omega_i/\omega$ (for $i = x, y, z$) being the frequency-dependent complex stretching variables (note that a_i and Ω_i are frequency-independent). Eqs. (11-4) and (11-5) are split as follows:

$$\frac{1}{s_x}\frac{\partial}{\partial_x}\hat{x}\times\bar{E} = j\omega\bar{B}_{sx} \tag{11-7}$$

$$\frac{1}{s_x}\frac{\partial}{\partial_x}\hat{x}\times\bar{H} = -j\omega\bar{D}_{sx} + \sigma\bar{E}_{sx}, \tag{11-8}$$

which can then be written as

$$\frac{\partial}{\partial_x}\hat{x}\times\bar{E} = j\omega a_x\bar{B}_{sx} - \Omega_x\bar{B}_{sx} \tag{11-9}$$

$$\frac{\partial}{\partial_x}\hat{x}\times\bar{H} = -j\omega a_x\bar{D}_{sx} + \Omega_x\bar{D}_{sx} + a_x\sigma\bar{E}_{sx} + j\frac{\Omega_x}{\omega}\sigma\bar{E}_{s} \tag{11-10}$$

In the time domain, the above become

$$\frac{\partial}{\partial_x}\hat{x}\times\bar{E} = -a_x\frac{\partial}{\partial_t}\bar{B}_{sx} - \Omega_x\bar{B}_{sx} \tag{11-11}$$

$$\frac{\partial}{\partial_x}\hat{x}\times\bar{H} = a_x\frac{\partial}{\partial_t}\bar{D}_{sx} + \Omega_x\bar{D}_{sx} + a_x\sigma\bar{E}_{sx} + \Omega_x\sigma\int_0^t\bar{E}_{sx}(\tau)d\tau \tag{11-12}$$

These equations are to be discretized both in time and space. However, before that, the dispersive medium characteristics need to be incorporated into these equations. This is carried out through the use of complex permittivity function, which results in the following magnetic and electric flux equations:

$$\bar{B}_{sx} = \mu\bar{H}_{sx} \tag{11-13}$$

$$\bar{D}_{sx} = \epsilon(t) *_t \bar{E}_{sx} \tag{11-14}$$

where $\epsilon(t) = \mathcal{F}^{-1}(\epsilon(\omega))$ is the N-species Lorentzian dispersive medium given by the following frequency-dependent relative permittivity function

$$\epsilon(\omega) = \epsilon_0[\epsilon_\infty + \chi(\omega)] \tag{11-15}$$

$$= \epsilon_0\epsilon_\infty + \epsilon_0(\epsilon_s - \epsilon_\infty)\sum_{m=1}^{N}\frac{G_m\omega_m^2}{\omega_m^2 - j2\omega\alpha_m - \omega^2} \tag{11-16}$$

where $\chi(\omega)$ is the medium susceptibility, ω_m is the resonant frequency for the mth species, α_m is the correspondent damping factor, and ϵ_0 and ϵ_∞ are the static and infinite frequency permittivities, respectively. A corresponding time-domain susceptibility function can be defined as

$$\hat{\chi}(t) = \sum_{m=1}^{N} \hat{\chi}_m(t) = \sum_{m-1}^{N} j\gamma_m e^{-(\alpha_m + j\beta_m)t} u(t) \tag{11-17}$$

where $\beta_m = \sqrt{\omega_m^2 - \alpha_m^2}$, $\gamma_m = (\epsilon_s - \epsilon_\infty)\omega_m^2 G_m / \beta_m$ and $\sum_{m=1}^{N} G_m = 1$. Note that $\chi(t) = \mathcal{F}^{-1}(\chi(\omega)) = \Re e(\hat{\chi}(t))$. Substituting (11-15) and (11-17) into (11-14) yields the following electric flux definition

$$\bar{D}(t) = \epsilon_0 \epsilon_\infty \bar{E}(t) + \epsilon_0 \chi(t) *_t \bar{E}(t) \tag{11-18}$$

$$\bar{D}(t) = \epsilon_0 \epsilon_\infty \bar{E}(t) + \epsilon_0 \sum_{m=1}^{N} \Re e\{\hat{\chi}(t) *_t \bar{E}(t)\}. \tag{11-19}$$

The electric field at $t = l\Delta t$ using the piecewise-linear approximation for the time discretization can be written as

$$\bar{E}(t) = \bar{E}^l + \frac{t - l\Delta_t}{\Delta_t}(\bar{E}^{l+1} - \bar{E}^l). \tag{11-20}$$

Once substituted into (11-19), we get

$$\bar{D}^l = \epsilon_0 \epsilon_\infty \bar{E}^l + \epsilon_0 \sum_{m=1}^{N} \Re e\left\{\bar{Q}_m^l\right\} \tag{11-21}$$

where

$$\bar{Q}_m^l = \sum_{p=0}^{l-1} \left[\left(\hat{\chi}_m^0 - \hat{\zeta}_m^0 \right) \bar{E}^{l-p} + \hat{\zeta}_m^0 \bar{E}^{l-p-1} \right] e^{-(\alpha_m + j\beta_m)p\Delta_t} \tag{11-22}$$

with the constants given as

$$\hat{\chi}_m^0 = \int_0^{\Delta_t} \hat{\chi}_m(t)dt = \frac{j\gamma_m}{\alpha_m + j\beta_m}\{1 - e^{-(\alpha_m + j\beta_m)\Delta_t}\} \tag{11-23}$$

$$\hat{\zeta}_m^0 = \int_0^{\Delta_t} t\hat{\chi}_m(t)dt = \frac{j\gamma_m}{\Delta_t(\alpha_m + j\beta_m)^2}\{1 - [(\alpha_m + j\beta_m)\Delta_t + 1]e^{-(\alpha_m + j\beta_m)\Delta_t}\}. \tag{11-24}$$

The following recursive calculation can be carried out for $\bar{Q}_m^l$

$$\bar{Q}_m^l = \begin{cases} 0 & l = 0 \\ \left(\hat{\chi}_m^0 - \hat{\zeta}_m^0 \right) \bar{E}^l + \hat{\zeta}_m^0 \bar{E}^{l-1} + \bar{Q}_m^{l-1} e^{-(\alpha_m + j\boldsymbol{\beta}_m)\Delta_t} & l \geq 0 \end{cases} \tag{11-25}$$

Once this is substituted in Eq. (11-21), we obtain the following update equation for the electric flux:

$$\bar{D}^l = \underbrace{\epsilon_0\left(\epsilon_\infty + \sum_{m=1}^{N} \Re e\left(\hat{\chi}_m^0 - \hat{\zeta}_m^0\right)\right)}_{\lambda_0}\bar{E}^l + \underbrace{\epsilon_0 \sum_{m=1}^{N} \Re e\left(\hat{\zeta}_m^0\right)}_{\lambda_1}\bar{E}^{l-1} + \underbrace{\epsilon_0 \sum_{m=1}^{N} \Re e\left(\bar{Q}_m^{l-1} e^{-(\alpha_m + j\beta_m)\Delta_t}\right)}_{\bar{P}^{l-1}} \tag{11-26}$$

$$\bar{D}^l = \epsilon_0\left(\lambda_0 \bar{E}^l + \lambda_1 \bar{E}^{l-1} + \bar{P}^{l-1}\right)$$

Note that in this equation, $\bar{P}^{l-1}$ depends only on $\bar{Q}_m^{l-1}$.

At this point, we need to apply both time-stepping and space discretization schemes for (11-11) and (11-12). The space discretization follows the conventional Yee's staggered-grid scheme with a central-difference approximation for the derivatives [8]. The time discretization for them becomes

$$\frac{\partial}{\partial_x}\hat{x} \times \bar{E}^l = -a_x \Delta_t^{-1}\left(\bar{B}_{sx}^{l+1/2} - \bar{B}_{sx}^{l-1/2}\right) - \Omega_x \bar{B}_{sx}^{l+1/2} \tag{11-27}$$

$$\frac{\partial}{\partial_x}\hat{x} \times \bar{H}^{l+1/2} = a_x \Delta_t^{-1}\left(\bar{D}_{sx}^{l+1} - \bar{D}_{sx}^{l}\right) + \Omega_x \bar{D}_{sx}^{l+1} + a_x \sigma \bar{E}_{sx}^{l+1} + \sigma \Omega_x \bar{F}_{sx}^{l}, \tag{11-28}$$

where $\bar{F}_{sx}^l = \bar{F}_{sx}^l(l\Delta_t) = \int_0^{l\Delta_t} \bar{E}(\tau)d\tau$. These equations can be arranged to give the time-stepping scheme as

$$\bar{B}_{sx}^{l+1/2} = -(a_x + \Omega_x \Delta_t)^{-1}\left(\Delta_t \frac{\partial}{\partial_x}\hat{x} \times \bar{E}^l - a_x \bar{B}_{sx}^{l-1/2}\right) \tag{11-29}$$

and

$$(a_x + \Omega_x \Delta_t)\bar{D}_{sx}^{l+1} + a_x \sigma \Delta_t \bar{E}_{sx}^{l+1} = \Delta_t\left(\frac{\partial}{\partial_x}\hat{x} \times \bar{H}^{l+1/2}\right) + a_x \bar{D}_{sx}^{l} - \sigma \Omega_x \Delta_t \bar{F}_{sx}^{l}. \tag{11-30}$$

Since the left-hand side of (11-31) depends both on $\bar{D}_{sx}^{l+1}$ and $\bar{E}_{sx}^{l+1}$, it is not suited for time-stepping. However, substituting (11-26) into (11-31), we have

$$\begin{aligned}\left((a_x + \Omega_x \Delta_t)\lambda_0 \epsilon_0 + a_x \sigma \Delta_t\right)\bar{E}_{sx}^{l+1} = {} & \Delta_t\left(\frac{\partial}{\partial_x}\hat{x} \times \bar{H}^{l+1/2}\right) + a_x \bar{D}_{sx}^{l} - \sigma \Omega_x \Delta_t \bar{F}_{sx}^{l} \\ & - (a_x + \Omega_x \Delta_t)\epsilon_0\left(\lambda_1 \bar{E}_{sx}^{l} + \bar{P}_{sx}^{l}\right)\end{aligned} \tag{11-31}$$

where $\bar{E}_{sx}^{l+1}$ can be updated in an explicit time-stepping. This is also used for updating of $\bar{B}_{sx}^{l+1/2}$ and $\bar{H}_{sx}^{l+1/2}$. The other quantities are updated as follows

$$\bar{D}_{sx}^{l} = \epsilon_0\left(\lambda_0 \bar{E}_{sx}^{l} + \lambda_1 \bar{E}_{sx}^{l-1} + \bar{P}_{sx}^{l-1}\right) \tag{11-32}$$

$$\bar{F}_{sx}^{l} = \bar{F}_{sx}^{l-1} + 0.5\Delta_t\left(\bar{E}_{sx}^{l} + \bar{E}_{sx}^{l-1}\right) \tag{11-33}$$

$$\bar{Q}_{m,sx}^{l} = \left(\hat{\chi}_m^0 - \hat{\zeta}_m^0\right)\bar{E}_{sx}^{l} + \hat{\zeta}_m^0 \bar{E}_{sx}^{l-1} + \bar{Q}_{m,sx}^{l-1} e^{-(\alpha_m + j\beta_m)\Delta_t} \tag{11-34}$$

$$\bar{P}_{sx}^{l} = \sum_{m=1}^{N} \Re e\left(\bar{Q}_{m,sx}^{l} e^{-(\alpha_m + j\beta_m)\Delta_t}\right). \tag{11-35}$$

This scheme is then repeated for y and z by replacing them with x. This constitutes the complete FDTD algorithm for use in antenna problems involving dispersive and lossy media. Another variants of this algorithm can be constructed as well. For example, the above PML implementation relied on a field-splitting, akin to the original PML formulation of Berenger [15]. There are also alternative, unsplit formulations of the PML that are attractive for being strongly well-posed and that can be adapted for inhomogeneous, dispersive media as well, as illustrated for example in [2].

11.1.5 A PML-FETD Algorithm for Dispersive, Inhomogeneous Media

We next illustrate a mixed FETD algorithm for application to UWB antenna problems that also allows for a simple implementation of the dispersive and anisotropic tensors that comprise the conformal PML. In this algorithm, the time update procedure associated with the constitutive relations can be derived and implemented separately from the update procedure associated with Maxwell curl equations. The conformal PML implementation boils down to a modification in the calculation of the two Hodge (mass) matrices $[\star_\epsilon]$ and $[\star_{\mu^{-1}}]$ [3].

The derivation of this algorithm starts by expanding electric field intensity $\bar{E}$ and the magnetic field flux density $\bar{B}$ in terms of Whitney *edge* elements $\bar{W}_i^1, i = 1,\ldots,N_e$, and Whitney *face* elements $\bar{W}_i^2, i = 1,\ldots,N_f$, respectively, as follows

$$\bar{E} = \sum_{i=1}^{N_e} e_i \bar{W}_i^1 \qquad \bar{B} = \sum_{i=1}^{N_f} b_i \bar{W}_i^2, \tag{11-36}$$

where e_i and b_i are the unknown expansion coefficients or degrees of freedom (DoFs) of the problem, N_e is the number of interior (free) edges in the problem, and N_f is the number of faces, respectively. If we define column vectors of DoFs as $\mathbb{E} = [e_1, e_2, \ldots, e_{N_e}]^T$ and $\mathbb{B} = [b_1, b_2, \ldots, b_{N_f}]^T$, where the superscript denotes transpose, the semidiscrete Maxwell equations can be written as [3]

$$[\star_\epsilon]\frac{\partial}{\partial t}\mathbb{E} = [\mathcal{D}^*_{\text{curl}}][\star_{\mu^{-1}}]\mathbb{B} - \mathbb{J}_s \tag{11-37}$$

$$\frac{\partial}{\partial t}\mathbb{B} = -[\mathcal{D}_{\text{curl}}]\mathbb{E} - \mathbb{M}_s \tag{11-38}$$

where the $N_f \times N_e$ matrix $[\mathcal{D}_{\text{curl}}]$ and the $N_e \times N_f$ matrix $[\mathcal{D}^*_{\text{curl}}]$ are *curl incidence matrices* (discrete analogues of the exterior derivative d acting on 1-forms) on the primal and dual grids, respectively [21]). The primal grid is chosen as the finite-element mesh itself. Both $[\mathcal{D}_{\text{curl}}]$ and $[\mathcal{D}^*_{\text{curl}}]$ are metric-free matrices whose elements assume only {–1, 0, 1} values. Up to boundary terms, we have $[\mathcal{D}^*_{\text{curl}}] = [\mathcal{D}_{\text{curl}}]^T$ [21]. The column vectors $\mathbb{J} = [\mathrm{j}_1, \mathrm{j}_2, \ldots, \mathrm{j}\, N_e]^T$ and $\mathbb{M} = [\mathrm{m}_1, \mathrm{m}_2, \ldots, m_{N_f}]^T$ represent (known) electric and magnetic source current densities, respectively. The column vector $\mathbb{M}$ is associated with faces of the primal (finite-element) mesh, while $\mathbb{J}$ is associated with faces of the (implicit) dual mesh [21]. The $N_e \times N_e$ matrix $[\star_\epsilon]$ and the $N_f \times N_f$ matrix $[\star_{\mu^{-1}}]$ represent discrete Hodge star operators, an isomorphism between primal grid variables and dual-grid variables that incorporate all metric information of the mesh [21]. In the finite-element literature, these matrices are commonly referred as *mass* matrices.

Using a leap-frog time discretization in (11-37) and (11-38), the FETD update equations become

$$[\star_\epsilon]\mathbb{E}^{n+1} = [\star_\epsilon]\mathbb{E}^n + \Delta t[\mathcal{D}_{curl}]^T[\star_{\mu^{-1}}]\mathbb{B}^{n+\frac{1}{2}} - \Delta t\mathbb{J}_s^{n+\frac{1}{2}} \tag{11-39}$$

$$\mathbb{B}^{n+\frac{1}{2}} = \mathbb{B}^{n-\frac{1}{2}} - \Delta t[\mathcal{D}_{curl}]\mathbb{E}^n - \Delta t\mathbb{M}_s^n. \tag{11-40}$$

The solution for $\mathbb{E}$ and $\mathbb{B}$ at each time step can be obtained by solving a sparse linear system for $\mathbb{E}$ for each n. Since $[\star_\epsilon]$ is sparse and symmetric positive-definite, the linear solve can be done efficiently using direct (for small- and moderate-size problems) or iterative (for large-scale problems) solvers. The above update equations are similar to the leap-frog update equations in FDTD, except for the fact that in the latter case, $[\star_\epsilon]$ is diagonal and the inversion is trivial.

If we denote i and j as the row and column indices respectively, the (Galerkin) Hodge matrices are given by the following volume integrals

$$[\star_\epsilon]_{ij} = \int_\Omega \bar{W}_i^1 \cdot \bar{\bar{\epsilon}}(\bar{r}) \cdot \bar{W}_j^1 d\Omega \tag{11-41}$$

$$[\star_{\mu^{-1}}]_{ij} = \int_\Omega \bar{W}_i^2 \cdot \bar{\bar{\mu}}^{-1}(\bar{r}) \cdot \bar{W}_j^2 d\Omega, \tag{11-42}$$

along the support where Ω of the basis functions.

Inside the PML, the above permittivity and permeability tensors are functions of frequency: $\bar{\bar{\epsilon}}(\bar{r},\omega)$ and $\bar{\bar{\mu}}(\bar{r},\omega)$, as they depend on complex stretching variables that are frequency-dependent. As a result, the update of the time-domain constitutive equations require the use of techniques such as PLRC or ADE described before. Reference [3] provides a description of the implementation of the ADE technique to discretize (11-41) and (11-42) in the FETD algorithm. Of course, the PLRC or ADE techniques can also be utilized when dispersive media (dielectrics, metamaterials) are present within the physical domain [12].

11.1.6 Examples

11.1.6.1 UWB Dielectric Horn Antenna

For detection of shallow objects by ground-penetrating radar (GPR) where high sensitivity is not an issue, elevated antennas are often used for easier scanning and better calibration. On the other hand, most GPR antennas used for the detection of deep targets are operated close to the ground so that most of the energy is radiated into the ground. However, characteristics of such GPR antennas while in field operation are typically difficult to determine a priori because of the large coupling with the environment. This also makes calibration quite difficult. Dielectric horn antennas are good candidates to make antenna characteristics less susceptible to ground effects because the feed system is naturally elevated. Moreover, apart from truncation effects, the geometry of dielectric horn antennas is self-similar and hence they are good candidates for UWB operation [4].

Figure 11-1 shows the geometry of the feed system with the two-arm metallic plate launchers and a detail of the FDTD grid used at the feed point of the dielectric horn antenna UWB antenna considered. This feed system is truncated and the space between the metallic plates is filled with a pyramidal dielectric horn with relative permittivity $\epsilon_r = 5$. The FDTD grid discretization of the dielectric horn is illustrated in Fig. 11-2.

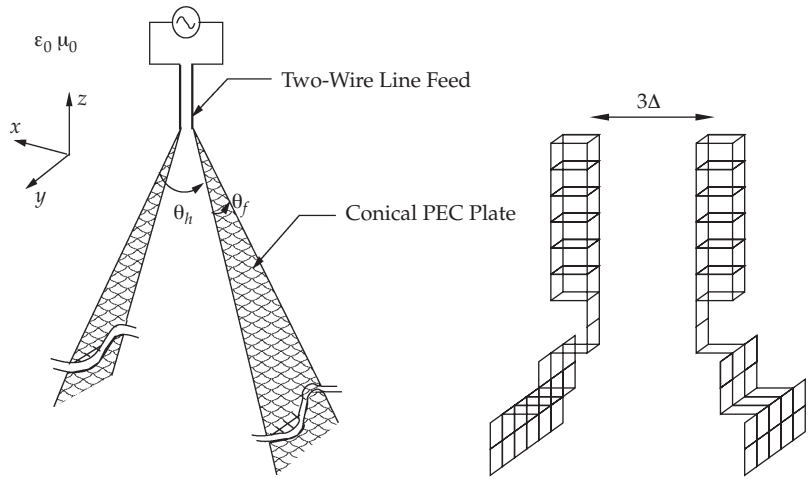

Figure 11-1 (a) Geometry of the metallic arm feeds of the UWB dielectric horn antenna, where the space between the arms is filled with a pyramidal dielectric horn. (b) Detail of the FDTD-grid discretization of the two-wire feed systems and coupling with the two metallic arms feeds.

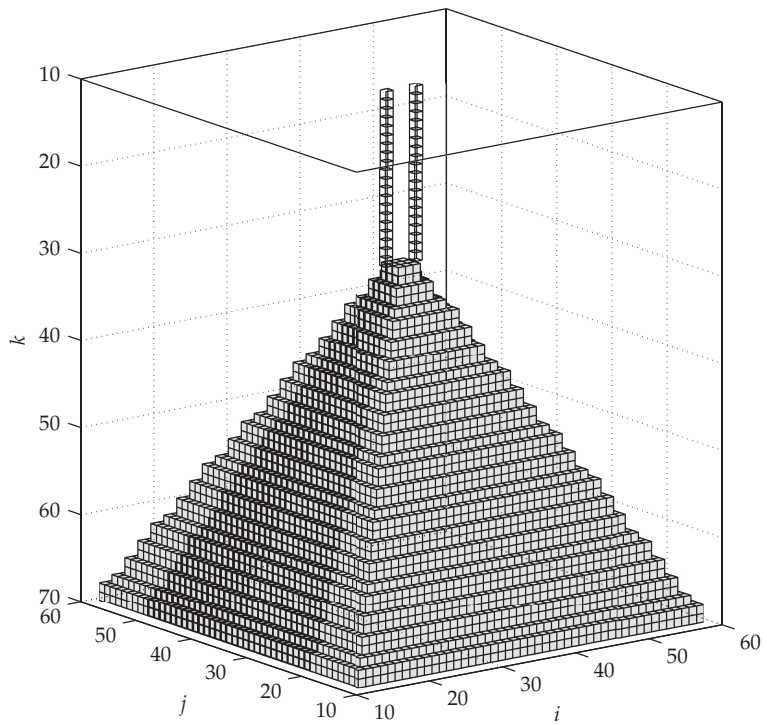

Figure 11-2 FDTD-grid discretization of the dielectric horn and the two opposite-side metallic arm feeders

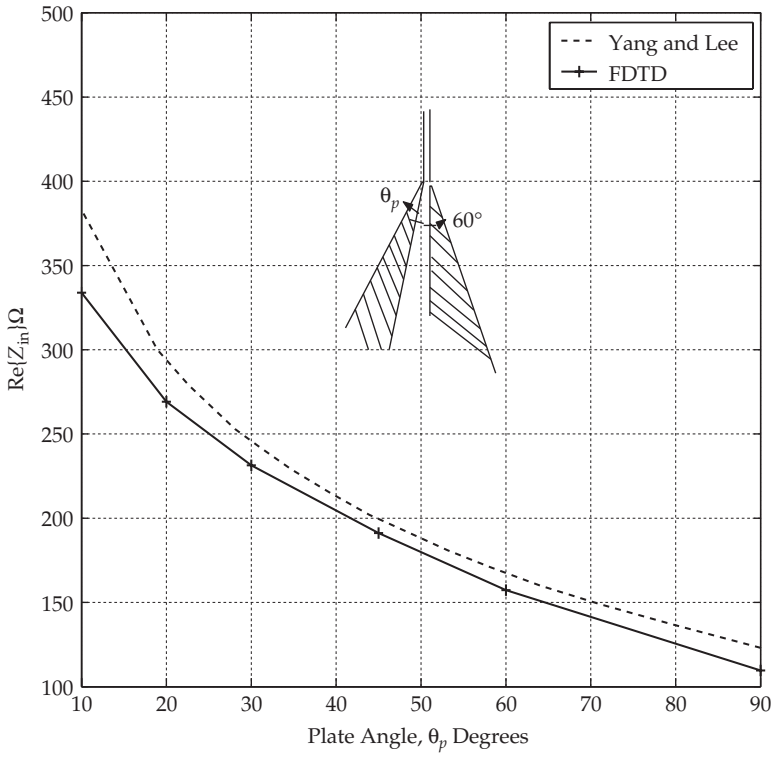

Figure 11-3 Comparison of the input impedance of the two-arm feed system, computed by FDTD and by an analytical approach. The flare angle is $\theta_h = 60$ degrees, and various plate angles are considered.

Figure 11-3 compares the input impedance (real part) of the two-arm feed system computed by FDTD, for various plate angles and for flare angle $\theta_h = 60$ degrees, against analytical results [22]. Figure 11-4 shows the input impedance of the dielectric horn antenna versus frequency computed by FDTD. The dielectric load has relative permittivity $\epsilon_r = 4$ in this case. The input impedance shows little variation in the 500 MHz to 2 GHz range [4].

11.1.7 Dual-Polarized UWB-HFBT Antenna

Bow-tie antennas are also widely used for UWB applications. To reduce ground susceptibility in GPR applications, bow-tie antennas can be fed by a dielectric horn feed similar the one previously discussed. Moreover, a four arm consideration can be adopted to allow for dual-polarization (polarimetric) operation.

Figure 11-5 shows the geometry of a dual-polarized UWB horn-fed bow-tie (HFBT) antenna designed for GPR operation [5]. This is somewhat similar to a planar bow-tie dipole with the feed point now being raised off the ground. This reduces the sensitivity of the surge impedance to ground properties. Each antenna arm is smoothly curved in the transition from the horn section to the planar bow-tie dipole section. The ends of the

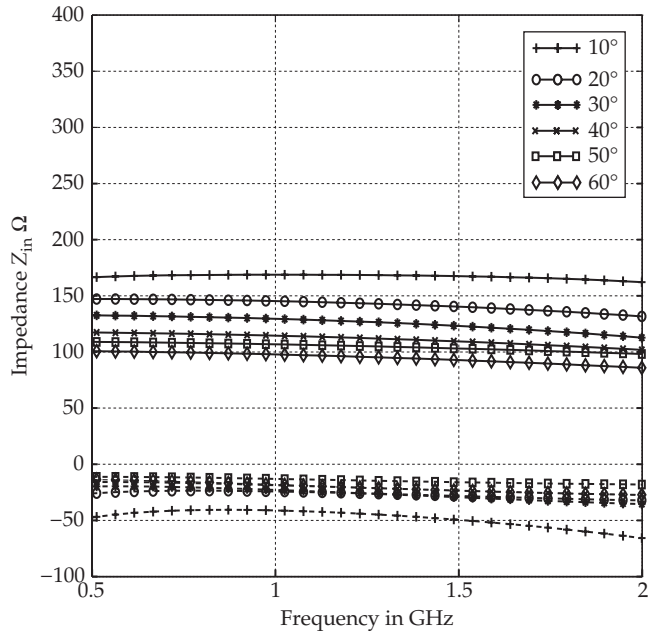

Figure 11-4 Input impedance of the horn-fed bow-tie antenna versus frequency computed by FDTD, for flare angle $\theta_h = 60$ degrees and various plate angles (Source:[4], ©IEEE, 2004)

dipoles are terminated with tapered resistive cards (R-cards). The objective of the R-cards is to reduce reflections by gradually dissipating the currents propagating toward the end of each antenna arm. This increases the antenna bandwidth. The prototype considered here has a dielectric horn with $\epsilon_r = 5$. The plate angle of each antenna arm is 11.5 degrees. The horn angle itself is approximately 150 degrees.

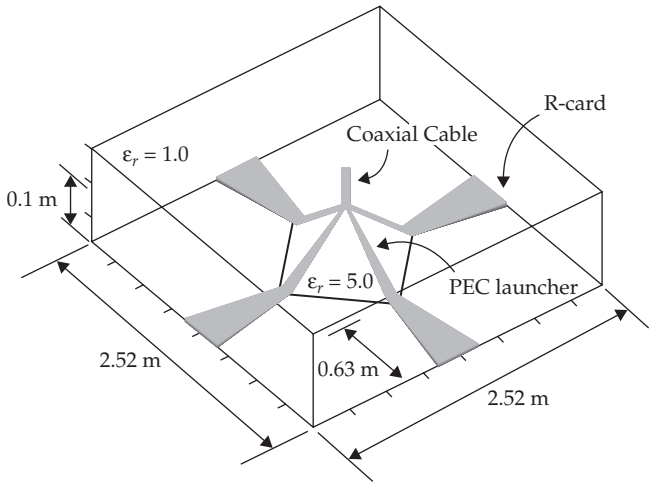

Figure 11-5 Illustration of the UWB-HFBT antenna geometry and dimensions

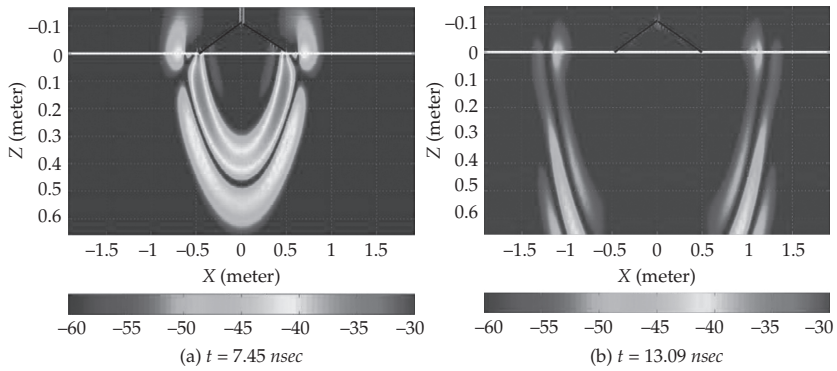

Figure 11-6 FDTD simulation snapshots of the electric field strength in dB scale with R-card attached

A full scale FDTD model of the UWB HFB antenna prototype requires computational grid spanning a minimum of 2.5 m × 2.5 m × 0.63 m space. A spatial cell size of 6.3 mm was chosen to accurately model the geometrical details of the antenna and cable structure [5]. This yields a grid with approximately 96 million unknowns. The four antenna arms were modeled as perfect electric conducting (PEC) plates, and the curved edges and surfaces were approximated by staircases. Each tapered R-card attached to the end of the PEC arm is 63 cm in length and is implemented via a conductive sheet in FDTD. The ground was assumed to be a lossless half space with $\epsilon_r = 5$.

Figure 11-6 shows side-view snapshots, computed by FDTD, of the field distribution of this antenna launched into the ground at two different time instants: $t = 7.45$ nsec and $t = 13.09$ nsec [5]. Figure 11-7 shows snapshots at the same time instants for the same antenna geometry except that the R-cards are now absent. The ringing effect from the antenna terminations and the perturbation of the field distribution are clearly visible in Fig. 11-7. In general, FDTD models provide very useful visualization of dynamic field distributions that can help identify undesired radiation and reflection sources.

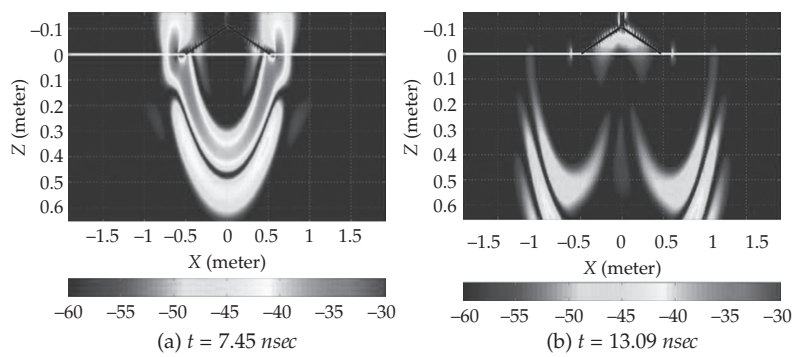

Figure 11-7 FDTD simulation snapshots of the electric field strength in dB scale without R-card attached

11.1.8 Time-Domain Modeling of Metamaterials

In recent years, there has been an upsurge in the design and development of new materials under the conceptual umbrella of "metamaterials," as they show great promise to expand the design space of RF and optical devices and antennas. FDTD and FETD have proved to be quite effective tools for the analysis of metamaterials.

One interesting periodic material arrangement that provides a photonic crystals (PhCs) with a degenerate band edge (DBE) is shown in Fig. 11-8a. In this arrangement, the unit cell has two misaligned anisotropic dielectric layers, A_1 and A_2, and one isotropic layer *B*. The dispersion relation can be tailored in order to produce a degenerate band edge by adjusting the thickness and permittivity of each layer. DBE PhCs can be designed to yield a (approximately) quartic dispersion relation just below the DBE frequency rather than the conventional quadratic dispersion relation present below a regular band edge (RBE). Fabry-Perot resonances (associated with narrowband transmission peaks) can be exploited in finite-size slabs made of such periodic stacks. Finite-size DBE PhCs are able to produce gigantic amplitude increase at Fabry-Perot resonances that have very good transmittance (matching) properties, which can be exploited by antennas operating in the resonance frequency [6].

Figure 11-8b shows the simulated transmission spectrum with the Fabry-Perot resonances below the DBE frequency, for $N = 8$ and $N = 16$, where N is the number of units cells. As N increases, the resonances move close to the DBE frequency (while the transmission bands are narrowed). As Fabry-Perot resonances move just below the band edge, a dramatic increase in field intensity is produced because of slow wave effects (decrease in the group velocity). Hence, larger N leads to greater growth in field intensity. Figure 11-9 shows the FETD computed field distribution squared inside this metamaterial. Note that because the group velocity is smaller below the DBE frequency (from the quartic dispersion relation) than the RBE frequency (from the quadratic dispersion relation), a much larger increase in the field amplitude is produced at DBE-based Fabry-Perot resonances than at the RBE counterpart for the same *N*.

Plasmon resonance structures have become the subject of intense study in recent years as potential building blocks of, among other devices, nanoantennas and (subwavelength) optical waveguides at the nanoscale (down to tens on nm). Localized

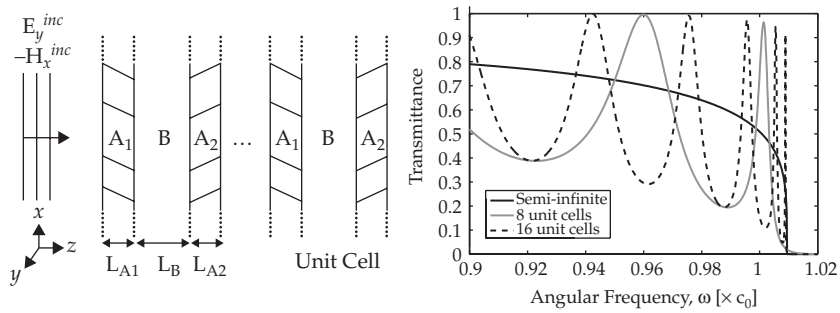

(a) Periodic DBE Crystal Arrangement (b) Transmittance Spectrum

Figure 11-8 (a) Schematic of a DBE-PhC composed of two anisotropic dielectric layers (*A*-layers) and one isotropic dielectric layer (*B*-layer). The dispersion relation can be tailored in order to produce a degenerate band edge by adjusting the thickness and permittivity of each layer. (b) Associated transmission spectrum for different number of unit cells *N* (Source: [6], © Am. Phys. Soc., 2008).

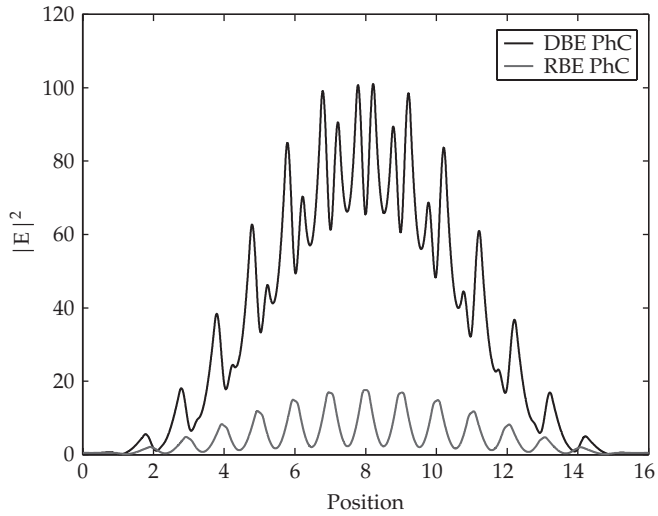

Figure 11-9 Steady-state (time-average) field intensity $|\mathbf{E}|^2$ inside a PhC with $N = 16$. The incident wave has unit amplitude. Increase in the field intensity is observed in DBE-PhC versus RBE-PhC (Source: [6], © Am. Phys. Soc., 2008).

surface plasmon resonances due to coherent electron oscillations excited at metal/dielectric interfaces yield highly localized field enhancement and provide guiding and confinement of electromagnetic waves well below the diffraction limit [7]. These structures are usually made of noble metals such as Ag and Au that exhibit dispersive response at optical frequencies, which can be modeled by ADE or PLRC techniques.

Figure 11-10 shows FDTD snapshots of the field intensity along a straight chain and a T-junction of a plasmon waveguide made of Au particles excited at center frequency of 580 THz. The excitation is a dipole located the left end of the waveguide. The particles

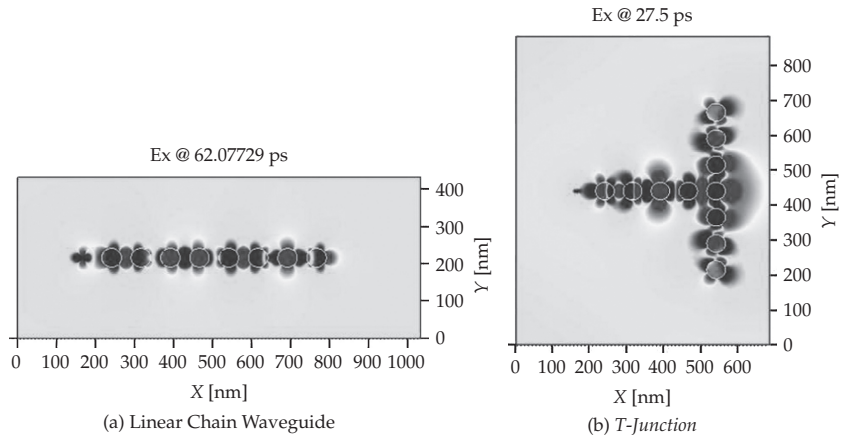

Figure 11-10 (a) Snapshot of the field distribution computed along a linear chain plasmon waveguide at 516 nm. (b) Snapshot of the field distribution computed along a T-junction (see text for details).

are nanospheres with radius 25 nm and center-to-center spacing of 75 nm. The FDTD grid cell size has 1.5625 nm; $640 \times 256 \times 256$ cells are used for straight chain and $448 \times 544 \times 256$ cells for T-junction simulations. A Drude model is used to model the Au dielectric response in the frequency range considered. The corresponding wavelength is 516 nm, i.e., deep subwavelength guiding is achieved by these waveguides of lateral dimension 50 nm.

11.2 Frequency-Domain FEM

Geometrical and material modeling flexibility of the FEM, has made it one of the most versatile design tools for modern antenna engineering. Recent advances in FEM modeling, coupled with fast and robust solution methods and general purpose mesh generation/graphical interface tools, have been instrumental in the proliferation of several commercial FEM packages in the past decade. Today, such commercial software are the antenna engineers' most efficient tools in tackling modern antenna design challenges. In this section, we outline the basic components of the FEM and summarize some of the aspects that makes it a popular design tool for antenna engineering (see e.g., [23]–[26], [10] on FEM for antenna analysis).

The partial differential equations (PDEs) that govern *"wave phenomena"* is of particular interest to the antenna engineer for obvious reasons. Since a full review of Maxwell's equations is beyond the scope of this chapter, we will simply focus on the time-harmonic wave equation to outline the FEM.

11.2.1 Weak Formulation of Time-Harmonic Wave Equation

In order to develop time harmonic FEM formulation, we will start by introducing the so-called "weak formulation" of the wave equation. For completeness, Maxwell equations in frequency domain (an $e^{-i\omega t}$ time convention is assumed and suppressed) are

$$\nabla \times \mathbf{E} = i\omega \mathbf{B}, \quad \nabla \times \mathbf{H} = -i\omega \mathbf{D} + \mathbf{j}, \quad \nabla \cdot \mathbf{D} = \rho_e, \quad \nabla \cdot \mathbf{B} = 0, \tag{11-43}$$

where $\mathbf{E}$ and $\mathbf{H}$ are the electric and magnetic field intensities, and $\mathbf{D}$ and $\mathbf{B}$ are the electric and magnetic flux densities, respectively. Also, $\mathbf{J}$ denotes the electric current density and ρ_e is the electric charge density (related to electric current density via the continuity equation $\nabla \cdot \mathbf{J} = i\omega\rho_e$). In addition, for linear anisotropic media, the electric and magnetic field intensities and flux densities are related through constitutive parameters, viz. $\mathbf{D} = \bar{\bar{\epsilon}} \cdot \mathbf{E}$ and $\mathbf{B} = \bar{\bar{\mu}} \cdot \mathbf{H}$.

The wave equation for the electric field intensity is constructed by coupling Maxwell's curl equations for the electric and magnetic field intensities. Namely, by taking the curl of Maxwell's first equation ($\nabla \times \nabla \times \mathbf{E} = i\omega \nabla \times \mathbf{B}$) and then substituting Maxwell's second equation (along with the constitutive relation $\mathbf{B} = \bar{\bar{\mu}} \cdot \mathbf{H}$), we arrive at

$$\nabla \times \bar{\bar{\mu}}^{-1}(\mathbf{r}) \cdot \nabla \times \mathbf{E}(\mathbf{r}) - \omega^2 \bar{\bar{\epsilon}}(\mathbf{r}) \cdot \mathbf{E}(\mathbf{r}) = i\omega \mathbf{J}^i(\mathbf{r}) \tag{11-44}$$

where $\omega = 2\pi f$ denotes the angular frequency. In (11-44), $\mathbf{J}^i(\mathbf{r})$ represents the impressed excitations within the solution domain v. We remark that the right-hand side of (11-44) vanishes for source-free regions. A similar "dual" equation can also be obtained for the magnetic field intensity $\mathbf{H}(\mathbf{r})$.

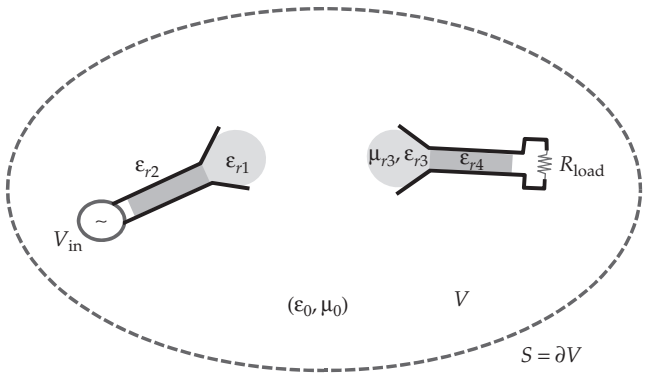

Figure 11-11 Representation of a typical antenna problem involving multiple antennas and material regions

Equation (11-44) is a strong, point-wise condition that the electric field intensity **E** must satisfy at all locations **r** within the domain of a given problem.

In general, as seen in Fig. 11-11, the solution domain may contain perfectly conducting and/or lossy surfaces, impedance boundaries, and homogeneous-isotropic/anisotropic materials, as well as inhomogeneous material regions. The versatility of the FEM stems from (11-44) in which material properties (e.g., linear, inhomogeneous, and anisotropic) are explicitly expressed.

Although as simple and as general (11-44) is, it is a mathematically strong statement whose solution cannot be readily obtained for arbitrary antenna geometries. However, this strong statement can be relaxed by seeking approximate field solutions that satisfy (11-44) in an average sense. Such an approximate form of (11-44) is mathematically called the "weak form."

In order to relax the point-wise statement of (11-44), we proceed by defining auxiliary functions that will help us measure the error between the right- and left-hand sides of (11-44). Using a suitable inner product (please see [23], [10], [27]–[30] for a rigorous treatment) defined over the domain of the electric field **E** and a set of testing functions $\mathbf{W} = \{\mathbf{w}_j, j = 1, \ldots, N\}$, we can rewrite (11-44) as

$$\int_v dv \mathbf{W} \cdot \left\{ \nabla \times \nabla \times \mathbf{E} - k_0^2 \mathbf{E} \right\} = i\omega\mu \int_v dv \mathbf{W} \cdot \mathbf{J}^i \tag{11-45}$$

where, for the sake of simplicity, we consider a linear, isotropic, and piecewise homogeneous domain, and the implicit **r** dependence is understood.

Our next step is to relax the double differentiation (i.e., double curl operation) requirement in (11-45). This is simply done using the vector identity

$$\nabla \cdot (\mathbf{A} \times \mathbf{B}) = (\nabla \times \mathbf{A}) \cdot \mathbf{B} - \mathbf{A} \cdot (\nabla \times \mathbf{B}), \tag{11-46}$$

with $\mathbf{A} = \mathbf{W}$ and $\mathbf{B} = \nabla \times \mathbf{E}$, and (11-45) can be written as

$$\int_v dv \nabla \cdot \{\mathbf{W} \times (\nabla \times \mathbf{E})\} - \int_v dv (\nabla \times \mathbf{W}) \cdot (\nabla \times \mathbf{E}) - k_0^2 \int_v dv \mathbf{W} \cdot \mathbf{E} = i\omega\mu \int_v dv \mathbf{W} \cdot \mathbf{J}^i. \tag{11-47}$$

Next, Gauss theorem is applied to the first term of (11-47), which results in the weak form of the wave equation

$$\int_v dv(\nabla \times \mathbf{W}) \cdot (\nabla \times \mathbf{E}) - k_0^2 \int_v dv \mathbf{W} \cdot \mathbf{E} - \oint_{s=\partial v} ds\hat{n} \cdot \{\mathbf{W} \times (\nabla \times \mathbf{E})\} = i\omega\mu \int_v dv \mathbf{W} \cdot \mathbf{J}^i. \quad (11\text{-}48)$$

In (11-48), $\hat{n}$ in the outward normal vector on the boundary $s = \partial v$. The surface integral can further be simplified using the vector identity

$$\hat{n} \cdot (\mathbf{A} \times \mathbf{B}) = \mathbf{A} \cdot (\mathbf{B} \times \hat{n}) = \mathbf{B} \cdot (\hat{n} \times \mathbf{A}), \quad (11\text{-}49)$$

resulting in the alternative expression

$$\int_v dv(\nabla \times \mathbf{W}) \cdot (\nabla \times \mathbf{E}) - k_0^2 \int_v dv \mathbf{W} \cdot \mathbf{E} + \oint_s ds \mathbf{W} \cdot \hat{n} \times (\nabla \times \mathbf{E}) = i\omega\mu \int_v dv \mathbf{W} \cdot \mathbf{J}^i. \quad (11\text{-}50)$$

The weak statements (11-48) and (11-50) must now be satisfied for a set of testing functions **W**. Hence, unlike (11-45), an approximate solution for **E** can be computed via the FEM.

It is also interesting to note that if we choose our testing function **W** to be the same as the electric field **W** = **E** (Galerkin testing, see [23], [10]), (11-48) becomes an energy conservation statement

$$\int_v dv(\nabla \times \mathbf{E}) \cdot (\nabla \times \mathbf{E}) - k_0^2 \int_v dv \mathbf{E} \cdot \mathbf{E} = i\omega\mu \oint_s ds\hat{n} \cdot (\mathbf{E} \times \mathbf{H}) + i\omega\mu \int_v dv \mathbf{E} \cdot \mathbf{J}^i \quad (11\text{-}51)$$

where the left-hand side is the total electric and magnetic energy contained in v and the right-hand side is the total power crossing s and power delivered into the volume by the impressed source.

The FEM seeks solutions to (11-48) and (11-50), which are weaker statements than (11-44), i.e., they are satisfied in an average sense over the whose solution space v. Thus, solutions **E** to (11-48) may not necessarily satisfy the original wave equation (11-44) exactly, only approximately. The construction of (11-48), starting from (11-44) and imposing (11-45) is called the weighted residuals method. Galerkin's method, or Galerkin's testing belongs to this family when the weighting functions is chosen to be the same as the unknown function, as was done in arriving at (11-51). Alternatively, one can arrive at the same weak form statement (also called the variational statement) through the Rayleigh-Ritz procedure, by minimizing the functional associated with the wave equation. Due to space limitations, the reader is referred to [23], [10] for more information on the functional approach in constructing the variational statement.

In the following, we seek solutions to the electric field intensity **E** in the domain v that satisfy (11-48) exactly, thus (11-44) weakly. Obviously, we can start by assuming a solution **E** and test (by choosing suitable testing functions **W**) whether this solution satisfies (11-48). However, since we can have infinitely many choices for assuming a solution **E**, this approach would rather inefficient. Alternatively, we may introduce a tessellation of the problem domain v via a connected mesh of simple shapes (triangular or quadrilateral finite elements for two-dimensional (2D) problems and tetrahedral or

hexahedral finite elements for 3D) and express the unknown electric field intensity **E** as a sum of known functions with unknown coefficients, viz.

$$\mathbf{E}(\mathbf{r}) = \sum_{i=1}^{N} a_i \mathbf{e}_i(\mathbf{r}). \tag{11-52}$$

The *"basis"* functions, $\{\mathbf{e}_i, i = 1, \ldots, N\}$, are defined on the finite elements in terms of the local coordinates (to facilitate concise universal expressions). They should also respect the properties of the unknown electric field **E**. For instance, the vector-field nature of **E** should be respected by the choice of $\mathbf{e}_i$ and conditions, such as $\nabla \times \mathbf{e}_i$ being well-defined must be satisfied.

Tetrahedral, hexahedral, and triangular-prism elements and associated basis functions are the most popular 3D finite elements used in antenna engineering. In the following section, we briefly summarize the usual 2D and 3D finite elements.

11.2.2 Geometry Modeling and Finite-Element Representations

As noted above, the first step in implementing the FEM to analyze a radiating structure is to approximate the antenna geometry and the surrounding solution domain v by a connected mesh of geometrically simple elements (see Fig. 11-12). This mesh forms an approximation to the solution domain, and basis functions are expressed directly on the mesh elements. Some popular choices for 2D elements are depicted in Fig. 11-13, and those for 3D elements are shown in Fig. 11-14. For example, a 2D triangular element is defined by its three vertices $\mathbf{r}_1$, $\mathbf{r}_2$, $\mathbf{r}_3$, as shown in Fig. 11-15. Any point **r** inside the element has the barycentric coordinates $(\zeta_1, \zeta_2, \zeta_3)$ where ζ_i is defined with respect to the area of each subtriangle formed by connecting **r** to the vertices, viz. $\zeta_i = A_i/A$, where $A = A_1 + A_2 + A_3$ is the area of the triangle. Similarly, 4 barycentric variables can be constructed for tetrahedral elements.

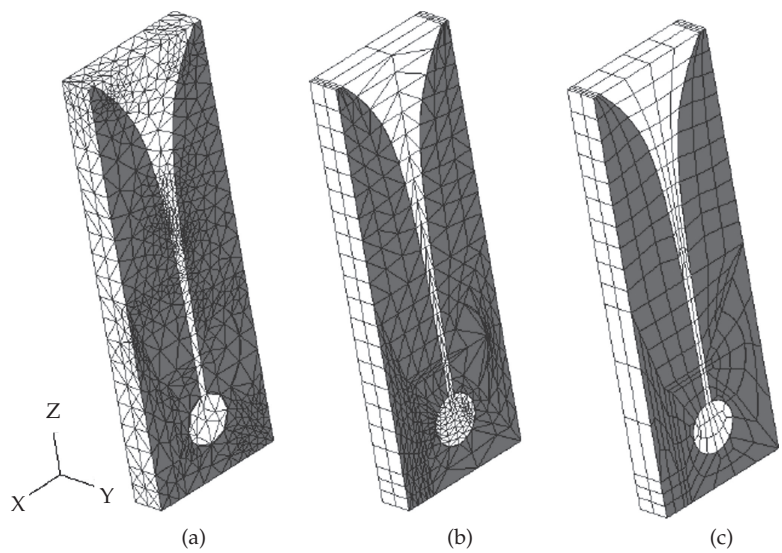

Figure 11-12 FEM meshes of the Vivaldi antenna using (a) tetrahedral elements, (b) triangular-prism elements, and (c) hexahedral elements

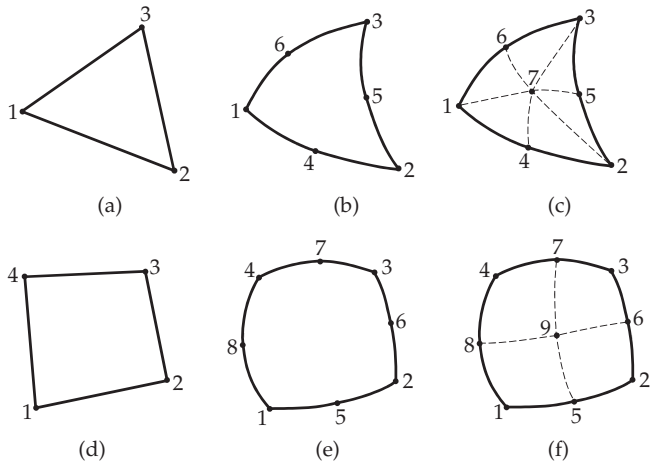

Figure 11-13 2D finite elements: (a) flat Triangular, (b) Curvilinear, 6-point triangular, (c) Curvilinear, 7-point triangular, (d) Flat, quadrilateral, (e) Curvilinear, 8-point quadrilateral, and (f) Curvilinear, 9-point quadrilateral.

Alternatively, we can also use a parametric representation of the elements. For instance, a 2D quadrilateral element defined by its 4 vertices as depicted in Fig 11-13c can be considered to be the map of a unit square in a (u, v) domain, viz. $r(u, v) = [x(u, v), y(u, v), z(u, v)]$. Here, the parametric transformation, are constructed such that the 4 corners of the unit square in the (u, v) space is mapped to the given 4 vertices of the quadrilateral, a.k.a. $\mathbf{r}_1 = \mathbf{r}(u = 0, v = 0)$, $\mathbf{r}_2 = \mathbf{r}(\mathrm{u} = 1, v = 0)$, $\mathbf{r}_3 = \mathbf{r}(u = 1, v = 1)$, and $\mathbf{r}_4 = \mathbf{r}(u = 0, v = 1)$. Both the barycentric $(\zeta_1, \zeta_2, \zeta_3)$ representations and the (u, v) parameterizations

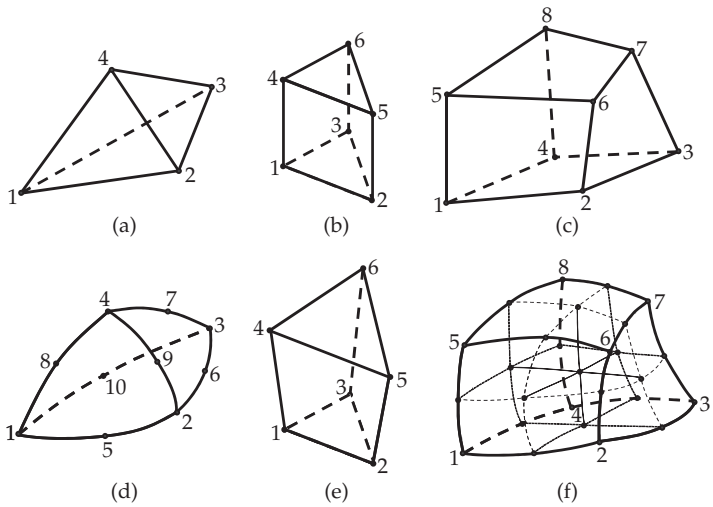

Figure 11-14 Popular 3D finite elements: (a) Tetrahedral, (b) Triangular prism (right angled), (c) Trilinear hexahedral (brick), (d) Curved tetrahedral, (e) Distorted prism, (f) Triquadratic, and hexahedral element.

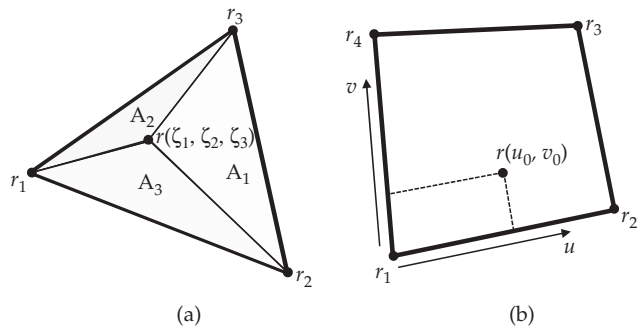

Figure 11-15 Parametric representations of 2D finite elements: (a) Barycentric coordinates for a triangular element, (b) (u, v) parametrization of a quadrilateral.

allow for simple expressions for the elements and the basis functions defined on these elements. This simplicity is particularly useful for implementation ease. Representations of 3D tetrahedral, hexahedral, and triangular-prism elements are summarized in the following subsections. Curvilinear versions of such elements can be found in various journal papers [31]–[33].

11.2.2.1 Tetrahedral Elements

The position vector **r** inside the tetrahedral element is given in terms of the 4 barycentric parameters, ζ_i, defined by connecting the position vector to the 4 vertices defining the element. Each barycentric variable is defined as $\zeta_i = V_i/V$, where V_i is the volume of the subtetrahedron defined by the position vector **r** and the face of the tetrahedron across the ith vertex, and V is the volume of the element $V = V_1 + V_2 + V_3 + V_4$ (see Fig. 11-16).

11.2.2.2 Hexahedral Elements

Much like the 2D quadrilateral elements, 3D hexahedra can be simply defined as a mapping of a unit cube in the parametric (u, v, w) space, viz.

$$\mathbf{r}(u,v,w) = \sum_{i=1}^{2}\sum_{j=1}^{2}\sum_{k=1}^{2} L_i(u)L_j(v)L_k(w)\mathbf{r}_{ijk} \tag{11-53}$$

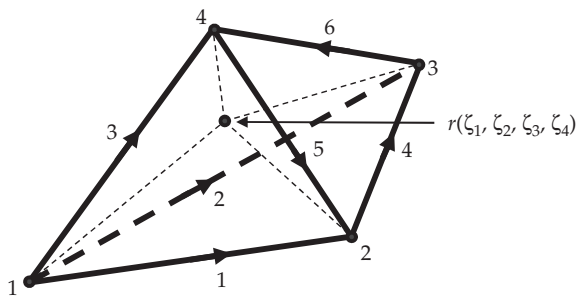

Figure 11-16 3D tetrahedral element

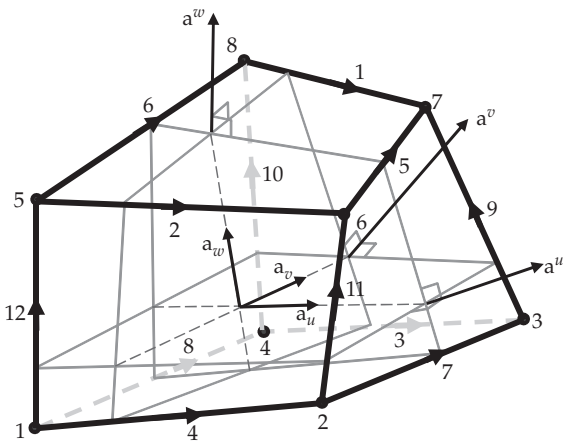

Figure 11-17 3D hexahedral element and the illustrations of covariant and contravariant basis vectors

where $\mathbf{r}_{ijk}$ $i = 1, 2$; $j = 1, 2$; and $k = 1, 2$ are the 8 vertices of the element as shown in Fig. 11-17. Also, $L_1(\tau) = \tau$ and $L_2(\tau) = 1 - \tau$, are the first-order Lagrange interpolators for $\tau = u, v, w$. We also note that for (11-53) to be valid, the vertices of the element must lie on a topologically rectangular grid.

11.2.2.3 Triangular-Prism Elements

The distorted triangular-prism element [34] shown in Fig. 11-18 can be represented in terms of the parametric height variable t in addition to the barycentric (ζ_1, ζ_2, ζ_3) coordinates of the triangular faces, viz.

$$\mathbf{r}(\zeta_1, \zeta_2, \zeta_3, t) = \{\mathbf{r}_1\zeta_1 + \mathbf{r}_2\zeta_2 + \mathbf{r}_3\zeta_3\}(1-t) + \{\mathbf{r}_1\zeta_4 + \mathbf{r}_5\zeta_2 + \mathbf{r}_6\zeta_3\}t \tag{11-54}$$

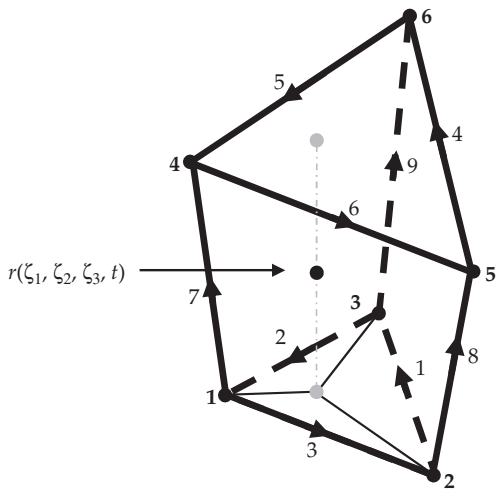

Figure 11-18 Triangular-prism element and the illustration of its parametric representation

where $\mathbf{r}_i$, $i = 1, \ldots, 6$ are the 6 vertices of the distorted prism. As a special case of the distorted prism element, the right-angled prism element is particularly useful in for layered media, often encountered in modeling antennas.

The previous definitions provide the mathematical tools to represent the finite elements. Next, we summarize some popular vector basis functions defined on these finite elements to express the electric field unknowns in FEM.

11.2.3 Vector Finite Elements

For programming simplicity, it is desirable to use low-order polynomial expressions to construct the basis functions. As such, the following are among the most widely utilized in FEM for antenna modeling [35].

11.2.3.1 Vector Basis Functions on Tetrahedra

Associated with each of the 6 edges of the tetrahedral element, we define 6 basis functions expressed in terms of the barycentric coordinates. Assuming a local edge numbering given in Table 11-1, the basis function associated with the kth edge is given as

$$\mathbf{e}_k = l_{ij}(\zeta_i \nabla \zeta_j - \zeta_j \nabla \zeta_i), \qquad i, j = 1, \ldots, 4, \tag{11-55}$$

where $l_{ij} = l_k$ is the length of the edge between the vertices i and j forming the kth edge. It can be shown that $\nabla \cdot \mathbf{e}_k = 0$ and $\nabla \times \mathbf{e}_k = l_{ij}\, 2\nabla\zeta_i \times \nabla\zeta_j$.

11.2.3.2 Vector Basis Functions on Hexahedra

One can define the basis function for hexahedral elements in a slightly different manner, in the parametric (u, v, w) space. To do so, we start by introducing partial derivatives (a.k.a. parametric covariant vectors) $\mathbf{a}_\tau = \partial \mathbf{r}/\partial\tau$ where $\tau = (u, v, w)$. Next, we define a complementary set of vectors, namely the contravariant vectors as

$$\mathbf{a}^u = \frac{1}{V_+}\mathbf{a}_v \times \mathbf{a}_w, \quad \mathbf{a}^v = \frac{1}{V_+}\mathbf{a}_w \times \mathbf{a}_u, \quad \mathbf{a}^w = \frac{1}{V_+}\mathbf{a}_u \times \mathbf{a}_v, \tag{11-56}$$

Local Edge Number	First Node	Second Node
1	1	2
2	1	3
3	1	4
4	2	3
5	4	2
6	3	4

Table 11-1 Local Edge Numbering for a Tetrahedral Element

where $V_+ = \mathbf{a}_u \cdot (\mathbf{a}_v \times \mathbf{a}_w)$ is the differential volume used for normalization. Using these contravariant vectors, first-order vector finite-element functions can be written as

$$\begin{aligned}
\mathbf{e}_1 &= (v)(w)\mathbf{a}^u, & \mathbf{e}_2 &= (1-v)(w)\mathbf{a}^u \\
\mathbf{e}_3 &= (v)(1-w)\mathbf{a}^u, & \mathbf{e}_4 &= (1-v)(1-w)\mathbf{a}^u \\
\mathbf{e}_5 &= (u)(w)\mathbf{a}^v, & \mathbf{e}_6 &= (1-u)(w)\mathbf{a}^v \\
\mathbf{e}_7 &= (u)(1-w)\mathbf{a}^v, & \mathbf{e}_8 &= (1-u)(1-w)\mathbf{a}^v \\
\mathbf{e}_9 &= (u)(v)\mathbf{a}^w, & \mathbf{e}_{10} &= (1-u)(v)\mathbf{a}^w \\
\mathbf{e}_{11} &= (u)(1-v)\mathbf{a}^w, & \mathbf{e}_{12} &= (1-u)(1-v)\mathbf{a}^w.
\end{aligned} \tag{11-57}$$

Curls of the above functions can be easily evaluated using the standard formula

$$\begin{aligned}
\nabla \times \mathbf{e}_i = \frac{1}{\sqrt{g}} \Bigg\{ & \left[\frac{\partial(\mathbf{e}_i \cdot \mathbf{a}_w)}{\partial v} - \frac{\partial(\mathbf{e}_i \cdot \mathbf{a}_v)}{\partial w} \right] \mathbf{a}_u + \left[\frac{\partial(\mathbf{e}_i \cdot \mathbf{a}_u)}{\partial w} - \frac{\partial(\mathbf{e}_i \cdot \mathbf{a}_w)}{\partial v} \right] \mathbf{a}_v \\
& + \left[\frac{\partial(\mathbf{e}_i \cdot \mathbf{a}_v)}{\partial u} - \frac{\partial(\mathbf{e}_i \cdot \mathbf{a}_u)}{\partial v} \right] \mathbf{a}_w \Bigg\}
\end{aligned} \tag{11-58}$$

where g is the determinant of the metric tensor

$$g = \begin{vmatrix} (\mathbf{a}_u \cdot \mathbf{a}_u) & (\mathbf{a}_u \cdot \mathbf{a}_v) & (\mathbf{a}_u \cdot \mathbf{a}_w) \\ (\mathbf{a}_v \cdot \mathbf{a}_u) & (\mathbf{a}_v \cdot \mathbf{a}_v) & (\mathbf{a}_v \cdot \mathbf{a}_w) \\ (\mathbf{a}_w \cdot \mathbf{a}_u) & (\mathbf{a}_w \cdot \mathbf{a}_v) & (\mathbf{a}_w \cdot \mathbf{a}_w) \end{vmatrix}. \tag{11-59}$$

For a rectangular hexahedral element (a.k.a. the brick element), the above expressions can be simplified via $\mathbf{a}_u = \mathbf{a}^u = \mathbf{r}_2 - \mathbf{r}_1$, $\mathbf{a}_v = \mathbf{a}^v = \mathbf{r}_4 - \mathbf{r}_1$, and $\mathbf{a}_w = \mathbf{a}^w = \mathbf{r}_5 - \mathbf{r}_1$. In addition, the metric tensor determinant becomes $\sqrt{g} = V$ where V is the volume of the rectangular prism. Subsequently, the curls of the brick element basis functions also simplify as

$$\begin{aligned}
\nabla \times \mathbf{e}_1 &= \frac{1}{V}\{v\mathbf{a}_v - w\mathbf{a}_w\}, & \nabla \times \mathbf{e}_2 &= \frac{1}{V}\{(1-v)\mathbf{a}_v - w\mathbf{a}_w\}, \\
\nabla \times \mathbf{e}_3 &= \frac{1}{V}\{v\mathbf{a}_v - (1-w)\mathbf{a}_w\}, & \nabla \times \mathbf{e}_4 &= \frac{1}{V}\{(1-v)\mathbf{a}_v - (1-w)\mathbf{a}_w\}, \\
\nabla \times \mathbf{e}_5 &= \frac{1}{V}\{w\mathbf{a}_w - u\mathbf{a}_u\}, & \nabla \times \mathbf{e}_6 &= \frac{1}{V}\{w\mathbf{a}_w - (1-u)\mathbf{a}_u\}, \\
\nabla \times \mathbf{e}_7 &= \frac{1}{V}\{(1-w)\mathbf{a}_w - u\mathbf{a}_u\}, & \nabla \times \mathbf{e}_8 &= \frac{1}{V}\{(1-w)\mathbf{a}_w - (1-u)\mathbf{a}_u\}, \\
\nabla \times \mathbf{e}_9 &= \frac{1}{V}\{u\mathbf{a}_u - v\mathbf{a}_v\}, & \nabla \times \mathbf{e}_{10} &= \frac{1}{V}\{(1-u)\mathbf{a}_u - v\mathbf{a}_v\}, \\
\nabla \times \mathbf{e}_{11} &= \frac{1}{V}\{u\mathbf{a}_u - (1-v)\mathbf{a}_v\}, & \nabla \times \mathbf{e}_{12} &= \frac{1}{V}\{(1-u)\mathbf{a}_u - (1-v)\mathbf{a}_v\},
\end{aligned} \tag{11-60}$$

11.2.3.3 Vector Basis Functions on Triangular-Prism Elements

Since the triangular-prism element is a hybrid between triangular elements and quadrilateral elements, the basis functions for triangular-prism elements can be expressed as a combination of the barycentric and parametric representations. Namely, the vector functions associated with each of the 6 edges of the element are given as

$$\begin{aligned}
\mathbf{e}_1 &= (\zeta_2 \nabla\zeta_3 - \zeta_3 \nabla\zeta_2)(1-t),\\
\mathbf{e}_2 &= (\zeta_3 \nabla\zeta_1 - \zeta_1 \nabla\zeta_3)(1-t),\\
\mathbf{e}_3 &= (\zeta_1 \nabla\zeta_2 - \zeta_2 \nabla\zeta_1)(1-t),\\
\mathbf{e}_4 &= (\zeta_2 \nabla\zeta_3 - \zeta_3 \nabla\zeta_2)(t),\\
\mathbf{e}_5 &= (\zeta_3 \nabla\zeta_1 - \zeta_1 \nabla\zeta_3)(t),\\
\mathbf{e}_6 &= (\zeta_1 \nabla\zeta_2 - \zeta_2 \nabla\zeta_1)(t),\\
\mathbf{e}_7 &= (\zeta_1)\mathbf{a}^t,\\
\mathbf{e}_8 &= (\zeta_2)\mathbf{a}^t,\\
\mathbf{e}_9 &= (\zeta_3)\mathbf{a}^t,
\end{aligned} \tag{11-61}$$

where $\mathbf{a}^t$ is the vector defined by $\mathbf{r}(\zeta_1, \zeta_2, \zeta_3, t=1) - \mathbf{r}(\zeta_1, \zeta_2, \zeta_3, t=0)$.

We note here that the electric field boundary conditions require tangential continuity across material interfaces (where there are no magnetic currents). Hence, to carry on with the FEM implementation, the basis functions defined above need to be properly paired across neighboring finite elements such that tangential field continuity is explicitly enforced in the basis function expansion. That is, only a single "composite" basis function (hence a single unknown), spanning several elements that have the associated edge in common, is associated with each edge of the mesh. Indeed, the definitions above constitute only partial-basis functions. Basis functions associated with each edge of the mesh are constructed by pairing all such partial-basis functions that share the common edge. For instance, an internal edge in a tetrahedral mesh might be shared by 6 elements, in which case, the edge basis function would be the collection of all 6 partial-basis functions defined over the corresponding neighboring tetrahedra.

As we discuss in Sec. 11.2.4, the FEM discretization of the weak form in (11-48) relies on the computation of basis functions defined over each element using local coordinates and provides contributions of edge-based basis functions into the global FEM matrix.

11.2.4 Computation of FEM Matrices

We are now ready to discretize the weak form of the wave equation (11-48) numerically. To do so, we first insert the expansion (11-52) into (11-48), viz.

$$\int_v dv(\nabla\times\mathbf{W})\cdot\left(\nabla\times\sum_{i=1}^{N}x_i\mathbf{e}_i\right) - k_0^2\int_v dv\mathbf{W}\cdot\sum_{i-1}^{N}x_i\mathbf{e}_i - i\omega\mu\oint_{s=\partial v}ds\cdot\{\mathbf{W}\times\mathbf{H}\} = i\omega\mu\int_v dv\mathbf{W}\cdot\mathbf{J}^i. \tag{11-62}$$

In order to be able to construct a linear system for the N unknowns, we next choose N testing functions $\mathbf{w}_j$, $j = 1, \ldots, N$, giving

$$\sum_{i=1}^{N} x_i \int_v dv(\nabla \times \mathbf{w}_j) \cdot (\nabla \times \mathbf{e}_i) - k_0^2 \sum_{i=1}^{N} x_i \int_v dv \mathbf{w}_j \cdot \mathbf{e}_i - i\omega\mu \oint_{s=\partial v} d\mathbf{s} \cdot \{\mathbf{w}_j \times \mathbf{H}\}$$
$$= i\omega\mu \int_v dv \mathbf{w}_j \cdot \mathbf{J}^i, \qquad j = 1, \ldots, N \tag{11-63}$$

which can be written in a compact matrix form $[Z]\ \{x\} = \{f\}$. However, note that the surface integral contribution is written in terms of the surface magnetic field, which itself is an unknown. Thus the boundary magnetic field $\mathbf{H}$ must be dealt with before we can transform (11-63) into a matrix equation. Several efficient methods of mesh truncation are addressed next.

11.2.4.1 Truncation of the Solution Domain

11.2.4.1.1 Absorbing Boundary Conditions The simplest and one of the most popular methods for mesh truncation for wave equation is to simply impose the far-field behavior of fields as the boundary condition on the surface mesh bounding the FEM domain. As is well-known, fields radiating away from a source can be approximated as locally planar spherical waves in the far zone. That is, the following relation holds for the tangential components of electric and magnetic field intensities:

$$\hat{n} \times \mathbf{H}^{\text{scat}}(\mathbf{r}) = ik_0 \hat{n} \times \{\hat{n} \times \mathbf{E}^{\text{scat}}(\mathbf{r})\}. \tag{11-64}$$

The above condition approximately applies for the mesh truncation surface if it is sufficiently away from the sources and/or scattering centers within the FEM domain. However, since the total field within the domain just inside the truncation boundary consists of incident and scattered fields, (11-64) must be modified as

$$\hat{n} \times \mathbf{H}(\mathbf{r}) - ik_0 \hat{n} \times \{\hat{n} \times \mathbf{E}(\mathbf{r})\} = \hat{n} \times \mathbf{H}^{\text{inc}}(\mathbf{r}) - ik_0 \hat{n} \times \{\hat{n} \times \mathbf{E}^{\text{inc}}(\mathbf{r})\}. \tag{11-65}$$

Using (11-65), the unknown $\mathbf{H}$ under the surface integral in (11-50) can be written in terms of the electric field intensity $\mathbf{E}(\mathbf{r})$ as

$$\oint_{s=\partial v} ds \cdot \{\mathbf{W} \times \mathbf{H}\} = -\oint_{s=\partial v} ds \mathbf{W} \cdot \{\hat{n} \times \mathbf{H}\}$$
$$= -\oint_{s=\partial v} ds \mathbf{W} \cdot \{ik_0 \hat{n} \times (\hat{n} \times \mathbf{E}) + \hat{n} \times \mathbf{H}^{\text{inc}} - ik_0 \hat{n} \times (\hat{n} \times \mathbf{E}^{\text{inc}})\}. \tag{11-66}$$

Next, we transfer the first term involving the unknown $\mathbf{E}$ to the left-hand side of (11-48) and the terms involving the known incident field to the right-hand side. Doing so, (11-48) becomes

$$\int_v dv(\nabla \times \mathbf{W}) \cdot (\nabla \times \mathbf{E}) - k_0^2 \int_v dv \mathbf{W} \cdot \mathbf{E} + ik_0 \oint_s ds \mathbf{W} \cdot [\hat{n} \times (\hat{n} \times \mathbf{E})]$$
$$= i\omega\mu \int_v dv \mathbf{W} \cdot \mathbf{J}^i - \oint_s ds \mathbf{W} \cdot (\hat{n} \times \mathbf{H}^{\text{inc}}) + ik_0 \oint_s ds \mathbf{W} \cdot [\hat{n} \times (\hat{n} \times \mathbf{E}^{\text{inc}})]. \tag{11-67}$$

Alternatively, this can be cast in a more symmetric form as

$$\int_v dv(\nabla\times\mathbf{W})\cdot(\nabla\times\mathbf{E})+k_0^2\int_v dv\mathbf{W}\cdot\mathbf{E}-ik_0\oint_s ds(\hat{n}\times\mathbf{W})\cdot(\hat{n}\times\mathbf{E})$$
$$=i\omega\mu\int_v dv\mathbf{W}\cdot\mathbf{J}^i-\oint_s ds\mathbf{W}\cdot(\hat{n}\times\mathbf{H}^{\text{inc}})-ik_0\oint_s ds(\hat{n}\times\mathbf{W})\cdot(\hat{n}\times\mathbf{E}^{\text{inc}}). \quad (11\text{-}68)$$

In the above, the right-hand side is recognized the total excitation, consisting of an incident field excitation due to known sources external to the FEM domain as well as impressed currents within the FEM domain.

Discretization of the above equation as in (11-62) results in a sparse FE matrix. As mentioned earlier, as long as the truncation surface is sufficiently away (such that the electromagnetic fields locally behave as outward traveling plane waves), the absorbing boundary condition (ABC) approximation gives sufficiently accurate results. In discretized form, the FE-ABC equations are given as

$$\begin{bmatrix} E^{VV} & E^{SV} \\ E^{VS} & E^{SS} \end{bmatrix}\begin{bmatrix} a_V \\ a_S \end{bmatrix}=\begin{bmatrix} f^I \\ f^S \end{bmatrix}, \quad (11\text{-}69)$$

where

$$E^{VV}=\int_v dv(\nabla\times\mathbf{e}_j)\cdot(\nabla\times\mathbf{e}_i)-k_0^2\int_v dv\mathbf{e}_j\cdot\mathbf{e}_i \quad (11\text{-}70)$$

for all finite-element edges inside the solution domain v, and

$$E^{SV}=[E^{VS}]^T=\int_v dv(\nabla\times\mathbf{e}_j)\cdot(\nabla\times\mathbf{e}_i)-k_0^2\int_v dv\mathbf{e}_j\cdot\mathbf{e}_i \quad (11\text{-}71)$$

for all basis functions $\mathbf{e}_i$ in the volume v and testing functions $\mathbf{e}_j$ associated with the edges on the boundary surface s. More importantly, the surface unknown contributions in (11-69) are given as

$$E^{SS}=\int_v dv(\nabla\times\mathbf{e}_j)\cdot(\nabla\times\mathbf{e}_i)-k_0^2\int_v dv\mathbf{e}_j\cdot\mathbf{e}_i-ik_0\int_s ds(\hat{n}\times\mathbf{e}_j)\cdot(\hat{n}\times\mathbf{e}_i). \quad (11\text{-}72)$$

In addition, all excitations inside the FEM volume v contribute to the first part of the right-hand side and are computed using

$$f^I=i\omega\mu\int_v dv\mathbf{W}\cdot\mathbf{J}^i. \quad (11\text{-}73)$$

Moreover, the surface portion of the excitation vector $[f^I f^S]^T$ in (11-69) may also contain external incident field contributions in the form

$$f^S=-\int_v ds\mathbf{e}_j\cdot(\hat{n}\times\mathbf{H}^{\text{inc}})-ik_0\int_s ds(\hat{n}\times\mathbf{e}_i)\cdot(\hat{n}\times\mathbf{E}^{\text{inc}})+f^S_{\text{internal}}, \quad (11\text{-}74)$$

in which any internal sources on the truncation boundary also contribute to the right-hand side, viz.

$$f^S_{\text{internal}}=i\omega\mu\int_v dv\mathbf{W}\cdot\mathbf{J}^{i,s}. \quad (11\text{-}75)$$

Excitations interior to the solution domain are typically used to model port excitations in antenna design. These include infinitesimal voltage and current sources, as well as waveguide feed ports. We will summarize such excitations in Section 11.2.5.

All integrations involved in (11-70)–(11-75) can be evaluated numerically using a suitable quadrature. However, in most cases closed form expressions using the definitions of the basis functions can also be obtained.

Turning our attention back to mesh truncations schemes, we note that the approximate ABC in (11-65) is sometimes referred to as the zeroth order ABC (or the radiation boundary condition) since it involves only the far-field behavior of the electromagnetic energy. Several higher-order ABCs have also been developed for improved accuracy (see e.g., [36], [37], [15], [23], [10]). Such higher-order ABCs allow one to bring the FEM truncation surface closer to the antenna structure, thereby keeping the FEM domain and the resulting FEM matrix equation small, leading to faster and more efficient solutions. Another alternative to keep the FEM mesh close to the antenna structure is to use perfectly matched layers, which are discussed below.

11.2.4.1.2 Artificial Absorbers and Perfectly Matched Layers Much like the ABCs, artificial absorbers are simply *artificial* material layers that are placed on the truncation surface inside the FEM mesh. When the surface integral in (11-50) over the truncations surface s is simply discarded, the boundary surface ends up behaving like a conducting surface (the surface integral equals zero when $\mathbf{E}_{\tan} = 0$). Artificial absorbers are placed over this PEC boundary to eliminate reflections back into the solution domain. As such, multiple layers to artificial lossy materials with equal relative permittivity and permeabilities $\epsilon_i = \mu_i$ (for wave impedance matching) are placed on the inside of the truncation surface. The thicknesses and the material parameters are arranged such that the reflection from the truncation surface is minimized over a broad frequency and incidence angle range. The process of designing such artificial absorbers often requires a multidimensional optimization and results in nonphysical material parameters for the layers [23], [10]. A particular set of artificial absorbers, perfectly matched layers, is rather popular in FEM modeling (as well as in time-domain FEM and finite-difference implementations).

Perfectly matched layers [15] are artificial, anisotropic lossy material layers that do not reflect waves impinging from a lossless medium. Formal derivation of various PMLs is lengthy and beyond the scope of this introductory chapter and can be found in most prominent finite-element books such as [23], [10]. With the predetermined PML material parameters, the FE equation (using anisotropic material formulation)

$$\int_v dv(\nabla \times \mathbf{W}) \cdot \bar{\bar{\mu}}^{-1} \cdot (\nabla \times \mathbf{E}) - \omega^2 \int_v dv \mathbf{W} \cdot \bar{\bar{\epsilon}} \cdot \mathbf{E} = i\omega \int_v dv \mathbf{W} \cdot \mathbf{J}^i \tag{11-76}$$

can be solved straightforwardly without the need to deal with the surface fields on s.

Several combinations of ABCs and PMLs have also been considered. In particular, ABC backed PMLs provide better absorption of outgoing energy. Also, averaging two solutions to the same problem, one with with PMC backed PML and the other with the conventional PEC backed PML, can provide much better accuracy.

11.2.4.1.3 Exact Mesh Termination Through Boundary Integral Equations In addition to the mesh truncations summarized above, an exact relation between the tangential

electric and magnetic fields on the truncations surface can be used. These are given in terms of the Stratton-Chu integral representation formulas [38]. Namely, the electric field integral equation (EFIE) is given by

$$\frac{1}{2}\hat{n}\times(\hat{n}\times\mathbf{E})+\hat{n}\times[\hat{n}\times\mathcal{L}(\hat{n}\times\mathbf{H})]+\hat{n}\times[\hat{n}\times\mathcal{K}(\hat{n}\times\mathbf{E})]=\hat{n}\times(\hat{n}\times\mathbf{E}^{\text{inc}}), \tag{11-77}$$

and the magnetic field integral equation (MFIE) is given by

$$\frac{1}{2}\hat{n}\times\mathbf{H}+\hat{n}\times\mathcal{K}(\hat{n}\times\mathbf{H})-\hat{n}\times\mathcal{L}(\hat{n}\times\mathbf{E})=\hat{n}\times\mathbf{H}^{\text{inc}}, \tag{11-78}$$

where the operators $\mathcal{L}$ and $\mathcal{K}$ are defined as

$$\mathcal{L}(\mathbf{X})=-ik_0\int_s ds\left[\mathbf{X}+\frac{1}{k_0^2}\nabla\nabla'\cdot\mathbf{X}\right]\frac{e^{ik_0R}}{4\pi R} \tag{11-79}$$

and

$$\mathcal{K}(\mathbf{X})=\int_s ds\mathbf{X}\times\nabla\frac{e^{ik_0R}}{4\pi R}, \tag{11-80}$$

in which $R=|\mathbf{r}-\mathbf{r}'|$ is the distance between the source and observation points. Both (11-77) and (11-78) are exact relations between the tangential field components; however, while the ABC relation $\hat{n}\times\mathbf{H}=ik_0\hat{n}\times(\hat{n}\times\mathbf{E})$ was used to eliminate $\hat{n}\times\mathbf{H}$ in (11-48) before, in this case the unknown $\hat{n}\times\mathbf{H}$ appears under integral operators. Thus, a simple elimination is not possible. Nonetheless, we can treat $\hat{n}\times\mathbf{H}$ as an unknown as it is and use the EFIE or the MFIE as an additional equation to complement the original FEM system. However, we must note that care must be taken in doing so since both (11-77) and (11-78) are themselves prone to so-called *interior resonance* problems. To eliminate this problem, a weighted sum of EFIE and MFIE, called the combined field integral equation, is used. The resulting FE-BI system is compactly given as

$$\begin{bmatrix} E^{VV} & E^{SV} & 0 \\ E^{VS} & E^{SS} & B \\ 0 & \tilde{B} & Z \end{bmatrix}\begin{bmatrix} E_V \\ E_S \\ H_S \end{bmatrix}=\begin{bmatrix} J^I \\ J^S \\ b \end{bmatrix}. \tag{11-81}$$

In the above, the submatrices E^{VV}, E^{SV}, and E^{VS} are identical to those given in (11-70) and (11-71). However, the submatrix E^{SS} in (11-81) is slightly modified in that the surface integral in (11-72) is treated separately as a submatrix B, viz.

$$\begin{aligned} E^{SS}&=\int_v dv(\nabla\times\mathbf{e}_j)\cdot(\nabla\times\mathbf{e}_i)-k_0^2\int_v dv\,\mathbf{e}_j\cdot\mathbf{e}_i \\ B&=-ik_0\int_S ds(\hat{n}\times\mathbf{e}_i)\cdot(\hat{n}\times\mathbf{e}_j). \end{aligned} \tag{11-82}$$

In addition, the boundary integral equation submatrices $\tilde{B}$ and Z are given in terms of the EFIE and MFIE contributions as $\tilde{B} = \alpha\tilde{B}_{\text{EFIE}} + (1 - \alpha)\,\tilde{B}_{\text{MFIE}}$ and $Z = \alpha Z_{\text{EFIE}} + (1 - \alpha)\,Z_{\text{MFIE}}$, where α is a constant between 0 and 1, typically chosen as 0.5 and

$$\begin{aligned}
\tilde{B}_{\text{EFIE}} &= \int_S ds(\hat{n}\times\mathbf{t}_j)\cdot\hat{n}\times\left[\frac{1}{2}(\hat{n}\times\mathbf{e}_i) + \hat{n}\times\mathcal{K}(\hat{n}\times\mathbf{e}_i)\right] \\
\tilde{B}_{\text{MFIE}} &= -\int_S ds(\hat{n}\times\mathbf{t}_j)\cdot[\hat{n}\times\mathcal{L}(\hat{n}\times\mathbf{e}_i)] \\
Z_{\text{EFIE}} &= \int_S ds(\hat{n}\times\mathbf{t}_j)\cdot\hat{n}\times[\hat{n}\times\mathcal{L}(\hat{n}\times\mathbf{h}_i)] \\
Z_{\text{MFIE}} &= \int_S ds(\hat{n}\times\mathbf{t}_j)\cdot\left[\frac{1}{2}(\hat{n}\times\mathbf{h}_i) + \hat{n}\times\mathcal{K}(\hat{n}\times\mathbf{h}_i)\right].
\end{aligned} \tag{11-83}$$

Here, we also introduced the testing functions $\mathbf{t}_j$ defined over the surface elements on s. Moreover, for the CFIE implementation, the excitations submatrix b associated with external excitations is also given as

$$b = \alpha\int_S ds(\hat{n}\times\mathbf{t}_j)\cdot\hat{n}\times(\hat{n}\times\mathbf{E}^{\text{inc}}) + (1-\alpha)\int_S ds(\hat{n}\times\mathbf{t}_j)\cdot\hat{n}\times\mathbf{H}^{\text{inc}} \tag{11-84}$$

Although the previous equations seem complicated, they can be greatly simplified when the surface basis/testing functions for the tangential electric and magnetic field are chosen to be the same such that $\mathbf{e}_j = \mathbf{h}_j$. Also, $\mathbf{t}_j$ is chosen as $\mathbf{t}_j = \hat{n}\times\mathbf{h}_j$ on the surfaces of volumetric elements that lie on the boundary S. We also note that several variants of the FE-BI system have also been reported [39]–[42].

In numerically solving real-life problems, one would like to be assured that the obtained FEM solution is accurate. In essence, if a solution is obtained using an FEM mesh with an average edge length of h, it is important to put an upper bound on the error in the FEM solution in terms of the mesh parameter h. That is, we expect that FEM solution accuracy should improve when a denser mesh is used for the same problem. To measure a rate of convergence, the mesh parameter h is used. Another alternative is to improve the modeling abilities of the basis functions using higher-order expansions [43]–[47]. If we denote the FE expansion order with p, we must be assured that by increasing p the FEM error can be improved. Obviously, a denser mesh or a higher-order expansion is most beneficial in the regions where the field behavior changes rapidly due to sharp geometrical changes, such as edges and corners, or due to excitations points, such as feeds and waveguide ports. Thus, often both strategies are combined and mesh density and basis function order are adaptively increased over regions with rapid spatial field variations [48].

11.2.5 Feed Modeling

For an accurate antenna analysis, it is important that the antenna feeds within the FEM domain are accurately representable in the FEM statement. In addition to material modeling capabilities, the FEM also incorporates various feeding mechanisms used in modern antenna designs. Some of the most frequently used feed models are summarized in the following subsections.

11.2.5.1 Current Probe Feeds

Coaxial transmission lines are widely used in printed antennas, such as microstrip patch antennas. Typically, the center conductor of the coaxial feed is attached to the patch and the outer conductor to the ground plane. The short section of the center conductor behaves as a current probe that excites the patch antenna. Such feeds can readily be modeled with FEM when this short section is treated as an impressed current source under the patch. As such, the coaxial transmission line is replaced by a current probe feed and the excitation of this current probe is computed by

$$f^I = ik_0 Z_0 \int_{V_s} dv \mathbf{W} \cdot \mathbf{J}^i \tag{11-85}$$

where the impressed current source is due to a current element along the direction of the original coaxial probe as

$$\mathbf{J} = \hat{l} I \delta(\mathbf{r}_s). \tag{11-86}$$

The input impedance of the feeding port can be subsequently found by considering the electric field unknown (after solving the FEM system) at the probe feed location using the well-known formula $Z_{\text{in}} = V/I$, where

$$V = -\int_l dl \mathbf{E} \cdot \hat{l} \tag{11-87}$$

in which l is the length of the probe section.

Alternatively, for modeling antennas fed by other types of transmission lines, such as dipole antennas, a voltage gap model may be more appropriate.

11.2.5.2 Voltage Gap Feeds

If we assume a voltage differential exists across the pth edge of the FEM mesh, such that the electric field across the edge is forced to assume a constant value, we can eliminate the unknown associated with that edge through $E_s = V/d$, where d is the length of the edge. With this assignment, the column in the FEM matrix associated with the voltage gap edge can be explicitly evaluated and thus is eliminated from the system, decreasing the matrix size by 1 for each voltage gap source. Consequently, the pth column becomes an excitation to the reduced system as

$$b_j = \frac{V}{d} \int_v dv (\nabla \times \mathbf{w}_j) \cdot (\nabla \times \mathbf{e}_p) + \frac{k_0^2 V}{d} \int_v dv \mathbf{w}_j \cdot \mathbf{e}_p. \tag{11-88}$$

After the solution of the reduced system, the input impedance of the voltage gap excitation port can be found from $Z_{\text{in}} = V/I$, where the current I flowing across the voltage gap feed can be found by

$$I = \frac{I}{i\omega\mu} \oint_c dl (\nabla \times \mathbf{E}) \cdot \hat{c}. \tag{11-89}$$

11.2.5.3 Lumped Circuit Elements

Lumped elements can also be easily implemented by assigning lossy/reactive material parameters to the finite elements associated with the circuit components. For example, a lumped load of impedance Z_L associated with the kth edge of the mesh contributes to the FEM via

$$E^{VV} = \frac{-ik_0 Z_0 l^2}{Z_L} \tag{11-90}$$

As such, modeling of shorting pins is extremely easy in the sense that for each shorting pin edge, simply the associated edge unknown is set to zero, eliminating the associated column from the FEM matrix.

11.2.5.4 Waveguide Port Feeds

For modeling antennas that are fed via waveguides, a modal expansion must be incorporated into the FEM system. This is needed to express the surface **H** field over the waveguide port in terms of the unknown **E** field (so that the surface term in (11-48) can be eliminated). For this, a general modal summation expression for the waveguide fields, given as

$$\mathbf{H} = \mathbf{H}^{\text{inc}} + \sum_m a_m \mathbf{h}_m e^{\gamma m z}, \quad \mathbf{E} = \mathbf{E}^{\text{inc}} + \sum_m \frac{a_m}{Z_m} \mathbf{e}_m e^{\gamma m z} \tag{11-91}$$

where

$$a_m = e^{-\gamma m L} \int_S ds \mathbf{h}_m \cdot [\mathbf{H} - \mathbf{H}^{\text{inc}}]_{z=L} \tag{11-92}$$

is used. Obviously, various orthonormality relationships between waveguide modes can be applied to simplify the above equation [23], [10], [38].

Although we stated the eigenmode expansion using infinitely many modes, the summations in (11-92) are truncated in FEM implementations. If the waveguide port surface inside the waveguide is chosen far enough from the waveguide-antenna junction, only a few terms in (11-92) is sufficient since most higher-order modes are evanescent and will die out before reaching the wave-port surface. Moreover, the wave-port can be chosen sufficiently far from the junction such that considering only the dominant mode would result in accurate FEM solutions. Since waveguides are typically small in size, the additional burden to model the extra waveguide section in the FEM domain is often very small.

In addition to the feed models summarized above, known incident fields from sources external to the solution domain can also be included as excitations using (11-74) and (11-84) for the FE-ABC and FE-BI implementations, respectively. Moreover, FEM problems involving thin lossy material layers and/or conductors coated with thin layers can be further simplified by replacing such thin layers by equivalent impedance boundary conditions. Resistive sheets, thin dielectric layers, etc. can be readily approximated via impedance boundary conditions [49]. In addition, even nonlinear circuit elements such as diodes and transistors can be implemented into the FEM framework coupled with circuit simulation approaches.

11.2.6 Calculation of Radiation Properties of Antennas

As noted in the previous subsection, antenna impedances associated with the small port excitations or waveguide feeds can be readily calculated after the FEM solution. Likewise, the near-zone fields around the antennas are available as an immediate result of the FEM solution. However, far-zone antenna parameters, such as the radiations patterns, need to be separately computed following the FEM solution. Fortunately, this can be accomplished by simply employing the Stratton-Chu integral representations given in (11-79) and (11-80) for observation points in the farzone. Thus, for FEM-ABC and FE-BI solutions, the following simple formulas are employed to compute the far-field radiation patterns of the antennas using the tangential field values on the truncation boundary, $\mathbf{E}^{ff} = \mathcal{L}^{ff}(\hat{n} \times \mathbf{H}) + \mathcal{K}^{ff}(\hat{n} \times \mathbf{E})$, where

$$\mathcal{L}^{ff}(\hat{n} \times \mathbf{H}) = \int_s ds \left[\overline{\overline{I}} - \hat{k}\hat{k}\right] \cdot (\hat{n} \times \mathbf{H}) e^{i\mathbf{k}\cdot\mathbf{r}} \tag{11-93}$$

and

$$\mathcal{K}^{ff}(\hat{n} \times \mathbf{K}) = \int_s ds \hat{k} \times [\hat{n} \times (\hat{n} \times \mathbf{E})] e^{i\mathbf{k}\cdot\mathbf{r}} \tag{11-94}$$

In case of FEM-PML solution, an auxiliary surface inside the FEM volume, sufficiently far away from the PML region as well as the antenna geometry, must be used to compute the tangential field quantities used in (11-93) and (11-94).

11.2.7 An FEM Example: Broadband Vivaldi Antenna

In this subsection, we demonstrate the FEM solution of a typical wideband antenna. The antenna of choice is a popular wideband Vivaldi, as shown in Fig. 11-19 [50]. As seen, the antenna consists of two tapered slots etched on both sides of a conductor backed dielectric substrate. The permittivity of the substrate used here is $\epsilon_r = 2.2$ and a stripline feed with a wideband open end is integrated into the antenna substrate. This feed is excited by two current probes at the end of the line between the two conductor planes. Alternatively, a coaxial waveguide feed can also be used to excite the stripline.

The Vivaldi antenna has been a popular element for phased arrays. Although the presented FEM is also applicable to antenna array modeling, standard approach often leads to very large FEM systems that are computationally intensive to solve. Several highly efficient methods based on decomposing the original problem into many identical subdomains (these subdomains obviously correspond to the individual antenna elements in a large phased array) have been developed. These domain decomposition methods are discussed in [51]–[54].

The first step in modeling the Vivaldi antenna is to represent its geometry on the computer and generate an FEM mesh. A typical mesh using hexahedral elements is shown in Fig. 11-12c. In order to proceed with the problem setup, first, all FEM unknowns associated with the conducting surface in the geometry are eliminated since the total tangential electric field on PEC surfaces is zero. For this particular example, the total number of non-PEC edges in the mesh is 2, 236. Next, all finite elements are assigned a relative permittivity of $\epsilon_r = 2.2$ and the FEM matrix is calculated using (11-81). The two current probe sources contribute to the right-hand side of (11-81) through (11-85). We note that the FEM matrix and the excitation

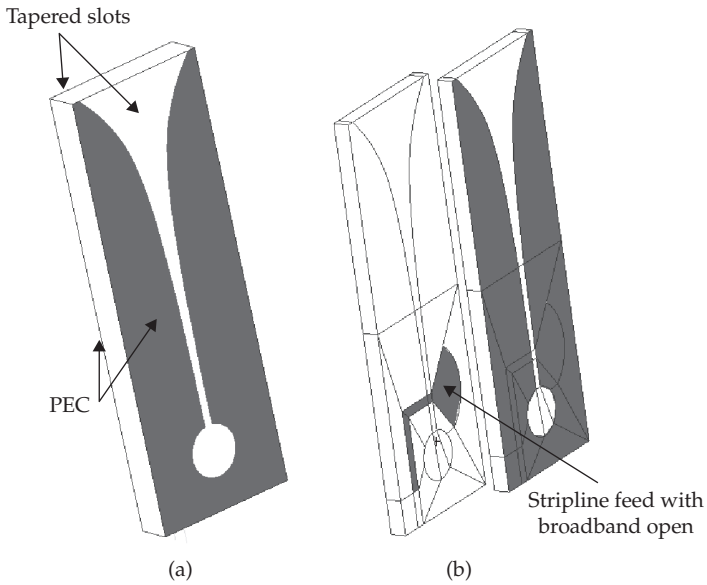

Figure 11-19 A representative antenna problem: (a) Vivaldi tapered slot antenna geometry and (b) the stripline feeding the two tapered slots (Geometry is split in half for illustration of feeding detail).

vector must be computed for each frequency in order to generate the input impedance behavior of the antenna over a desired range of frequencies. To accelerate this process, fast frequency sweep methods based on the asymptotic waveform evaluation (AWE) expansion [10], domain decomposition based preconditioners (see Section 11.3), as well as model order reduction techniques [26] are used.

Next, we first consider an FE-BI solution of the Vivaldi antenna problem. Since, as described in Section 11.2.4, the BI treatment is an exact mesh truncation scheme, only the antenna structure is meshed as shown in Fig. 11-12c. This discretization results in 986 volume unknowns and 1250 surface unknowns. However, we note that due to the moment method nature of the BI portion, the submatrices $\tilde{B}$ and Z in (11-81) are fully populated, thus, the computational cost of FE-BI can be substantial. For larger size problems, one often resorts to fast integral equation solution methods, such as the fast multipole method or the adaptive integral method [55], [56].

After the matrix is computed, the contributions of the two current probe feeds that excite the stripline feeding the antenna are modeled using (11-85). The input impedance for the feed is computed as a parallel combination of the two current probes, each of which has an impedance according to (11-87).

Alternatively, we can also solve the same problem using FE-ABC, as described in Section 11.2.4. In this case, we need to mesh a substantial amount of space around the antenna so that we can use the ABC approximation of (11-64). For the FE-ABC, the total number of unknowns increase to 48,123. However, since the matrix system is extremely sparse, the computational cost of solving this larger system is still comparable with the FE-BI system.

The resulting systems can be solved using a direct solver when the system size is relatively small since the computational complexity of direct solution scales as $O(N^3)$, where N is the overall matrix size. However, since most antenna simulations are done in the transmitting mode (with a fixed internal excitation), often only a single solution is sufficient for each frequency. Thus, relatively cheaper iterative solution techniques are often used in practice. Particularly, for larger problems, the computational savings of efficient iterative solvers and preconditioners (such as a simple diagonal preconditioner) make them the preferred choice.

After the matrix solution is obtained one can visualize the actual electromagnetic fields in and around the antenna structure. In Fig. 11-20, we plot the electric field on the surface of the Vivaldi antenna at 5 GHz. The coupling of the incident power from the stripline onto the tapered slot is clearly visible. The FE-ABC solution also provides the field behavior around the antenna, as well as inside. As seen in Fig. 11-21, the antenna radiates through the opening of the tapered slot.

In Fig. 11-22 we plot the input impedance of the Vivaldi antenna obtained by FE-BI and FE-ABC solutions. As seen, both are in good agreement with each other and predict that the antenna is designed to operate approximately between 1–5 GHz. We note, however, that this particular antenna design is intended to be used in a phased array configuration, such as the one shown in Fig. 11-23. In this case, the antenna behavior will be affected due to mutual coupling between adjacent elements. In Section 11.3, we address FEM techniques that are particularly well suited for antenna array analysis.

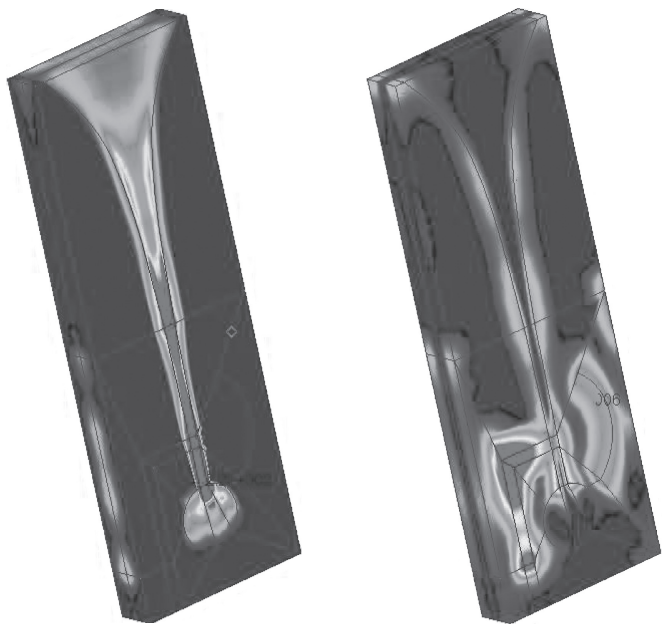

(a) (b)

Figure 11-20 Grayscale rendering of electric field magnitude inside the Vivaldi antenna at 5 GHz. (a) $\mathbf{E}_x$ showing the fields within the slot are mostly x-polarized, (b) $\mathbf{E}_y$ showing that the fields within the stripline are mostly y-polarized.

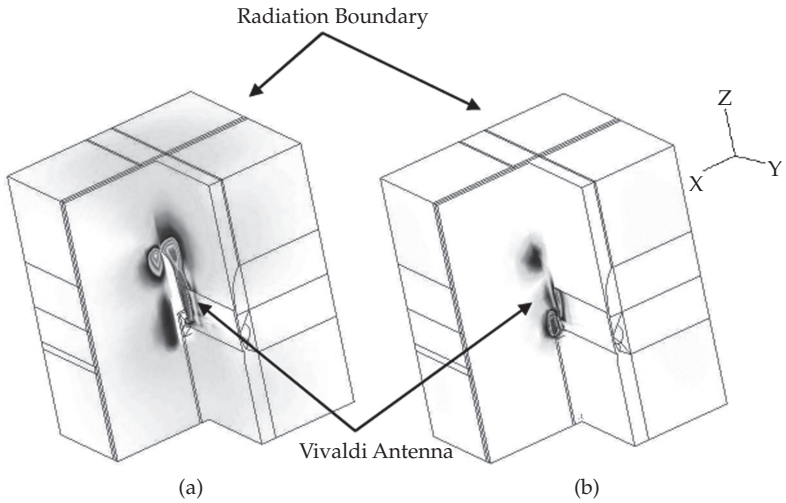

Figure 11-21 Volumetric field behavior in and around the Vivaldi antenna after FE-ABC solution (part of the FEM mesh is deleted to show the interior structure): (a) $\mathbf{E}_x$ (b) $\mathbf{E}_y$

Such fast alternatives for array design by fully harnessing the modeling capabilities of FEM has been instrumental in developing new designs using full material and geometrical flexibility.

Finally, it is straightforward to compute the far zone radiation pattern of the Vivaldi using (11-93) and (11-94). Often depicted as a polar plot, the two principle cut radiation patters of the Vivaldi as shown in Fig. 11-24. In addition, Fig. 11-24b shows the three-dimensional pattern of the antenna at 5 GHz. By integrating this pattern, standard antenna parameters, such as the directivity D_0 and the total radiated power P_{rad} can be readily obtained. Additionally, any impedance mismatches can also be included in this

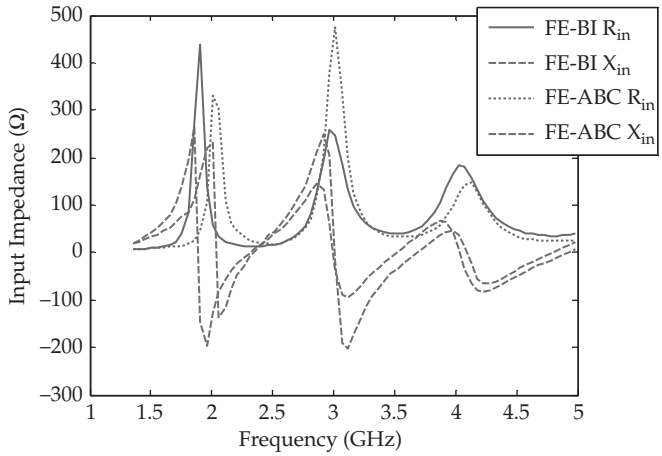

Figure 11-22 Input impedance of the Vivaldi antenna using the FE-BI and FE-ABC formulations

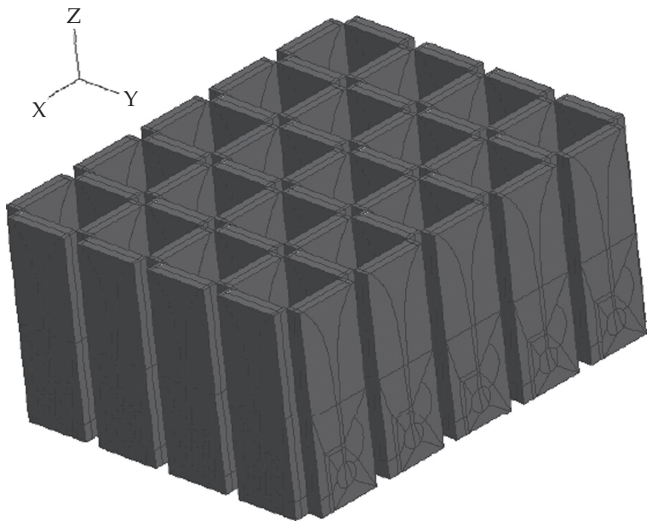

Figure 11-23 A 49-element dual polarization Vivaldi array

calculation to compute the overall antenna gains. In antenna design problems, the FEM systems needs to be solved for each frequency. For broadband antennas, this might be a time-consuming task. Instead, fast frequency sweep algorithms based on the asymptotic waveform evaluation (see [10] and references therein) can significantly speed up the broadband simulations. Moreover, large phased antenna arrays made of many identical antenna elements can be efficiently solved by exploiting the symmetries in the geometry. Several domain decomposition algorithms have been developed [57], [51], [53] to efficiently tackle large FEM problems with geometrical repetitions. In the next section, we outline the domain decomposition method in the FEM context.

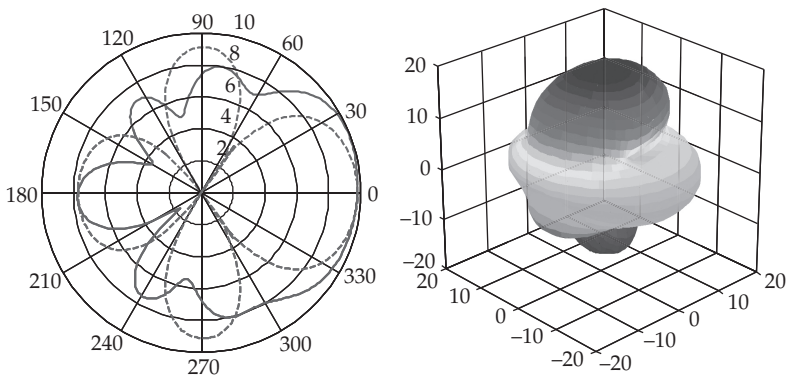

(a) Far-Field Pattern (b) 3D Rendering

Figure 11-24 (a) Far-field patterns of the Vivaldi antenna at 5 GHz on the two principle cuts. (b) 3D rendering of the antenna patterns at 5 GHz.

11.3 Conformal Domain Decomposition Method

In this section, we adopt the engineering notation, and employ $j = \sqrt{-1}$.

11.3.1 Notation

We first introduce some notation and definitions that will be employed throughout the manuscript. Boldface letters (e.g., $\mathbf{u}$) are used to denote vectors in $\mathbb{R}^3$ while an overhead hat (e.g., $\hat{\mathbf{u}}$) will signify that the vector has unit magnitude. Finite dimensional matrices will be represented by uppercase italic characters (e.g., A), while lowercase italic characters will be used to represent column vectors (e.g., x). The imaginary unit will be represented by j.

We will denote the time-harmonic electric and magnetic fields by $\mathbf{E}$ and $\mathbf{H}$, respectively [58]. The free-space wavenumber will be denoted by $k_0 = \omega\sqrt{\mu_0\varepsilon_0}$, where $\omega = 2\pi f$ is the radial frequency of operation and ε_0 and μ_0 are the permittivity and permeability in free space, respectively. The free-space intrinsic impedance is given by $\eta_0 = \sqrt{\mu_0/\varepsilon_0}$. In a material region, the wavenumber is given by $k = \omega\sqrt{\mu\varepsilon}$, where ε and μ are the permittivity and permeability of the material. Also, we define $\varepsilon_r = \varepsilon/\varepsilon_0$ and $\mu_r = \mu/\mu_0$ as the relative permittivity and permeability of the material.

In deriving the methods we will often consider a domain $\Omega \subset \mathbb{R}^3$ and its decomposition into $N_p = 2$ subdomains such that $\Omega = \Omega_1 \cup \Omega_2$ (see Fig. 11-25). Further, we define the interface between subdomains as $\Gamma := \partial\Omega_1 \cap \partial\Omega_2$, and the exterior boundaries as $\widetilde{\partial\Omega_i} := \partial\Omega_i \cap \partial\Omega$. We denote the outward-directed unit normal to $\partial\Omega_i$ by $\hat{\mathbf{n}}_i$. The subscripts $i \in \{1, 2\}$ will denote the restriction of a quantity to $\overline{\Omega_i}$. For example, in $\overline{\Omega_i}$, $\mathbf{E}_i$ will denote the electric field while ε_{ri} and μ_{ri} will denote the relative permittivity and permeability, respectively.

We will also use the tangential trace operator

$$\gamma_\tau(\mathbf{u}_i) := \hat{\mathbf{n}}_i \times \mathbf{u}_i \mid \partial\Omega_i \tag{11-95}$$

and tangential components trace operator

$$\pi_\tau(\mathbf{u}_i) := \hat{\mathbf{n}}_i \times (\mathbf{u}_i \times \hat{\mathbf{n}}_i) \mid \partial\Omega_i \tag{11-96}$$

along with the associated jump and average operators on the interface Γ:

$$[\![\mathbf{u}]\!]_\gamma := \gamma_\tau(\mathbf{u}_1) + \gamma_\tau(\mathbf{u}_2) \tag{11-97}$$

$$[\![\mathbf{u}]\!]_\pi := \pi_\tau(\mathbf{u}_1) - \pi_\tau(\mathbf{u}_2) \tag{11-98}$$

$$\{\!\{\mathbf{u}\}\!\}_\gamma := \frac{1}{2}(\gamma_\tau(\mathbf{u}_1) - \gamma_\tau(\mathbf{u}_2)). \tag{11-99}$$

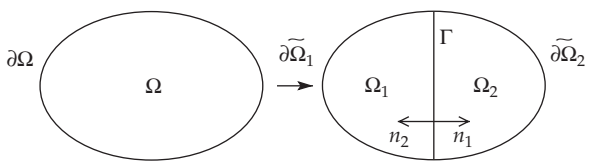

Figure 11-25 Notation for decomposition of the domain

Volume and surface sesquilinear forms are defined by

$$(\mathbf{u},\mathbf{v})_{\Omega} := \int_{\Omega} \bar{\mathbf{u}} \cdot \mathbf{v}\, dv \tag{11-100}$$

and

$$\langle \mathbf{u},\mathbf{v}\rangle_{\partial\Omega} := \int_{\partial\Omega} \bar{\mathbf{u}} \cdot \mathbf{v}\, ds, \tag{11-101}$$

where the overbar denotes conjugation. Note that we sometimes use $(\mathbf{u}, \mathbf{v})_{\Omega}$ to mean the broken form $(\mathbf{u}_1, \mathbf{v}_1)_{\Omega 1} + (\mathbf{u}_2, \mathbf{v}_2)_{\Omega 2}$ and, similarly, $\langle \mathbf{u}, \mathbf{v}\rangle_{\partial\Omega} = \langle \mathbf{u}_1, \mathbf{v}_1\rangle_{\widetilde{\partial\Omega}_1} + \langle \mathbf{u}_2, \mathbf{v}_2\rangle_{\widetilde{\partial\Omega}_2}$.

We recall the standard Sobolev spaces $H^s(\Omega)$ for $s \in \mathbb{R}$ and $H^t(\partial\Omega)$ for $t \in [-1, 1]$ [59], and set

$$\mathbf{H}^s(\Omega) := (H^s(\Omega))^3 \tag{11-102}$$

$$\mathbf{H}^t(\partial\Omega) := (H^t(\partial\Omega))^3 \tag{11-103}$$

$$L^2(\Omega) := H^0(\Omega) \tag{11-104}$$

$$\mathbf{L}^2(\Omega) := \mathbf{H}^0(\Omega). \tag{11-105}$$

Also, we define [60]

$$\mathbf{H}(\mathrm{curl},\Omega) := \{\mathbf{u} \in \mathbf{L}^2(\Omega) \mid \nabla \times \mathbf{u} \in \mathbf{L}^2(\Omega)\} \tag{11-106}$$

$$\mathbf{H}(\mathrm{div},\Omega) := \{\mathbf{u} \in \mathbf{L}^2(\Omega) \mid \nabla \cdot \mathbf{u} \in L^2(\Omega)\} \tag{11-107}$$

$$\mathbf{H}^{-1/2}(\mathrm{curl}_{\tau},\partial\Omega) := \{\mathbf{u} \in \mathbf{H}^{-1/2}(\partial\Omega) \mid \nabla_{\tau} \times \mathbf{u} \in \mathbf{H}^{-1/2}(\partial\Omega), \hat{\mathbf{n}} \cdot \mathbf{u} = 0\} \tag{11-108}$$

$$\mathbf{H}^{-1/2}(\mathrm{div}_{\tau},\partial\Omega) := \{\mathbf{u} \in \mathbf{H}^{-1/2}(\partial\Omega) \mid \nabla_{\tau} \cdot \mathbf{u} \in \mathbf{H}^{-1/2}(\partial\Omega), \hat{\mathbf{n}} \cdot \mathbf{u} = 0\} \tag{11-109}$$

$$\mathbf{H}_0(\mathrm{curl},\Omega) := \{\mathbf{u} \in \mathbf{H}(\mathrm{curl},\Omega) \mid \gamma_{\tau}(\mathbf{u}) = 0 \text{ on } \Gamma_D\}. \tag{11-110}$$

Note that $\mathbf{H}_0(\mathrm{curl}, \Omega)$ is the space of curl-conforming functions that satisfy essential boundary conditions on Γ_D, the collection of surfaces on which Dirichlet boundary conditions are applied. This is the space in which the electric field resides, with the appropriate Dirichlet conditions imposed on Perfect Electrically Conducting (PEC) surfaces. That is, we may write $\mathbf{E}_i \in \mathbf{H}_0(\mathrm{curl}, \Omega_i)$. Similarly, the subscript 0 will be used with other function spaces to denote that essential Dirichlet boundary conditions are enforced.

Finally, we recall that the function spaces for the traces of curl-conforming functions are given via [60]

$$\mathbf{H}^{-1/2}(\mathrm{curl}_{\tau},\partial\Omega) := \{\pi_{\tau}(\mathbf{u}) \mid \mathbf{u} \in \mathbf{H}(\mathrm{curl},\Omega)\} \tag{11-111}$$

$$\mathbf{H}^{-1/2}(\mathrm{div}_{\tau},\partial\Omega) := \{\gamma_{\tau}(\mathbf{u}) \mid \mathbf{u} \in \mathbf{H}(\mathrm{curl},\Omega)\}, \tag{11-112}$$

and that

$$\mathbf{H}\,(\mathrm{curl},\Omega)' = \mathbf{H}(\mathrm{div},\Omega) \tag{11-113}$$

$$\mathbf{H}^{-1/2}\,(\mathrm{curl}_\tau,\partial\Omega)' = \mathbf{H}^{-1/2}(\mathrm{div}_\tau,\partial\Omega) \tag{11-114}$$

where X' denotes the function space dual to X in the appropriate L^2 inner product.

11.3.2 Interior Penalty Based Domain Decomposition Method

In this section, we introduce a conformal DD method that does not require auxiliary variables to solve for time-harmonic Maxwell equations. The method is closely related to the Interior Penalty (IP) Discontinuous Galerkin (DG) methods of [61], [62]. A general derivation of the method leads to many possible formulations, but one that provides an optimal rate of convergence in solution error as well as robust iterative solver convergence is selected for further study.

When compared to the conventional FEM, the proposed method is less accurate for a given mesh due to energy dissipation on interfaces. As with all computational methods, solution accuracy to a prescribed tolerance can only be guaranteed using adaptive procedures that either produce finer computational meshes (*h*-refine) or increase the polynomial order of basis functions (*p*-refine) based on reliable *a posteriori* error estimators. We note that adaptive mesh refinement is most efficient when the numerical method gives an optimal error convergence rate. The current work therefore addresses two of the three key ingredients for a robust numerical method by providing an efficient, reliable solution procedure and an optimal rate of convergence. The final ingredients, adaptive refinement procedures, are left to future research and the work in [63], in the context of DG methods, may provide a starting point.

11.3.2.1 Boundary Value Problem

We begin by defining a Boundary Value Problem (BVP) for the decomposed problem of Fig. 11-25. It may be written as

$$\nabla\times\mu_{r1}^{-1}\nabla\times\mathbf{E}_1 - k_0^2\varepsilon_{r1}\mathbf{E}_1 = -jk_0\eta_0\mathbf{J}_1^{\mathrm{imp}} \qquad \text{in } \Omega_1 \tag{11-115}$$

$$\nabla\times\mu_{r1}^{-1}\nabla\times\mathbf{E}_2 - k_0^2\varepsilon_{r2}\mathbf{E}_2 = -jk_0\eta_0\mathbf{J}_2^{\mathrm{imp}} \qquad \text{in } \Omega_2 \tag{11-116}$$

$$\pi_\tau(\mathbf{E}_1) = \pi_\tau(\mathbf{E}_2) \qquad \text{on } \Gamma \tag{11-117}$$

$$\gamma_\tau\left(\mu_{r1}^{-1}\nabla\times\mathbf{E}_1\right) = \gamma_\tau(\mu_{r2}^{-1}\nabla\times\mathbf{E}_2) \qquad \text{on } \Gamma \tag{11-118}$$

$$\gamma_\tau\left(\mu_{r1}^{-1}\nabla\times\mathbf{E}_1\right) = jk_1\mu_{r1}^{-1}\pi_\tau(\mathbf{E}_1) \qquad \text{on } \widetilde{\partial\Omega}_1 \tag{11-119}$$

$$\gamma_\tau\left(\mu_{r2}^{-1}\nabla\times\mathbf{E}_2\right) = jk_2\mu_{r2}^{-1}\pi_\tau(\mathbf{E}_2) \qquad \text{on } \widetilde{\partial\Omega}_2 \tag{11-120}$$

where $\mathbf{E}_i \in \mathbf{H}_0\,(\mathrm{curl}, \Omega_i)$ represents the electric field in a subdomain. Note that $\mathbf{E}_1$ and $\mathbf{E}_2$ are allowed to be discontinuous on Γ. Equations (11-117) and (11-118) enforce the

necessary continuity of the electric and magnetic fields on the interface between subdomains and render the BVP above equivalent to that of the original problem without decomposition. Equations (11-119) and (11-120) provide a simple first-order absorbing boundary condition (ABC) on $\partial\Omega$, though other conditions may also be applied to the boundary. The impressed electric current is assumed to be given such that $\mathrm{J}_{\mathrm{i}}^{\mathrm{imp}} \in \mathbf{H}(\mathrm{div}, \Omega_i)$.

We ignore other boundary conditions (e.g., PEC, PMC, and impedance conditions) and sometimes omit discussion of the ABC treatment in what follows as they can be accounted for as in the conventional FEM.

11.3.2.2 Weak Formulation

To derive the weak form we first introduce the following residual quantities and their associated function spaces:

$$\mathbf{R}_{\Omega_1}^{(1)} := \nabla \times \mu_{r1}^{-1} \nabla \times \mathbf{E}_1 - k_0^2 \varepsilon_{r1} \mathbf{E}_1 + jk_0 \eta_0 \mathbf{J}_1^{\mathrm{imp}} \quad \in \mathbf{H}(\mathrm{div}, \Omega_1) \tag{11-121}$$

$$\mathbf{R}_{\Omega_2}^{(2)} := \nabla \times \mu_{r2}^{-1} \nabla \times \mathbf{E}_2 - k_0^2 \varepsilon_{r2} \mathbf{E}_2 + jk_0 \eta_0 \mathbf{J}_2^{\mathrm{imp}} \quad \in \mathbf{H}(\mathrm{div}, \Omega_2) \tag{11-122}$$

$$\mathbf{R}_{\Gamma}^{(3)} := \pi_\tau(\mathbf{E}_1) - \pi_\tau(\mathbf{E}_2) \quad \in \mathbf{H}^{-1/2}(\mathrm{curl}_\tau, \Gamma) \tag{11-123}$$

$$\mathbf{R}_{\Gamma}^{(4)} := \gamma_\tau\left(\mu_{r1}^{-1} \nabla \times \mathbf{E}_1\right) + \gamma_\tau\left(\mu_{r2}^{-1} \nabla \times \mathbf{E}_2\right) \quad \in \mathbf{H}^{-1/2}(\mathrm{div}_\tau, \Gamma) \tag{11-124}$$

$$\mathbf{R}_{\widetilde{\partial\Omega}_1}^{(5)} := \gamma_\tau\left(\mu_{r1}^{-1} \nabla \times \mathbf{E}_1\right) - jk_1 \mu_{r1}^{-1} \pi_\tau(\mathbf{E}_1) \quad \in \mathbf{H}^{-1/2}(\widetilde{\partial\Omega}_1) \tag{11-125}$$

$$\mathbf{R}_{\widetilde{\partial\Omega}_2}^{(6)} := \gamma_\tau\left(\mu_{r2}^{-1} \nabla \times \mathbf{E}_2\right) - jk_2 \mu_{r2}^{-1} \pi_\tau(\mathbf{E}_2) \quad \in \mathbf{H}^{-1/2}(\widetilde{\partial\Omega}_2). \tag{11-126}$$

These residuals can be interpreted in terms of physical error currents that support a difference between the exact field solution and that obtained through the numerical method. $\mathbf{R}_{\Omega 1}^{(1)}$ and $\mathbf{R}_{\Omega 2}^{(2)}$ represent scaled volume electric error currents, $jk_0\eta_0\mathbf{J}_{\Omega 1}^{\mathrm{err}}$ and $jk_0\eta_0\mathbf{J}_{\Omega 2}^{\mathrm{err}}$, respectively. Also, surface error currents exist on the interface due to $\mathbf{R}_{\Gamma}^{(3)}$ and $\mathbf{R}_{\Gamma}^{(4)}$. The former defines a rotated magnetic current, $\hat{\mathbf{n}}_i \times \mathbf{M}_{\Gamma}^{\mathrm{err}}$, whereas the latter gives an electric current, $\mathbf{J}_{\Gamma}^{\mathrm{err}}$.

Following the Galerkin procedure we introduce test functions to form proper dual pairs. These dual pairs can be interpreted via functional space arguments, or we may rely on a more physical interpretation using energy densities. These densities arise from dual pairs and we can then see that the volume electric currents, $\mathbf{R}_{\Omega 1}^{(\mathrm{i})}$, should be paired with volume electric fields to give rise to the familiar $\mathbf{E} \cdot \mathbf{J}$ density. Thus, the test functions, $\mathbf{w}_i$ are chosen from the same functional space as the electric field and we choose $(\mathbf{w}_1, \mathbf{w}_2) \in \mathbf{H}_0(\mathrm{curl}, \Omega_1) \times \mathbf{H}_0(\mathrm{curl}, \Omega_2)$. Similarly, we pair the rotated magnetic current of $\mathbf{R}_{\Gamma}^{(3)}$ with a rotated magnetic field to give a surface energy density of the form $\mathbf{H} \cdot \mathbf{M}$. Since the rotated magnetic field lies in the space $\mathbf{H}^{-1/2}(\mathrm{div}_\tau, \Gamma)$, we may use test functions of the form $\gamma_\tau(\mu_{ri}^{-1} \nabla \times \mathbf{w}_i)$. Lastly, the electric current of $\mathbf{R}_{\Gamma}^{(4)}$ is paired with a surface electric field to give a surface density of the form $\mathbf{E} \cdot \mathbf{J}$. The surface electric fields lie in the space $\mathbf{H}^{-1/2}(\mathrm{curl}_\tau, \Gamma)$ and we may use test functions $\pi_\tau(\mathbf{w}_i)$.

On Γ, two possibilities arise for the choice of basis functions, one from either side of the interface. Here, we simply choose an average of the two possibilities as testing functions. Now, we may write a linear combination of the weighted residuals

$$\begin{aligned}
&\left(\mathbf{w}_1, \mathbf{R}_{\Omega_1}^{(1)}\right)_{\Omega_1} + \left(\mathbf{w}_2, \mathbf{R}_{\Omega_2}^{(2)}\right)_{\Omega_2} \\
&+ c_3 \left\langle \gamma_\tau\left(\mu_{r1}^{-1}\nabla\times\mathbf{w}_1\right) - \gamma_\tau\left(\mu_{r2}^{-1}\nabla\times\mathbf{w}_2\right), \mathbf{R}_\Gamma^{(3)}\right\rangle_\Gamma + c_4\left\langle \pi_\tau(\mathbf{w}_1) + \pi_\tau(\mathbf{w}_2), \mathbf{R}_\Gamma^{(4)}\right\rangle_\Gamma \\
&+ c_5\left\langle \pi_\tau(\mathbf{w}_1), \mathbf{R}_{\widetilde{\partial\Omega_1}}^{(5)}\right\rangle_{\partial\Omega_1} + c_4\left\langle \pi_\tau(\mathbf{w}_2), \mathbf{R}_{\widetilde{\partial\Omega_2}}^{(6)}\right\rangle_{\partial\Omega_2} \\
&+ \left\langle \pi_\tau(\mathbf{w}_1) - \pi_\tau(\mathbf{w}_2), p\mathbf{R}_\Gamma^{(3)}\right\rangle_\Gamma + \left\langle \gamma_\tau\left(\mu_{r1}^{-1}\nabla\times\mathbf{w}_1\right) + \gamma_\tau\left(\mu_{r2}^{-1}\nabla\times\mathbf{w}_2\right), \mathbf{R}_\Gamma^{(4)}\right\rangle_\Gamma = 0
\end{aligned} \tag{11-127}$$

with coefficients c_3, c_4, c_5, c_6, p and q to be determined based on accuracy and convenience.

We note that the first four residuals are tested using the appropriate functions to give proper dual pairings whereas the ABC residuals, $\mathbf{R}_{\widetilde{\partial\Omega_1}}^{(5)}$ and $\mathbf{R}_{\widetilde{\partial\Omega_2}}^{(6)}$, are tested with curl-conforming functions as in the conventional FEM.

The final two terms on the left-hand side of (11-127), inspired by the DG and IP methods (see, e.g., [61], [62], [64], [65]), are included to penalize the discontinuities of the electric and magnetic fields across Γ. We see their importance upon considering the boundary testings

$$\begin{aligned}
&\left\langle \gamma_\tau\left(\mu_{r1}^{-1}\nabla\times\mathbf{w}_1\right), c_3\mathbf{R}_\Gamma^{(3)} + q\mathbf{R}_\Gamma^{(4)}\right\rangle_\Gamma = 0 \qquad \forall\mathbf{w}_1 \in \mathbf{H}_0(\text{curl}, \Omega_1) \\
&\left\langle \gamma_\tau\left(\mu_{r2}^{-1}\nabla\times\mathbf{w}_2\right), c_3\mathbf{R}_\Gamma^{(3)} - q\mathbf{R}_\Gamma^{(4)}\right\rangle_\Gamma = 0 \qquad \forall\mathbf{w}_2 \in \mathbf{H}_0(\text{curl}, \Omega_2)
\end{aligned} \tag{11-128}$$

and

$$\begin{aligned}
&\left\langle \pi_\tau(\mathbf{w}_1), c_4\mathbf{R}_\Gamma^{(4)} + p\mathbf{R}_\Gamma^{(3)}\right\rangle_\Gamma = 0 \qquad \forall\mathbf{w}_1 \in \mathbf{H}_0(\text{curl}, \Omega_1) \\
&\left\langle \pi_\tau(\mathbf{w}_2), c_4\mathbf{R}_\Gamma^{(4)} - p\mathbf{R}_\Gamma^{(3)}\right\rangle_\Gamma = 0 \qquad \forall\mathbf{w}_2 \in \mathbf{H}_0(\text{curl}, \Omega_2).
\end{aligned} \tag{11-129}$$

The coefficients appearing in (11-128) and (11-129) can be chosen to weakly enforce transmission conditions on the interface between subdomains and thereby satisfy (11-117) and (11-118). For a planar interface, the theory of non-overlapping DD methods for scalar and vector Helmholtz equations indicates that convergent iterative methods (for propagative modes) may be obtained by enforcing a complex, mixed TC [66]–[68]. In the present work, evanescent modes are handled through the use of a Krylov subspace iterative solver, as is common in DD methods for wave phenomena [69]. Specifically, we choose c_3 and c_4 real, and set $p = -jc_4\tilde{k}/\tilde{\mu}_r$, $q = jc_3\tilde{\mu}_r/\tilde{k}$ with $\tilde{k} = (k_1 + k_2)/2$ and $\tilde{\mu}_r = (\tilde{\mu}_{r1} + \tilde{\mu}_{r2})/2$. Then, the TCs become the familiar ones of non-overlapping DD. Specifically

$$\begin{aligned}
&\gamma_\tau\left(\mu_{r1}^{-1}\nabla\times\mathbf{E}_1\right) - j\tilde{k}\tilde{\mu}_r^{-1}\pi_\tau(\mathbf{E}_1) = -\gamma_\tau\left(\mu_{r2}^{-1}\nabla\times\mathbf{E}_2\right) - j\tilde{k}\tilde{\mu}_r^{-1}\pi_\tau(\mathbf{E}_2) \\
&\gamma_\tau\left(\mu_{r2}^{-1}\nabla\times\mathbf{E}_2\right) - j\tilde{k}\tilde{\mu}_r^{-1}\pi_\tau(\mathbf{E}_2) = -\gamma_\tau\left(\mu_{r1}^{-1}\nabla\times\mathbf{E}_1\right) - j\tilde{k}\tilde{\mu}_r^{-1}\pi_\tau(\mathbf{E}_1).
\end{aligned} \tag{11-130}$$

We denote the method that uses the Robin TC above as the IP-DD method.

Now, after integrating the first two terms of (11-127) by parts, we obtain

$$\begin{aligned}
&\left(\nabla\times\mathbf{w},\mu_r^{-1}\nabla\times\mathbf{E}\right)_\Omega - k_0^2(\mathbf{w},\varepsilon_r\mathbf{E})_\Omega \\
&\quad+\left\langle\pi_\tau(\mathbf{w}_1),\gamma_\tau\left(\mu_{r1}^{-1}\nabla\times\mathbf{E}_1\right)\right\rangle_{\partial\Omega_1}+\left\langle\pi_\tau(\mathbf{w}_2),\gamma_\tau\left(\mu_{r2}^{-1}\nabla\times\mathbf{E}_2\right)\right\rangle_{\partial\Omega_2} \\
&\quad+c_3\left\langle\gamma_\tau\left(\mu_{r1}^{-1}\nabla\times\mathbf{w}_1\right)-\gamma_\tau\left(\mu_{r2}^{-1}\nabla\times\mathbf{w}_2\right),[\![\mathbf{E}]\!]_\pi\right\rangle_\Gamma \\
&\quad+2c_4\left\langle\pi_\tau(\mathbf{w}_1)+\pi_\tau(\mathbf{w}_2),\{\!\{\mu_r^{-1}\nabla\times\mathbf{E}\}\!\}_\gamma\right\rangle_\Gamma \\
&\quad-jc_4\left\langle[\![\mathbf{w}]\!]_\pi,\frac{\tilde{k}}{\bar{\mu}_r}[\![\mathbf{E}]\!]_\pi\right\rangle_\Gamma+jc_3\left\langle[\![\mu_r^{-1}\nabla\times\mathbf{w}]\!]_\gamma,\frac{\bar{\mu}_r}{\tilde{k}}[\![\mu_r^{-1}\nabla\times\mathbf{E}]\!]_\gamma\right\rangle_\Gamma \\
&\quad+c_5\left\langle\pi_\tau(\mathbf{w}_1),\gamma_\tau\left(\mu_{r1}^{-1}\nabla\times\mathbf{E}_1\right)-jk_1\mu_{r1}^{-1}\pi_\tau(\mathbf{E}_1)\right\rangle_{\widetilde{\partial\Omega}_1} \\
&\quad+c_6\left\langle\pi_\tau(\mathbf{w}_2),\gamma_\tau\left(\mu_{r2}^{-1}\nabla\times\mathbf{E}_2\right)-jk_2\mu_{r2}^{-1}\pi_\tau(\mathbf{E}_2)\right\rangle_{\widetilde{\partial\Omega}_2} \\
&=-jk_0\eta_0(\mathbf{w},\mathbf{J}^{\text{imp}})_\Omega.
\end{aligned}\tag{11-131}$$

Turning to the choice of constant coefficients, we first set $c_5 = c_6 = -1$ to enforce the ABCs on $\partial\Omega$ as in the usual FEM. Examining (11-131) and assuming that the media are isotropic and μ_r is real, we can obtain a (convenient) symmetric formulation if $c_3 = -c_4 = 1/2$. Then, the weak formulation is given by

$$\begin{aligned}
&\left(\nabla\times\mathbf{w},\mu_r^{-1}\nabla\times\mathbf{E}\right)_\Omega - k_0^2(\mathbf{w},\varepsilon_r\mathbf{E})_\Omega \\
&\quad+\left\langle\{\!\{\mu_r^{-1}\nabla\times\mathbf{w}\}\!\}_\gamma,[\![\mathbf{E}]\!]_\pi\right\rangle_\Gamma+\left\langle[\![\mathbf{w}]\!]_\pi,\{\!\{\mu_r^{-1}\nabla\times\mathbf{E}\}\!\}_\gamma\right\rangle_\Gamma \\
&\quad+\frac{j}{2}\left\langle[\![\mathbf{w}]\!]_\pi,\frac{\tilde{k}}{\tilde{\mu}_r}[\![\mathbf{E}]\!]_\pi\right\rangle_\Gamma+\frac{j}{2}\left\langle[\![\mu_r^{-1}\nabla\times\mathbf{w}]\!]_\gamma,\frac{\tilde{\mu}_r}{\tilde{k}}[\![\mu_r^{-1}\nabla\times\mathbf{E}]\!]_\gamma\right\rangle_\Gamma \\
&\quad+jk_0\left\langle\pi_\tau(\mathbf{w}),\sqrt{\mu_r^{-1}\varepsilon_r}\,\pi_\tau(\mathbf{E})\right\rangle_{\partial\Omega} \\
&=-jk_0\eta_0(\mathbf{w},\mathbf{J}^{\text{imp}})_\Omega.
\end{aligned}\tag{11-132}$$

We also note that many formulations can be derived by selecting different coefficients in (11-130). However, it is as yet unclear how an effective precon-ditioner can be constructed for the resulting matrix. For example, with $q = 0$, the symmetric, nonsymmetric, and incomplete interior penalty methods can be obtained by setting $c_4 = \frac{1}{2}, \frac{1}{2}$, or 0, respectively. The approximating properties of these methods have been analyzed in [61] and [62]. Note that some choices of coefficients may lead to suboptimal rates of convergence in the solution. We demonstrate via numerical experiment in Sections 11.3.4, that an optimal rate of convergence is obtained with the IP-DD method.

11.3.3 Discrete Formulation

While the IP-DD method is applicable to both conformal and nonconformal meshes, we restrict ourselves here to the conformal case and introduce a partitioning, $\mathcal{K}$, of Ω into a

conformal mesh of tetrahedra, K. To form the subdomains Ω_1 and Ω_2, the mesh is partitioned by grouping whole tetrahedra to give submeshes $\mathcal{K}_1$ and $\mathcal{K}_2$. The surface meshes induced by the partitioning are denoted by $\mathcal{T}_x$, with the subscript x referring to the original domain. For example, the triangulation on Γ is denoted by $\mathcal{T}_\Gamma$ and that on $\partial\Omega$ is given by $\mathcal{T}_{\partial\Omega}$. On each of the subdomains, we define discrete trial and test functions, $\mathbf{E}_i^h \in \mathbf{X}_i^h$ and $\mathbf{w}_i^h \in \mathbf{X}_i^h$ respectively, with $\mathbf{X}_i^h \subset \mathbf{H}_0(\text{curl}, \Omega_i)$. Here, $\mathbf{X}_i^h$ is taken to be the space of second-order, first kind Nedelec curl-conforming basis functions [70] over $\mathcal{K}_i$, given in [71]. We also set $\mathbf{E}^h := (\mathbf{E}_1^h, \mathbf{E}_2^h)$, $\mathbf{w}^h := (\mathbf{w}_1^h, \mathbf{w}_2^h)$, and $\mathbf{X}^h := \mathbf{X}_1^h \times \mathbf{X}_2^h$. The discrete problem is then given by: Seek $\mathbf{E}^h \in \mathbf{X}^h$ such that

$$a(\mathbf{w}^h, \mathbf{E}^h)_{\mathcal{K}} = -jk_0\eta_0(\mathbf{w}^h, \mathbf{J}^{\text{imp}})_{\mathcal{K}} \qquad \forall \mathbf{w}^h \in \mathbf{X}^h. \tag{11-133}$$

The sesquilinear form in (11-133) is given by

$$\begin{aligned} a(\mathbf{u},\mathbf{v})_{\mathcal{K}} :=& \left(\nabla\times\mathbf{u},\, \mu_r^{-1}\nabla\times\mathbf{v}\right)_{\mathcal{K}} - k_0^2(\mathbf{u},\, \varepsilon_r\mathbf{v})_{\mathcal{K}} \\ &+ \left\langle \{\!\{\mu_r^{-1}\nabla\times\mathbf{u}\}\!\}_\gamma, [\![\mathbf{v}]\!]_\pi \right\rangle_{\mathcal{T}} + \left\langle [\![\mathbf{u}]\!]_\pi, \{\!\{\mu_r^{-1}\nabla\times\mathbf{u}\}\!\}_\gamma \right\rangle_{\mathcal{T}} \\ &+ \frac{j}{2}\left\langle [\![\mathbf{u}]\!]_\pi, \frac{\tilde{k}}{\tilde{\mu}_r}[\![\mathbf{v}]\!]_\pi \right\rangle_{\mathcal{T}} + \frac{j}{2}\left\langle [\![\mu_r^{-1}\nabla\times\mathbf{u}]\!]_\gamma, \frac{\tilde{\mu}_r}{\tilde{k}}[\![\mu_r^{-1}\nabla\times\mathbf{v}]\!]_\gamma \right\rangle_{\mathcal{T}} \\ &+ jk_0\left\langle \pi_\tau(\mathbf{u}), \sqrt{\mu_r^{-1}\varepsilon_r}\,\pi_\tau(\mathbf{v}) \right\rangle_{\mathcal{T}_{\partial\Omega}}. \end{aligned} \tag{11-134}$$

After expanding the field in terms of the basis functions, the discrete system (11-133) can then be cast as a matrix equation for the electric field coefficients E_1 and E_2:

$$\begin{pmatrix} A_1 & C_{12} \\ C_{21} & A_2 \end{pmatrix} \begin{pmatrix} E_1 \\ E_2 \end{pmatrix} = \begin{pmatrix} b_1 \\ b_2 \end{pmatrix} \tag{11-135}$$

where

$$\begin{aligned} A_i &= \begin{pmatrix} A_i^{\text{II}} & A_i^{\text{IB}} \\ A_i^{\text{BI}} & A_i^{\text{BB}} + D_{ii}^{\text{B}} + \left(D_{ii}^{\text{B}}\right)^{\text{T}} + T_{ii}^{\text{B}} + S_{ii}^{\text{B}} + R_i^{\text{B}} \end{pmatrix} \\ C_{ij} = (C_{ji})^{\text{T}} &= \begin{pmatrix} 0 & 0 \\ 0 & -D_{ij}^{\text{B}} - \left(D_{ji}^{\text{B}}\right)^{\text{T}} - T_{ij}^{\text{B}} + S_{ij}^{\text{B}} \end{pmatrix} \\ E_i &= \begin{pmatrix} E_i^{\text{I}} \\ E_i^{\text{B}} \end{pmatrix} \\ b_i &= \begin{pmatrix} b_i^{\text{I}} \\ b_i^{\text{B}} \end{pmatrix}. \end{aligned} \tag{11-136}$$

In (11-136), the superscripts $x \in \{\mathrm{I}, \mathrm{B}\}$ correspond, respectively, to tetrahedra interior to the subdomain and those adjacent to its boundary, $\partial\Omega_i$. The block matrices are given by

$$\begin{aligned}
A_i^{\mathrm{xx}} &:= \left(\nabla \times \mathbf{w}_i, \mu_{ri}^{-1} \nabla \times \mathbf{w}_i\right)_{\mathcal{K}_i} - k_0^2 (\mathbf{w}_i, \varepsilon_{ri} \mathbf{w}_i)_{\mathcal{K}_i} \\
D_{ij}^{\mathrm{B}} &:= \frac{1}{2} \left\langle \pi_\tau(\mathbf{w}_i), \gamma_\tau\left(\mu_{rj}^{-1} \nabla \times \mathbf{w}_j\right) \right\rangle_{\mathcal{T}_\Gamma} \\
T_{ij}^{\mathrm{B}} &:= \frac{j}{2} \left\langle \pi_\tau(\mathbf{w}_i), \frac{\tilde{k}}{\tilde{\mu}_r} \pi_\tau(\mathbf{w}_j) \right\rangle_{\mathcal{T}_\Gamma} \\
S_{ij}^{\mathrm{B}} &:= \frac{j}{2} \left\langle \gamma_\tau\left(\mu_{ri}^{-1} \nabla \times \mathbf{w}_i\right), \frac{\tilde{\mu}_r}{\tilde{k}} \gamma_\tau\left(\mu_{rj}^{-1} \nabla \times \mathbf{w}_j\right) \right\rangle_{\mathcal{T}_\Gamma} \\
R_i^{\mathrm{B}} &:= jk_0 \left\langle \pi_\tau(\mathbf{w}_i), \sqrt{\mu_{ri}^{-1} \varepsilon_{ri}}\, \pi_\tau(\mathbf{w}_i) \right\rangle_{\widetilde{\mathcal{T}_{\partial\Omega_i}}}.
\end{aligned} \tag{11-137}$$

We can solve (11-135) via a preconditioned Krylov subspace method. The simplest preconditioner is of block-Jacobi type and can be written as

$$M = \begin{pmatrix} A_1 & 0 \\ 0 & A_2 \end{pmatrix}. \tag{11-138}$$

The system to be solved is of the form $M^{-1}Ax = M^{-1}b$ and we see that application of the preconditioner requires the inversion of each subdomain matrix, A_i. The subdomain matrices can be factorized in a preprocessing step or solved via another preconditioned Krylov method at each iteration (an "inner loop" iteration). Here, as a compromise between solution speed and memory usage, we use an incomplete factorization of each subdomain matrix to construct the preconditioner.

In addition to (11-138), other block preconditioners (e.g., Gauss-Seidel) may also be used. In serial these preconditioners entail a reasonable amount of additional computational effort; in parallel they may significantly increase communication costs.

11.3.4 Numerical Results

In this section, we study the proposed method via numerical experiment. We restrict ourselves to the symmetric case with μ_r real and use a preconditioned Conjugate Residual (CR) solver [72] for the solution of (11-135). Note that despite the increased memory requirement, we prefer the CR algorithm to a Conjugate Gradient method because we have found that it provides more stable convergence. The convergence criteria for the CR solver is defined as

$$\epsilon = \frac{\|M^{-1}(Ax - b)\|_2}{\|M^{-1}b\|_2}. \tag{11-139}$$

Note that for serial methods we have found that a block Gauss-Seidel preconditioner with truncated Generalized Conjugate Residual (GCR) method [73] to be a better approach.

To apply the proposed method here, the subdomains, $\mathcal{K}_i$, $i = 1, \ldots, N_p$, are formed by partitioning the tetrahedral mesh $\mathcal{K}$ using the METIS software package [74]. Drop tolerances of $\xi = 10^{-6}$ are used for the preconditioner's incomplete Choleski factorizations. Although double-precision arithmetic is used throughout, the factorizations are performed using only single-precision. First-order ABCs are used to truncate the computational regions unless otherwise noted. All computational statistics are reported using a workstation with two quad-core 64-bit Intel Xeon X5450 CPUs and 32 GB of RAM. Unless otherwise specified, 8 threads are used in an OpenMP [75] threaded implementation. All computational timings are reported as wall clock times.

11.3.4.1 Rectangular Waveguide

We first use an X-band (WR-90) rectangular waveguide excited by a TE_{10} mode and operating at 10 GHz to verify that with mesh refinement, the solution converges to the exact one at the proper rate. Successively finer quasi-uniform meshes are generated and then partitioned into two domains for the simulations. The waveguide ports are terminated with perfectly matched layers (PMLs). Figures 11-26a and 11-26b show that reflection and transmission coefficients computed with the proposed method, and the method of [53] that employs divergence-conforming cement variables, converge at the same rate as those of the FEM.

Figure 11-27 shows the number of CR iterations required for the two DD methods' solutions as the mesh is refined. The figure clearly demonstrates the IP-DD method's improvement over that of [53]. The figure also shows that solver convergence is sensitive to mesh size and a linear dependence is observed. This is due to the fact that the number of evanescent modes on the interface increases linearly as the mesh is refined. We remark that although a stopping criteria of $\epsilon = 10^{-8}$ is used here, a tolerance several orders of magnitude larger is usually sufficient for the accuracy required of practical simulations.

Next, we use an $8\lambda_0$ long segment of waveguide to examine the energy loss due to the method. We first solve the problem via a conventional FEM solver and then partition it with transverse slices into $N_p \in \{2, 4, 8, 16\}$ partitions and solve via the proposed method. The total power at each port is determined and normalized against the power

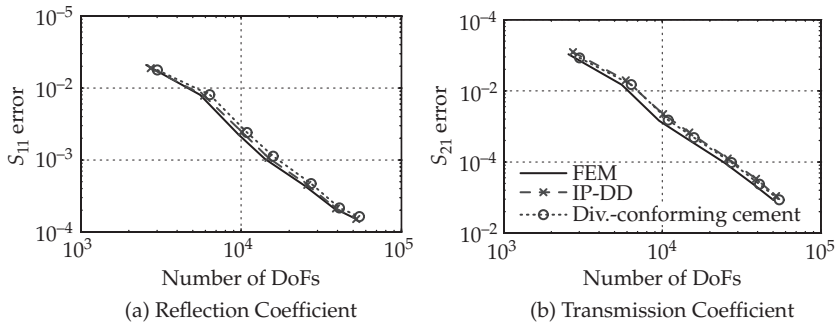

Figure 11-26 Error convergence of waveguide S-parameters

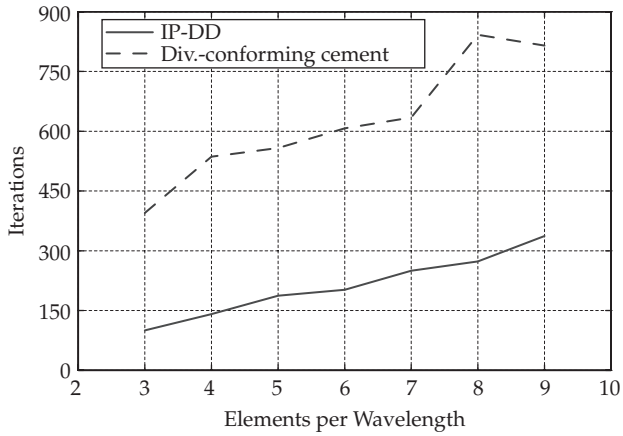

Figure 11-27 Solver convergence for waveguide with respect to mesh size, $\epsilon = 10^{-8}$

obtained from the FEM solution. The experiment is repeated for several mesh sizes and the results are shown plotted in Fig. 11-28. We first note that the total power decreases linearly as the number of domains is increased. That is, each additional interface introduces a constant amount of loss. We also note that once again, as the mesh is refined, the solution converges toward the exact one at the optimal rate.

We note that in the present method, as with the conventional FEM and all numerical methods, no guarantee in solution accuracy is available unless *(h* or *p)* adaptive procedures are employed. No simple heuristic on mesh size is sufficient to guarantee a certain level of numerical accuracy. The important point for the method is that arbitrary solution accuracy can be obtained via mesh refinement or by increasing the polynomial order of the basis functions. If the method converges at the optimal rate, as shown above, the adaptive procedure is most efficient. Adaptive refinement for the present method will differ slightly from the conventional FEM in that additional refinement on subdomain

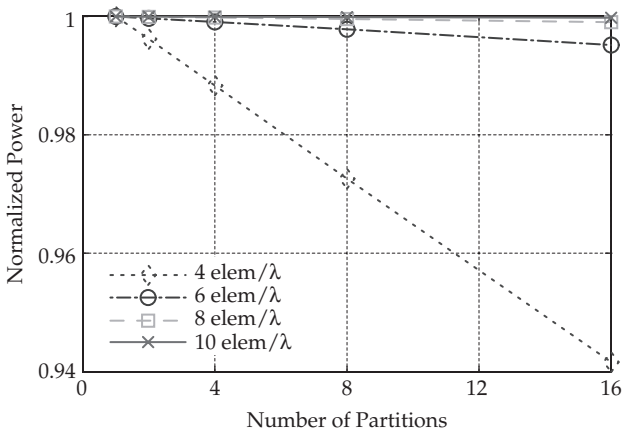

Figure 11-28 Energy loss in a waveguide with varying number of partitions and mesh size

interfaces may be desired. This local mesh refinement or polynomial enrichment on the interface would mitigate the energy dissipation since the order of the error is always on the same order of the error of the FEM method used within each subdomain.

11.3.4.2 Coated Sphere

We further examine the accuracy of the proposed method using a plane-wave incident upon a dielectric-coated perfectly electrically conducting (PEC) sphere. The radii of the PEC sphere and the outer surface of the coating are $r_1 = 1\lambda_0$ and $r_2 = 1.2\lambda_0$, respectively. The coating has relative permittivity $\varepsilon_r = 4$ and the domain is truncated by a sphere of radius $r_3 = 3.2\lambda_0$. The bistatic radar cross-section (RCS) is found via a conventional FEM solver and the proposed method with $N_p \in \{50, 100, 200\}$ partitions. The error in RCS is determined using

$$\text{RCS Error} = \frac{\sqrt{\int_0^{2\pi}\int_0^{\pi} |\sigma_{\text{ref}}(\theta,\phi) - \sigma_{\text{num}}(\theta,\phi)|^2 \sin\theta \, d\theta \, d\phi}}{\sqrt{\int_0^{2\pi}\int_0^{\pi} |\sigma_{\text{ref}}(\theta,\phi)|^2 \sin\theta \, d\theta \, d\phi}}, \tag{11-140}$$

where σ_{num} is the numerical solution and σ_{ref} is a reference solution obtained using the Mie series. Figure 11-29 shows that the solution of the proposed method once again converges at a rate equal to that of the FEM. Note that as the number of subdomains is increased, more error is introduced, as evidenced by the slight upward shift in the curves with increasing N_p. This error is due to the loss of energy previously demonstrated in Section 11.3.4. The rates of convergence remain optimal and diminish as the solutions approach one where the error is dominated by the truncation error of the simple first order absorbing boundary condition. The bistatic RCS for mesh size $h = \lambda_0/6$ is given in Fig. 11-30 and demonstrates good agreement with the Mie Series solution.

We now study the performance of the proposed method by comparing it to a *p*-type multiplicative Schwartz (pMUS) preconditioned FEM solver [76]. Here, only a single thread is used for a more fair comparison of the methods. It should be noted however,

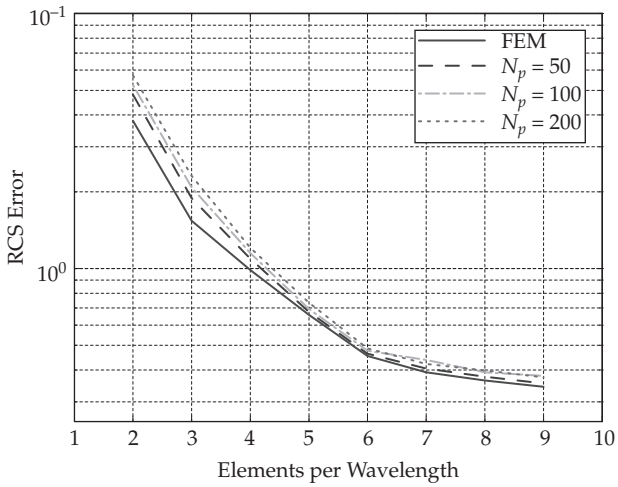

Figure 11-29 RCS error for coated sphere with varying number of partitions and mesh size

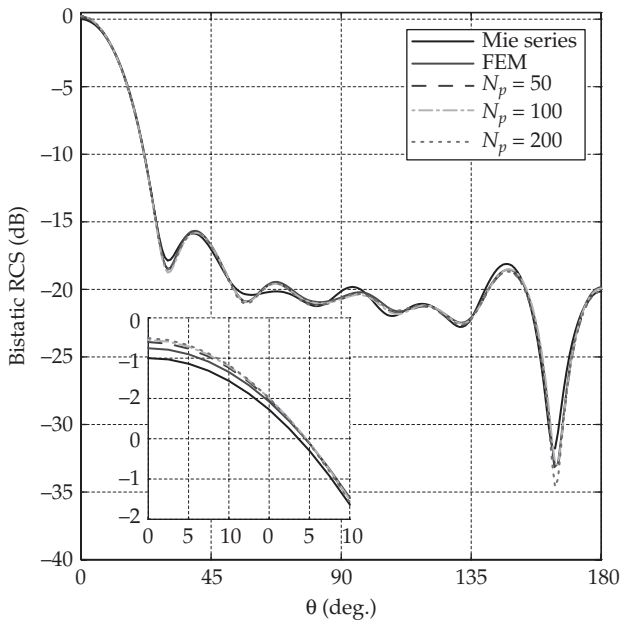

Figure 11-30 Bistatic RCS for coated sphere with varying number of partitions, $h = \lambda_0/6$, $\phi = 0$

that one of the IP-DD's benefits is that it is an efficient parallel algorithm. We begin at an operating frequency of $f = 50$ MHz and use a coated sphere with $r_1 = 0.5\lambda_0$, $r_2 = 0.6\lambda_0$, $r_3 = 0.75\lambda_0$, and $\varepsilon_r = 4$. The domain is meshed with $h = \lambda_0/5$ and solved via pMUS-FEM (that we denote by $N_p = 1$) and the proposed method with $N_p \in \{25, 50\}$ partitions. The experiment is repeated for higher frequencies with the same computational domain and a new mesh such that $h = \lambda_0/5$. A drop tolerance of $\xi = 10^{-3}$ is used for the factorizations of subdomain blocks.

The computational statistics are given in Table 11-2 where we see that for small problem geometries, the pMUS-FEM method is superior in terms of convergence and solution time. Also, its memory requirements are reasonably low.

As the electrical size of the problem increases, we see that the pMUS preconditioner is no longer effective and the solver fails to converge to $\epsilon = 10^{-3}$ within 1000 iterations. However, the proposed method is still able to obtain a solution.

The time and memory required for pMUS-FEM grow large due to the factorizations of large subblocks in the FEM matrix (that are obtained by splitting the hierarchical DoFs according to polynomial order). The time and memory required by the proposed method remains low due to the ability to control the size of the subblocks required for factorization; increasing N_p leads to smaller subblocks for factorizations. Of course, the energy considerations discussed above and the effect on solution time must also be considered in determining the number of partitions to employ.

We now use the largest of the coated spheres to examine the parallel scalability of the method. We use $N_p = 50$ subdomains and solve with 1 to 8 threads. The parallel speedup is measured as the total solution time required with t threads divided by the time required by the serial method. The results are shown in Fig. 11-31 and illustrate that a linear speedup is obtained when up to 4 threads are used. Beyond this, the

N_p	Frequency (MHz)	Degrees of Freedom	Iterations ($\epsilon = 10^{-3}$)	Preconditioner Time (s)	Solution Time (s)	Peak Memory Usage (MB)
1	50	11,382	6	1	0.3	26
	100	77,868	54	20	18	190
	150	256,196	40	213	53	699
	200	612,726	a	974	—	1792
	250	1,067,078	—	2670	—	3553
	300	1,875,096	—	9215	—	7692
25	50	15,016	49	0.5	1.4	8
	100	90,088	118	19	31	20
	150	284,204	161	225	179	74
	200	662,938	185	1210	593	213
	250	1,136,124	170	3752	1095	434
	300	1,978,766	240	11923	3190	870
50	50	17,154	72	0.3	2.3	8
	100	95,624	146	11	35	20
	150	296,066	135	118	135	52
	200	684,042	239	659	677	118
	250	1,166,672	188	2110	1082	202
	300	2,024,852	352	5833	4040	402

[a]Failed to converge within 1000 CR iterations

TABLE 11-2 Computational Statistics for Coated Sphere Simulations

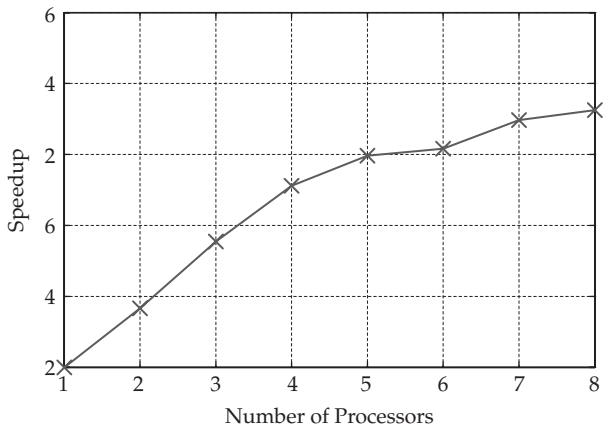

FIGURE 11-31 Parallel speedup for a coated sphere

speedup degrades. This can be explained by the fact that the processors of the dual quad-core machine are not truly parallel in terms of memory access. The four processors on a single die share two banks of 6 MB L2 cache. When more than two processors are used on a die (or more than four overall), the cache must be shared and this causes the observed degradation in speedup. Because the algorithm itself is highly parallel, we expect it to scale extremely well given the proper architecture.

11.3.4.3 Dielectric Cube

We now simulate a plane-wave incident upon a dielectric cube with permittivity $\varepsilon_r = 2$ and edge length $l_1 = 1.2\lambda_0$. The scatterer is enclosed within a larger vacuum-filled cube with edge length $l_2 = 2\lambda_0$. The model is meshed quasi-uniformly with $h = \lambda_0/6$. In Fig. 11-32a, solver convergence with respect to the number of partitions is examined. A fit through the data shows a dependence of about $N_p^{\frac{1}{8}}$ in the number of iterations and demonstrates an insensitivity to the number of partitions used in simulation.

Starting from a similar geometry with $l_1 = 0.6\lambda_0$, $l_2 = 1\lambda_0$, $h = \lambda_0/6$, and $N_p = 4$, we study the behavior as problem size increases. To do so, the cube volume *and* N_p are doubled for successive simulations. h is kept constant and the results of Fig. 11-32b demonstrate a dependence of the iterations on number of DoFs, N, of about $N^{\frac{1}{7}}$ and therefore very good scalability with respect to problem size.

11.3.4.4 Conformal Vivaldi Array with Meander-Line Polarizer

To examine the proposed method's performance on large-scale problems, a 7×7 Vivaldi antenna array and a meander-line polarizer are simulated. The geometrical specifications of the antenna elements and polarizer can be found in [51] and [77] (App. C.8), respectively. After meshing, the mesh is transformed so as to be conformal to a spherical surface. The geometry and mesh are depicted in Fig. 11-33 where the polarizer is placed $\frac{2}{3}\lambda_0$ away from the antenna aperture. The effect of the meander-lines is to change the field polarization from linear to circular. By using two such polarizers, the direction of linear polarization may be rotated. This may be desirable when, due to physical constraints, rotating the polarizers may be far simpler than manipulating the antenna. The simulation is performed at 5 GHz with $N_p = 1000$ and requires 10,275,060 DoFs. Preconditioner setup and matrix solution require 4 minutes, and 22 minutes, respectively. 226 CR iterations are required ($\epsilon = 10^{-2}$) and peak memory usage is 22.4 GB. The electric field magnitude on the antenna, ground plane and exterior truncation surface are shown in Fig. 11-34 on a logarithmic scale. The radiation field pattern of the array is given in Fig. 11-35.

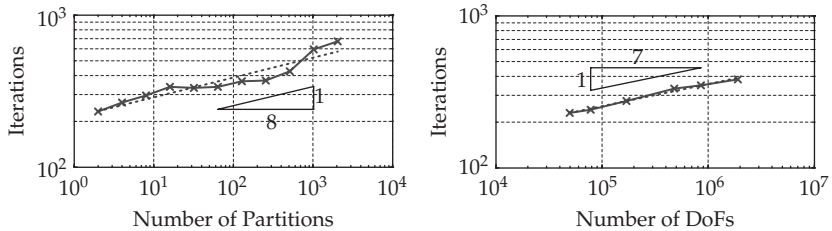

(a) Increasing number of partitions

(b) Increasing problem size and number of partitions

Figure 11-32 Dielectric cube solver convergence with respect to varying problem parameters, $\epsilon = 10^{-8}$

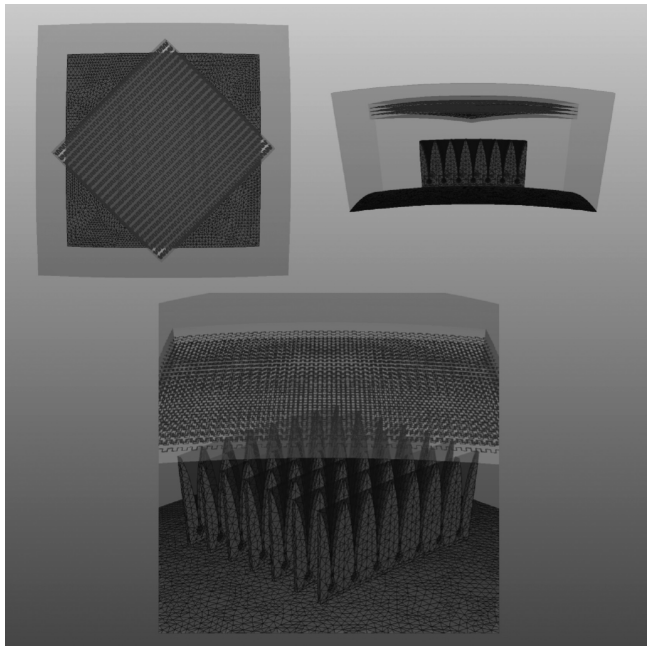

Figure 11-33 Conformal 7 × 7 Vivaldi array with meander-line polarizer: geometry and mesh

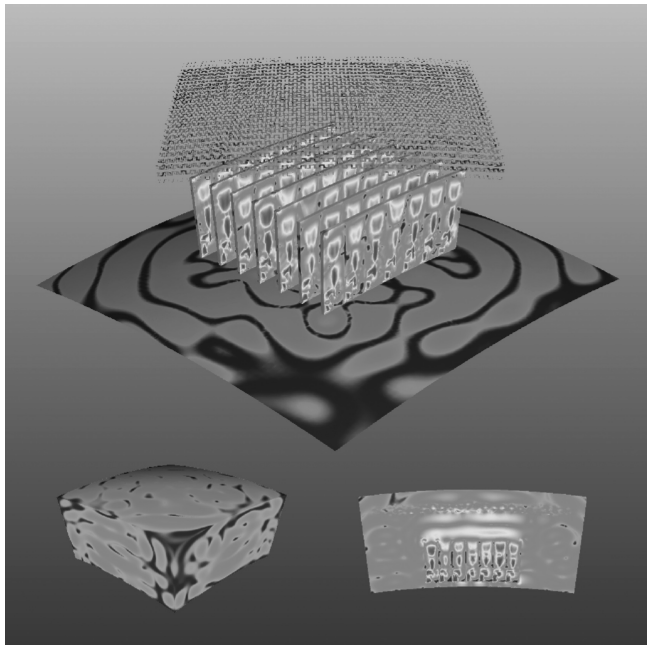

Figure 11-34 Conformal 7 × 7 Vivaldi array with meander-line polarizer: electric field magnitude (log. scale)

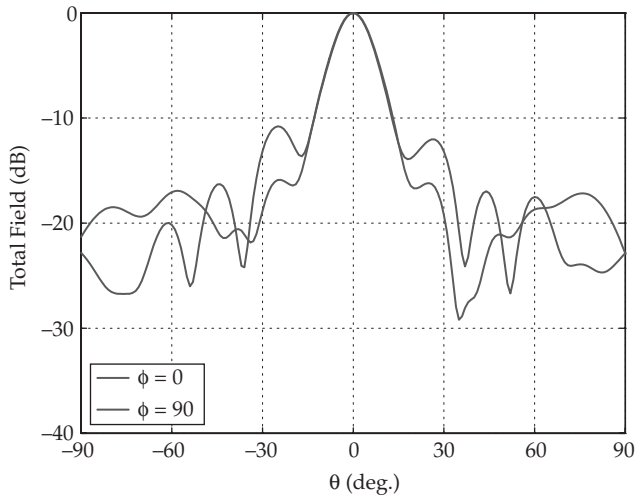

FIGURE 11-35 Radiation pattern of a conformal 7 × 7 Vivaldi array with meander-line polarizer

11.3.4.5 Dipole Array in an Aircraft Radome

Next, a circular array of 137 quarter-wavelength dipoles operating at $f = 5$ GHz is simulated in the presence of a conical dielectric aircraft radome with $\varepsilon_r = 3$. The array and radome are shown in Fig. 11-36a along with a shape-conforming truncation surface $\frac{1}{3}\lambda_0$ away from the radome's exterior. The radome has length $14.7\lambda_0$, outer diameter $7\lambda_0$,

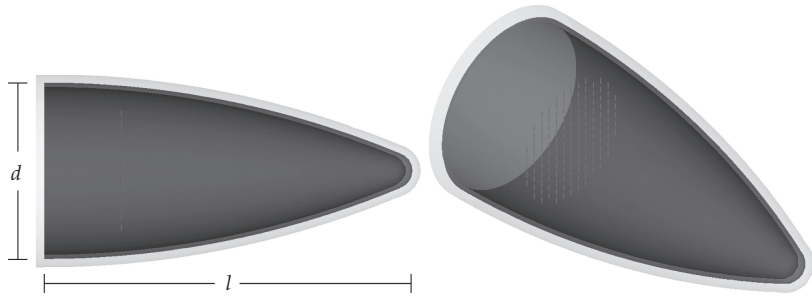

(a) Geometry, $l = 14.7\ \lambda_0$, $d = 7\ \lambda_0$

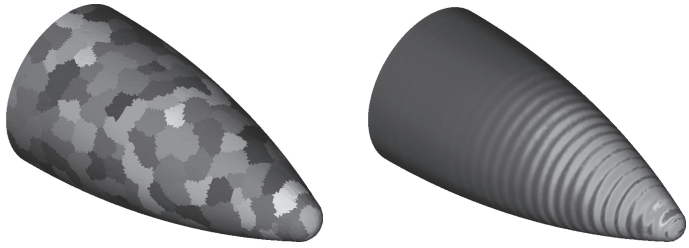

(b) Mesh Partition (c) Electric Field Magnitude

FIGURE 11-36 Aircraft radome with circular dipole array

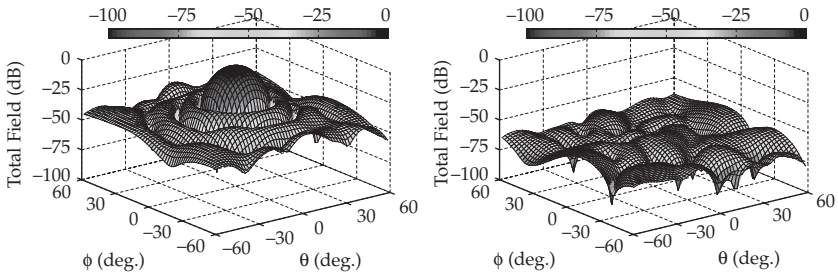

Figure 11-37 Radiation patterns of a circular dipole array

and thickness $\frac{1}{6}\lambda_0$, The mesh of 1,993,853 tetrahedra is partitioned into 500 domains (shown in Fig. 11-36b) and results in 14,370,776 DoFs. Preconditioner setup requires 32 minutes, while 21 minutes are required for 82 CR iterations ($\epsilon = 10^{-2}$). Peak memory usage is 24.5 GB. The magnitude of the electric field on the radome is shown in Fig. 11-36c. Figures 11-37 and 11-38 show, respectively, the radiation field patterns of the dipole array alone and in the presence of the radome. The effect of the radome on the copolarization is apparent in the increased level of the sidelobes, with the first one increasing from –28 to –12 dB relative to the main lobe. Significant cross-polarization is also introduced, with the peak value increasing from –55 to –19 dB.

11.3.4.6 Horn Antenna Array Fed by a Rotman Lens

The next electrically large simulation is that of a horn antenna array fed by a Rotman lens. The goal of the lens is to provide linear phase to an antenna array such that the radiated power can be guided in a particular direction. The geometry is depicted in Fig. 11-39. The lens has width $12\lambda_0$ and length $10.4\lambda_0$ at the operating frequency in the upper C to lower X band. The lens is filled with a dielectric of permittivity $\varepsilon_r = 2.5 - j0.00475$. Sixteen input ports and and 32 output ports are connected to microstrip transmission lines via SMA connectors as shown in the center inset of Fig. 11-39. The output ports are then connected via coaxial cables of equal length to 32 horn antenna elements. The horn elements have a small transition from coaxial cable to the wave

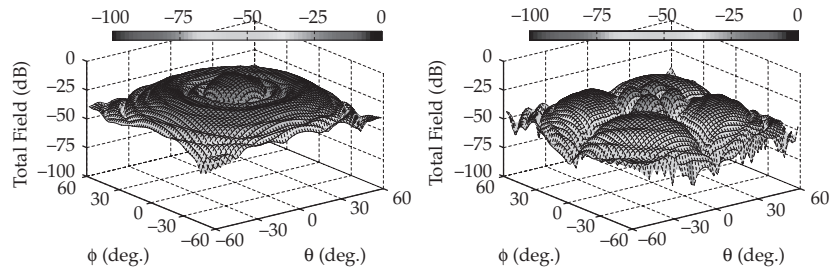

Figure 11-38 Radiation patterns of a circular dipole array with aircraft radome

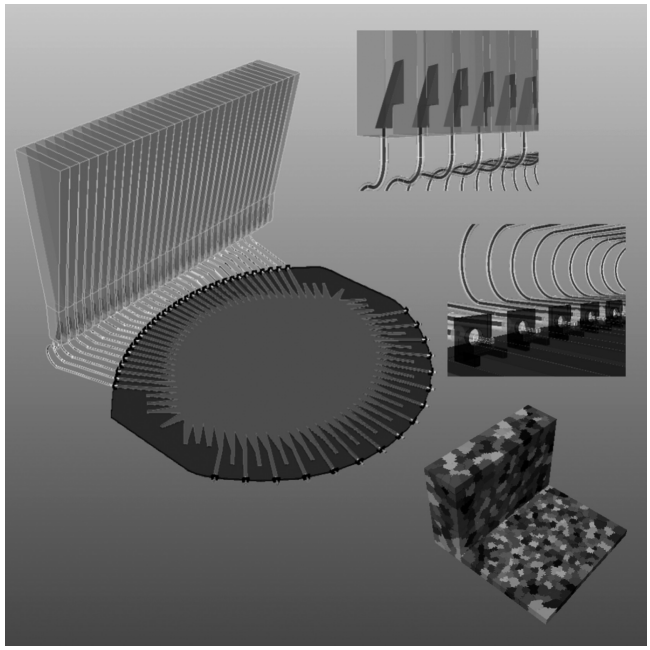

Figure 11-39 Configuration of the Rotman lens and horn antenna array. Insets (from upper right, clockwise): coax-to-horn antenna transitions, SMA connectors, and mesh decomposition.

guiding structure (upper inset of Fig. 11-39). Each horn element is $6.6\lambda_0$ high and $2\lambda_0 \times 0.36\lambda_0$ at the aperture. The entire geometry is enclosed in an L-shaped box with its boundary never less than $\frac{1}{3}\lambda_0$ from the geometry.

Simulations are performed for two input port excitations with the first excitation toward the center of the lens and the second one off-center. The excitation port determines the amount of phase variation in the output ports: the further the excitation port from center, the larger the phase variation and beamsteering angle.

The mesh consists of 2,847,778 tetrahedra and a decomposition into 1000 domains leads to 18,190,650 DoFs. The preconditioner setup requires 12 minutes and must be performed only once for both port excitations. The center port simulation requires 42 minutes for 281 CR iterations ($\epsilon = 10^{-2}$), whereas the off-center excitation requires 48 minutes for 313 iterations. Both simulations have peak memory usages of 30.7 GB.

The electric field magnitudes, plotted with logarithmic scales, are given in Figs. 11-40a and 11-40b and the radiation patterns in Fig. 11-41. The effect of varying the excited input port is clearly visible upon examination of the wavefronts in Figs. 11-40a and 11-40b. Note that in the case of the "center" port excitation, a small phase difference occurs at the output ports due to the fact that the even number of input ports requires a slightly off-center input. A much larger phase variation is seen for the off-center input. The fields on the apertures of the horn antennas confirm this as do the radiation patterns that show main lobes centered at 3.5 and 39.5 degrees, for center and off-center excitations, respectively.

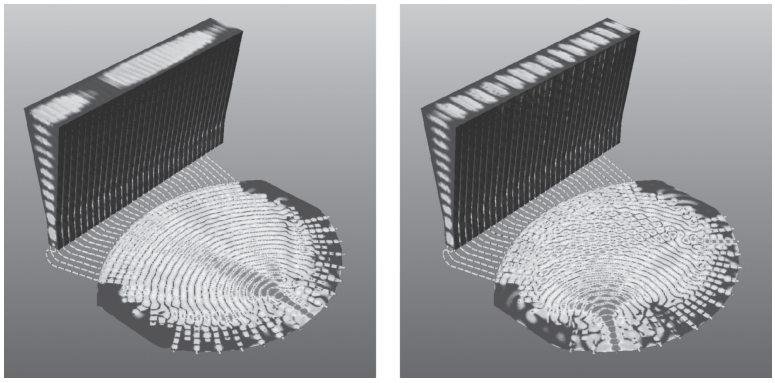

(a) (b)

Figure 11-40 (a) Electric field (log. scale) of a Rotman lens feeding a horn antenna array, center port excitation. (b) Electric field (log. scale) of a Rotman lens feeding a horn antenna array, off-center port excitation.

11.3.4.7 F-16 Scattering

Finally, we simulate the scattering of a $f = 1$ GHz plane-wave incident upon a long-range F-16 jet. The problem geometry, with a truncation boundary at least $\lambda_0/3$ away from the scatterer, is approximately 15 m long, 8 m wide, and 4.5 m high. A hollow dielectric radome with permittivity $\varepsilon = 3$ is placed at the front of the aircraft while a glass canopy with $\varepsilon = 4.7 - j0.0705$ sits atop the PEC body to form the cockpit. Figure 11-42 shows the geometry of the jet along with the surface mesh and the inset illustrates the partitioning of the 2,8444,939 tetrahedra into 500 domains. In this case, simulation of the 19,817,336 DoF problem could not be fit entirely into RAM, and the factorizations were written and read from disk only when necessary. This considerably increases the wall clock time and, because the disk operations are performed serially, seriously impacts parallel efficiency. In light of this, we employ a serial Gauss-Seidel preconditioner with a truncated GCR(5) solver for this simulation, though the matrix vector multiplication is still performed in parallel.

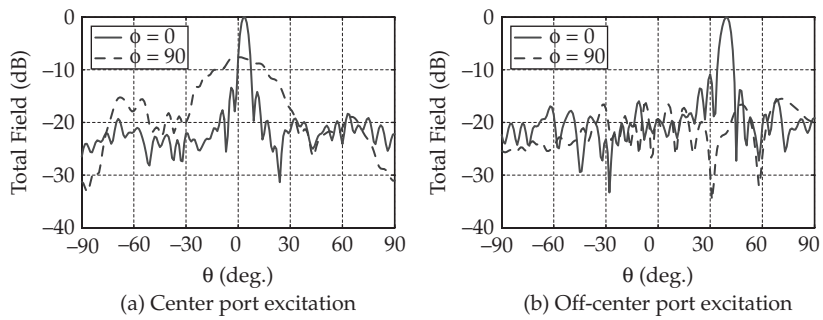

Figure 11-41 Radiation patterns of a Rotman lens feeding a horn antenna array

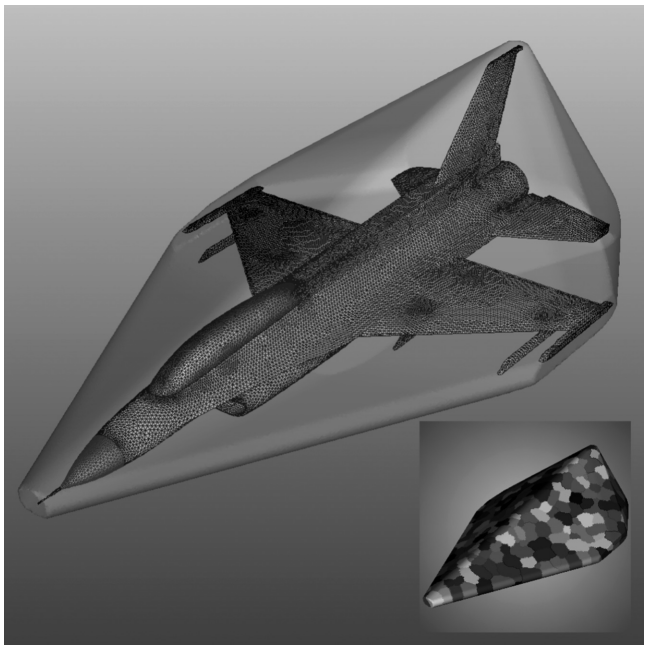

Figure 11-42 F-16 geometry and surface mesh. Inset: mesh decomposition

The simulations of both nose-on and oblique incidence required 1 hour and 52 minutes for preconditioner setup and a peak memory of 19.23 GB. The nose-on simulation required 4 hours and 50 minutes for 39 iterations while the oblique simulation used 4 hours and 10 minutes for 36 iterations. The electric fields on the F-16 are depicted in Figs. 11-43a and 11-43b for the nose-on and oblique excitations.

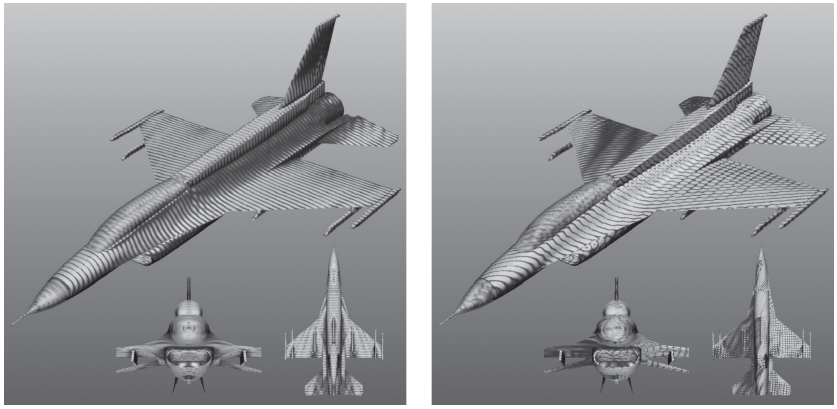

(a) (b)

Figure 11-43 (a) Electric field of F-16 scattering problem, normally incident excitation. (b) Electric field of F-16 scattering problem, obliquely incident excitation.

References

[1] F. L. Teixeira, "Time-domain finite-difference and finite-element methods for Maxwell equations in complex media," *IEEE Trans. Antennas Propagat.,* vol. 56, no. 8, pp. 2151–2166, 2008.

[2] F. L. Teixeira, and W. C. Chew, "Finite-difference computation of transient electromagnetic fields for cylindrical geometries in complex media," *IEEE Trans. Geosci. Remote Sens.,* vol. 38, no. 4, pp.1530–1543, 2000.

[3] B. Donderici, and F. L. Teixeira, "Conformal perfectly matched layer for the mixed finite element time-domain method," *IEEE Trans. Antennas Propagat.,* vol. 56, no. 4, pp. 1017–1026, 2008.

[4] N. Venkatarayalu, C.-C. Chen, F. L. Teixeira, and R. Lee, "Numerical modeling of ultra-wideband dielectric horn antennas using FDTD," *IEEE Trans. Antennas Propagat.,* vol. 52, no. 5, pp. 1318–1323, 2004.

[5] K.-H. Lee, C.-C. Chen, F. L. Teixeira, and R. Lee, "Modeling and characterization of geometrically complex UWB antennas using FDTD," *IEEE Trans. Antennas Propagat.,* vol. 52, no. 8, pp. 1983–1991, 2004.

[6] K.-Y. Jung, and F. L. Teixeira, "Photonic crystals with a degenerate band edge: Field enhancement effects and sensitivity analysis," *Phys. Rev. B,* vol. 77, no. 12, 2008.

[7] K.-Y. Jung, F. L. Teixeira, and R. Reano, "Au SiO2 nanoring plasmon waveguides at optical communication band," *J. Lightwave Technol.,* vol. 25, no. 9, pp. 2757–2765, 2007.

[8] A. Taflove, and S. Hagness, "*Computational Electrodynamics: The Finite-Difference Time-Domain Method,*" Artech House, Norwood, MA, 2005.

[9] J.-F. Lee, R. Lee, and A. C. Cangellaris, "Time domain finite element methods," *IEEE Trans. Antennas Propagat.,* vol. 45, no. 3, pp. 430–442, 1997.

[10] J. M. Jin, *The Finite Element Method in Electromagnetics,* 2nd ed. John Wiley, New York, 2002.

[11] S. Wang, and F. L. Teixeira, "Some remarks on the stability of time-domain electromagnetic simulations," *IEEE Trans. Antennas Propagat.,* vol. 52, no. 3, pp. 895–898, 2004.

[12] B. Donderici, and F. L. Teixeira, "Mixed finite-element time-domain method for Maxwell equations in doubly-dispersive media," *IEEE Trans. Microwave Theory Tech.,* vol. 56, no. 1, pp. 113–120, 2008.

[13] H. O. Lee, and F. L. Teixeira, "Cylindrical FDTD analysis of LWD tools through anisotropic dipping-layered earth media," *IEEE Trans. Geosci. Remote Sens.,* vol. 45, no. 2, pp. 383–388, 2007.

[14] C. Kung, and R. Lee, "Alternative FDTD updating schemes for anisotropic materials," *IEEE Trans. Antennas Propagat.,* vol. 57, no. 12, pp. 895–898, 2009.

[15] J. P. Berenger, "A perfectly matched layer for the absorption of electromagnetic waves," *J. Comput. Phys.,* vol. 114, no. 2, pp. 185–200, 1994.

[16] F. L. Teixeira, and W. C. Chew, "Complex space approach to perfectly matched layers: A review and some new developments," *Int. J. Numer. Model.,* vol. 13, pp. 441–455, 2000.

[17] J. A. Roden, and S. D. Gedney, "Efficient implementation of the uniaxial-based PML media in three-dimensional nonorthogonal coordinates with the use of the FDTD technique," *Microw. Opt. Technol. Lett.,* vol. 14, no. 2, pp. 71–75, 1997.

[18] M. Kuzuoglu, and R. Mittra, "Investigation of nonplanar perfectly matched absorbers for finite-element mesh truncation," *IEEE Trans. Antennas Propagat.,* vol. 45, no. 3, Mar. 1997.

[19] F. L. Teixeira, and W. C. Chew, "Analytical derivation of a conformal perfectly matched absorber for electromagnetic waves," *Microw. Opt. Tech. Lett.,* vol. 17, no. 4, pp. 231–236, 1998.

[20] F. L. Teixeira, W. C. Chew, M. Straka, M. L. Oristaglio, and T. Wang, "Finite-difference time-domain simulation of ground penetrating radar on dispersive, inhomogeneous, and conductive soils," *IEEE Trans. Geosci. Remote Sens.,* vol. 36, no. 6, pp. 1928–1937, June 1998.

[21] B. He, and F. L. Teixeira, "On the degrees of freedom of lattice electrodynamics," *Phys. Lett. A,* vol. 336, pp. 1–7, 2005.

[22] F. C. Yang, and K. S. H. Lee, "Impedance of a two-conical-plate transmission line," *Sensor and Simulation Notes, Air Force Research Laboratory,* Nov. 1976.

[23] J. L. Volakis, A. Chatterjee, and L. Kempel, *Finite Element Methods for Electromagnetics.* New York: IEEE Press, 1998.

[24] J. Jin, and D. J. Riley, *Finite Element Analysis of Antennas and Arrays.* Wiley-IEEE Press, 2008.

[25] P. P. Silvester, and G. Pelosi, *Finite elements for wave electromagnetics.* New York: IEEE Press, 1994.

[26] Y. Zhu, and A. Cangellaris, *Multigrid Finite Element Methods for Electromangtic Field Modeling.* New Jersey: IEEE Press, 2006.

[27] P. Monk, *Finite Element Methods for Maxwell's Equations.* Clarendon Press, Oxford, 2003.

[28] A. Bossavit, *Computational Electromagnetism.* Academic Press, San Diego, 1998.

[29] J. C. Nedelec, "Mixed finite elements in r3," *Numerische Mathematik,* vol. 35, pp. 315–341, 1980.

[30] P. G. Ciarlet, *The Finite Element method for Elliptic Problems,* Volume 4 of *Studies in Mathematics and Its Applications*, North-Hollan, New York, 1978.

[31] R. D. Graglia, "The use of parametric elements in the moment method solution of static and dynamic volume integral equations," *IEEE Trans. Antennas and Propagation,* vol. 36, no. 5, pp. 636–646, May 1988.
[32] M. I. Sancer, R. L. McClary, and K. J. Glover, "Electromagnetic computation using parametric geometry," *Electromagnetics,* vol. 10, pp. 85–103, 1990.
[33] G. E. Antilla, and N. G. Alexopoulos, "Scattering from complex 3d geometries by a curvilinear hybrid finite element-integral equation approach," *J. Opt. Soc. Am. A.,* vol. 11, no. 4, pp. 1445–1457, 1994.
[34] T. Ozdemir, and J. L. Volakis, "Triangular prisms for edge-based vector finite elements analysis of conformal antennas," *IEEE Trans. Antennas Propagat.,* vol. 45, no. 5, pp. 788–797, May 1997.
[35] Z. J. Cendes, "Vector finite elements for electromagnetic field computation," *IEEE Trans Magnatics,* vol. 27, no. 5, pp. 3958–3966, Sept. 1991.
[36] B. Engquist, and A. Majda, "Absorbing boundary conditions for the numerical simulation of waves," *Math. Comput.,* vol. 31, pp. 629–651, 1977.
[37] A. Bayliss, and E. Turkel, "Radiation boundary conditions for wave-like equations," *Appl. Math.,* vol. 33, pp. 707–725, 1980.
[38] Stratton, J. A., *Electromagnetic Theory.* Wiley-Interscience, Classic Reissue, 2007.
[39] X. Q. Sheng, J.-M. Jin, J. M. Song, C. C. Lu, and W. C. Chew, "On the formulation of hybrid finite-element and boundary-integral methods for 3d scattering," *IEEE Trans. Antennas Propagat.,* vol. 46, no. 3, pp. 303–311, Mar. 1998.
[40] T. F. Eibert, J. L. Volakis, D. R. Wilton, and D. R. Jackson, "Hybrid febi modeling of 3d doubly periodic structures utilizing triangular prismatic elements and a mpie formulation accelerated by the ewald transformation," *IEEE Trans. Antennas Propagat.,* vol. 47, no. 5, pp. 843–850, Mar. 1999.
[41] M. Vouvakis, S. C. Lee, K. Zhao, and J. F. Lee, "A symmetric fem-ie formulation with a single-level ie-qr algorithm for solving electromagnetic radiation and scattering problems," *IEEE Trans. Antennas Propagat.,* vol. 52, pp. 3060–3070, Nov. 2004.
[42] M. M. Botha, and J.-M. Jin, "On the variational formulation of hybrid finite element-boundary integral techniques for electromagnetic analysis," *IEEE Trans. Antennas Propag.,* vol. 52, no. 11, pp. 3037–3047, Nov. 2004.
[43] R. D. Graglia, D. R. Wilton, and A. F. Peterson, "Higher order interpolatory vector bases for computational electromagnetics," *IEEE Trans. Antennas Propagat.,* vol. 45, no. 3, pp. 329–342, March 1997.
[44] R. D. Graglia, D. R. Wilton, A. F. Peterson, and I.-L. Gheorma, "Higher order interpolatory vector bases on prism elements," *IEEE Trans. Antennas Propagat.,* vol. 46, no. 3, pp. 442–450, Mar. 1998.
[45] J. P. Webb, "Hierarchical vector basis functions of arbitrary order for triangular and tetrahedral finite elements," *IEEE Trans. Antennas Propag.,* vol. 47, no. 8, pp. 1244–1253, Aug. 1999.
[46] L. S. Andersen, and J. L. Volakis, "Development and application of a novel class of hierarchical tangential vector finite elements for electromagnetics," *IEEE Trans. Antennas Propagat.,* vol. 47, no. 1, pp. 112–120, Jan. 1999.
[47] E. Jorgensen, J. L. Volakis, P. Meincke, and O. Breinbjerg, "Higher order hierarchical legendre basis functions for electromagnetic modeling," *IEEE Trans. on Antennas and Propagation,* pp. 2985–2995, 2004.
[48] D. K. Sun, Z. Cendes, and J.-F. Lee, "Adaptive mesh refinement, h-version, for solving multi-port microwave devices in three dimensions," *IEEE Trans. Magn.,* vol. 36, no. 4, pp 1596–1599, Jul. 2000.
[49] T. B. A. Senior, and J. L. Volakis, *Approximate Boundary Conditions in Electromagnetics.* IET Press, 1995.
[50] Y. Zhang, R. A. van de Geijin, M. C. Taylor, and T.K. Sarkar, "Parallel mom using hihger-order basis functions and plapack in-core and out-of-core solvers for challenging em simulations," *IEEE Antennas Propagation Magazine,* vol. 51, no. 5, pp. 42–60, Oct. 2009.
[51] S.-C. Lee, M. N. Vouvakis, and J.-F. Lee, "A non-overlapping domain decomposition method with non-matching grids for modeling large finite antenna arrays," *J. Comput. Phys.,* vol. 203, no. 1, pp. 1–21, 2005.
[52] M. N. Vouvakis, Z. Cendes, and J.-F. Lee, "A FEM domain decomposition method for photonic and electromagnetic band gap structures," *IEEE Trans. Antennas and Propagation,* vol. 54, no. 2, pp. 721–733, Feb. 2006.
[53] K. Zhao, V. Rawat, S.-C. Lee, and J.-F. Lee, "A domain decomposition method with nonconformal meshes for finite periodic and semi-periodic structures," *IEEE Trans. Antennas and Propagation,* vol. 55, no. 9, pp. 2559–2570, Sept. 2007.
[54] Z. Peng, V. Rawat, and J.-F. Lee, "One way domain decomposition method with second order transmission conditions for solving electromagnetic wave problems," *J. Comput. Phys.,* vol. 229, no. 4, pp. 1181–1197, 2010.

[55] R. Coifman, V. Rokhlin, and S. Wandzura, "The fast multipole method for the wave equation: A pedestrian prescription," *IEEE Antenna Propagat. Magazine,* vol. 35, no. 3, pp. 7–12, June 1993.
[56] E. Bleszynski, M. Bleszynski, and T. Jaroszewicz, "Aim: Adaptive integral method for solving large-scale electromagnetic scattering and radiation problems," *Radio Sci.,* vol. 31, no. 5, pp. 1225–1251, Sep./Oct. 1996.
[57] R. W. Kindt, K. Sertel, E. Topsakal, and J. L. Volakis, "Array decomposition method for the accurate analysis of finite arrays," *IEEE Trans. Antennas and Propagation,* vol. 51, no. 6, pp. 1364–1372, June 2003.
[58] R. Harrington, *Time-Harmonic Electromagnetic Fields.* John Wiley & Sons, New York, 2001.
[59] R. A. Adams, *Sobolev spaces.* Academic Press, New York-London, 1975. Pure and Applied Mathematics, vol. 65.
[60] P. Monk, *Finite Element Methods for Maxwell's Equations.* Numerical Mathematics and Scientific Computation. Oxford University Press, New York, 2003.
[61] P. Houston, I. Perugia, A. Schneebeli, and D. Schotzau, "Interior penalty method for the indefinite time-harmonic Maxwell equations," *Numer. Math.,* vol. 100, no. 3, pp. 485–518, 2005.
[62] A. Buffa, P. Houston, and I. Perugia, "Discontinuous Galerkin computation of the Maxwell eigenvalues on simplicial meshes," *J. Comput. Appl. Math.,* vol. 204, no. 2, pp. 317–333, 2007.
[63] P. Houston, I. Perugia, and D. Schotzau, "Energy norm a posteriori error estimation for mixed discontinuous Galerkin approximations of the Maxwell operator," *Comput. Methods Appl. Mech. Engrg.,* vol. 194, no. (2–5), pp. 499–510, 2005.
[64] D. N. Arnold, "An interior penalty finite element method with discontinuous elements," *SIAM J. Numer. Anal.,* vol. 19, no. 4, pp. 742–760, 1982.
[65] D. N. Arnold, F. Brezzi, B. Cockburn, and L. D. Marini, "Unified analysis of Discontinuous Galerkin methods for elliptic problems," *SIAM J. Numer. Anal.,* vol. 39, no. 5, pp. 1749–1779, 2002.
[66] B. Despres, *Methodes de décomposition de domaine pour les problémes de propagation d'ondes en régime harmonique.* PhD thesis, Université Dauphine–Paris IX, 1991.
[67] B. Després, P. Joly, and J. E. Roberts, "A domain decomposition method for the harmonic Maxwell equations," In *Iterative methods in linear algebra* (Brussels, 1991), pp. 475–484. North-Holland, Amsterdam, 1992.
[68] M. N. Vouvakis, *A Non-Conformal Domain Decomposition Method for Solving Large Electromagnetic Wave Problems.* PhD thesis, Ohio State University, Columbus, Ohio, 2005.
[69] K. Zhao, *A Domain Decomposition Method for Solving Electrically Large Electromagnetic Problems.* PhD thesis, Ohio State University, Columbus, Ohio, 2007.
[70] J.-C. Nédélec, "Mixed finite elements in $\mathbb{R}^3$," *Numer. Math.,* vol. 35, no. 3, pp. 315–341, 1980.
[71] D.-K. Sun, J.-F. Lee, and Z. Cendes, "Construction of nearly orthogonal Nedelec bases for rapid convergence with multilevel preconditioned solvers," *SIAM Journal on Scientific Computing,* vol. 23, no. 4, pp. 1053–1076, 2001.
[72] D. G. Luenberger, "The conjugate residual method for constrained minimization problems," *SIAM Journal on Numerical Analysis,* vol. 7, no. 3, pp. 390–398, 1970.
[73] S. C. Eisenstat, H. C. Elman, and M. H. Schultz, "Variational iterative methods for nonsymmetric systems of linear equations," *SIAM Journal on Numerical Analysis,* vol. 20, no. 2, pp. 345–357, 1983.
[74] G. Karypis, and V. Kumar, "A fast and high quality multilevel scheme for partitioning irregular graphs," *SIAM J. Sci. Comput.,* vol. 20, no. 1, pp. 359–392 (electronic), 1998.
[75] B. Chapman, G. Jost, and R. van der Pas, *Using OpenMP: Portable Shared Memory Parallel Programming.* MIT Press, Cambridge, Massachusetts, 2008.
[76] J.-F. Lee, and D.-K. Sun, "*p*-Type multiplicative Schwarz (pMUS) method with vector finite elements for modeling three-dimensional waveguide discontinuities," *IEEE Trans. Microwave Theory and Techniques,* vol. 52, no. 3, pp. 864–870, 2004.
[77] B. A. Munk, *Finite Antenna Arrays and FSS*. John Wiley & Sons, New York, 2003.